_____

Unterschrift des Betreuers

TU WIEN | **TECHNISCHE UNIVERSITÄT WIEN**

DIPLOMARBEIT

Respiratory Motion Detection and Compensation for PET Imaging of Patients with Lung Cancer

ausgeführt am Institut für Angewandte Physik
der Technischen Universität Wien

in Zusammenarbeit mit dem

Zentrum für Medizinische Physik und Biomedizinische Technik
der medizinischen Universität Wien

unter der Anleitung von

Ao.Univ.-Prof. DI Dr. Martin Gröschl
(Technische Universität Wien)

und
als verantwortlich mitwirkendem Universitätsassistenten

Jacobo Cal González, PhD
(Center for Medical Physics and Biomedical Engineering)
(Medizinische Universität Wien)

durch
Seyedhossein Fatemi

Wien, 4th May 2018

_____

Unterschrift Student

Acknowledgements

Firstly I would like to thank Professor Martin Gröschl, my main supervisor at TU WIEN, for giving me the opportunity to work on this master thesis, and for all the useful comments and advice throughout the whole procedure.

My most sincere gratitude to Jacobo Cal González, my supervisor at Medical University of Vienna, for his truly exceptional supervision and support over the course of this thesis through regular daily and weekly meetings. I cannot thank him enough for the patience and time he dedicated to proofread and correct this thesis.

I would also like to thank Martin Lassen for his thoughts and advice on the subject and Alexander Berger for his constant help. I also thank all the colleagues that turned this last several months into a nice and pleasant memory.

And last but not least, I would like to thank my parents for their unconditional love and support throughout all these years.

Contents

Abbreviations

APD	Avalanche Photodiode
CNR	Contrast-to-Noise Ratio
CoM	Center of Mass method
CT	Computed Tomography
DD-Freq	Data-driven with Frequency filter
DD-MA	Data-driven with Moving Average filter
FBP	Filtered BackProjection
FDG	^{18}F-based Fluorodeoxyglucose
FOV	Field of View
FWHM	Full Width at Half Maximum
LBR	Lesion-to-Background Ratio
LOR	Line of Response
MCIR	Motion-Corrected Image Reconstruction
MoCo	Motion Compensation
MR	Magnetic Resonance
MRI	Magnetic Resonance Imaging
NAC	Non Attenuation-Corrected
NECR	Noise Equivalent Count Rate
OSEM	Ordered Subset Expectation Maximization
PET	Positron Emission Tomography
PET/CT	hybrid PET and CT device
PET/MR	hybrid PET and MR device
PMT	PhotoMultiplier Tube
ROI	Region of Interest
RTA	Reconstruct-Transform-Average
SiPM	Silicon PhotoMultiplier
SNR	Signal-to-Noise Ratio
STIR	Software for Tomographic Image Reconstruction
SUV	Standardized Uptake Value
TOF	Time of Flight
VOI	Volume of Interest

List of Figures

List of Tables

Abstract

Respiratory motion adds blurring to the PET activity distribution in the thoracic area. As a result, spatial resolution of PET images is reduced and quantitative measures are biased. The aim of this master thesis is to evaluate the impact of a projection-based and data-driven motion detection and compensation technique in the assessment of patients with lung tumors in simulated and real PET acquisitions with respiratory motion.

The validation of the data-driven method is done using data from two phantom experiments, filled with ^{18}F-FDG and scanned in a Biograph mCT PET/CT system. The data-driven respiratory extraction was validated against against respiratory signals obtained using a respiratory belt (Anzai AZ-733V). The optimization of the respiratory signal using the data-driven method in patients with lung cancer was performed in 12 ^{18}F-FDG PET/MR scans, acquired in listmode. Amplitude-based respiratory gating and reconstruct-transform-average motion compensation (RTA-MoCo) techniques were used to limit the blurring effect of the respiratory motion. The signal-to-noise ratio (SNR) in the frequency spectra and the contrast-to-noise ratio (CNR) in the reconstructed images were used as figures of merit to evaluate the performance of the respiratory motion detection techniques. Similarly, the lesion-to-background ratio (LBR) and the image noise were used as figures of merit to evaluate the quantitative accuracy of the images reconstructed with motion limiting techniques (gating and RTA-MoCo).

The data-driven extracted respiratory signal shows a high similarity with external signal with $r_s \approx 0.9$ for frequency filtered signals and $r_s \approx 0.75$ for the moving average filtered signals. Similar axial displacements (between 16 and 18 mm in the diaphragm, reference value = 20 mm) were observed in the gated images obtained using external, frequency filtered and moving average filtered signals. Respiratory motion was successfully detected and extracted in 8 of the 12 analyzed patients. The SNR in the frequency spectra showed a linear correlation with the amount of estimated motion ($r^2 = 0.704$). The motion-limited images (gated and RTA-MoCo) showed a clear increase in the LBR up to 20% (compared with the standard static images). The image noise increased for the gated images as much as 45%, while it was slightly reduced for the RTA-MoCo images ($\approx 15\%$).

The data-driven respiratory signal extraction is feasible in phantom data, obtaining similar results to the ones obtained with external markers; while in patient data it was successful in 8 of 12 analyzed cases. Future work includes the evaluation of further patient datasets and the comparison of the data-driven approach with other motion detection methodologies.

Kurzfassung

Die Atembewegung erhöht die Unschärfe der PET-Aktivitäts-Verteilung im Thoraxbereich. Dies führt dazu, dass die räumliche Auflösung von PET-Bildern reduziert wird und quantitative Messungen verzerrt werden. Ziel dieser Masterarbeit ist es, den Einfluss einer projektionsbasierten und datenbasierten Bewegungsdetektions- und Kompensationstechnik auf die Beurteilung von Patienten mit Lungentumoren bei simulierten und realen PET-Aufnahmen mit respiratorischer Bewegung zu untersuchen.

Die Validierung der datenbasierten Methode erfolgt mit Daten aus zwei Phantom-Experimenten, gefüllt mit ^{18}F-FDG und gescannt in einem Biograph mCT PET/CT-System. Die datenbasierte Atmungsextraktion wurde gegen Atemsignale validiert, die mit einem Atemgürtel (Anzai AZ-733V) erhalten wurden. Die Optimierung des Respirationssignals mittels der datenbasierten Methode wurde in 12 patienten mit Lungenkrebs mit ^{18}F-FDG PET/MR-Scans, die im Listmode erworben wurden, durchgeführt. Amplitudenbasierte Atmungs-Gating- und Rekonstruktions-Transformations-Durchschnittsbewegungskompensationstechniken (RTA-MoCo) wurden verwendet, um den Unschärfeeffekt der detektierten Atmungsbewegung zu begrenzen. Das Signal-zu-Rausch-Verhältnis (SNR) in den Frequenzspektren, das Kontrast-zu-Rausch-Verhältnis (CNR) in den rekonstruierten Bildern wurden als Gütezahlen verwendet, um die Leistung der Atembewegungserfassungstechniken zu bewerten. In ähnlicher Weise wurden das Läsion-zu-Hintergrund-Verhältnis (LBR) und das Bildrauschen als Gütezahlen verwendet, um die quantitative Genauigkeit der mit Bewegungsbegrenzungs-techniken rekonstruierten Bilder (Gating und Rekonstruktion) zu bewerten.

Das datenbasierte extrahierte respiratorische Signal zeigt eine hohe Ähnlichkeit mit dem externen Signal mit $r_s \approx 0,9$ für frequenzgefilterte Signale und $r_s \approx 0,75$ mit den gleitend gemittelten gefilterten Signalen. Ähnliche axiale Verschiebungen (zwischen 16 und 17 mm im Diapraghm, Referenzwert = 20 mm) wurden in den Gating-basierten Bildern beobachtet, die unter Verwendung externer, frequenzgefilterter und gleitend gemittelter gefilterter Signale erhalten wurden. Bei 8 der 12 analysierten Patienten wurde die Atembewegung erfolgreich nachgewiesen und extrahiert. Das SNR in den Frequenzspektren zeigte eine lineare Korrelation mit der geschätzten Bewegungsmenge ($r^2 = 0,704$).Die bewegungsbegrenzten Bilder (Gated und RTA-MoCo) zeigten eine deutliche Zunahme des LBR um bis zu 20% (im Vergleich zu den Standard-statischen Bildern). Das Bildrauschen stieg fr die gated-Bilder um bis zu 45%, whrend es fr die RTA-MoCo-Bilder leicht reduziert wurde (≈ 15%).

Die datenbasierte Atmungssignal-Extraktion ist mit Phantomdaten möglich, wobei ähnliche Ergebnisse wie bei externen Markern erhalten werden; mit Patientendaten war sie in 8 von 12 analysierten Fällen erfolgreich. Zukünftige Arbeiten umfassen die

Auswertung weiterer Patientendatensätze und den Vergleich des datenbasierten Ansatzes mit anderen Bewegungserkennungsmethoden.

Chapter 1

Introduction

Positron Emission Tomography (PET) (Cherry, Sorenson and Phelps 2012) is a functional imaging technique that produces a three-dimensional image of functional processes in the body. The PET scanner detect pairs of γ rays emitted by a positron-emitting radionuclide, which is introduced into the body in a biologically active molecule. This method is based on the tracer principle, which is developed in the beginning of 20th century by George de Hevesy. The tracer principle states that radioactive materials participate in the physiological processes the way nonradioactive compound do and since radionuclides undergo different decay processes, they can be detected with considerable sensitivity (Wernick and Aarsvold 2004). This method is categorized as a functional imaging technique to distinguish it from other imaging technologies such as x-ray computed tomography (CT) that in principle depicts the anatomical structure of the body. This ability to visualize physiological function, combined with anatomic images from CT or Magnetic Resonance Imaging (MRI), provides the best available information on tumor staging and diagnostic of other diseases (MacManus et al. 2009).

PET imaging has a variety of uses, which are shortly described as follows. In **oncology**, PET imaging is widely used for the detection and staging of tumors (Bailey et al. 2005). In **neurology**, PET is used for the diagnosis of diagnosis of dementia (Johnson et al. 2013), Parkinson's disease (Politis and Piccini 2012) or epilepsy (La Fougère et al. 2009). Alternatively, PET is also used in **cardiology** for the detection and monitoring of coronary artery disease (Schindler et al. 2010).

Lung cancer is one of the leading causes of cancer deaths worldwide for both genders. Accurate staging is one essential step in treatment and prognosis of the disease and to make a distinction between curable diseases and the ones that are candidates of palliative therapy. CT provides excellent morphologic information but has limitations in differentiating the malignancy of the tumor in the organs or the lymph nodes. ^{18}F-FDG PET plays an important role in diagnosis and staging of the lung cancer, especially for detection of nodal and metastatic site involvement. Its role has been more extensively studied in non-small cell lung carcinoma (NSCLC) than small cell lung carcinoma (SCLC) (Sharma et al. 2013; Steinert 2011). However, the use of PET imaging in lung/thoracic cancer is limited by the patient's respiratory motion, which may result in inaccurate PET image quantification due to motion-induced blurring and image artifacts.

Motion is a known source of degradation in every imaging modality that may need

a minimum amount of time to acquire the information for image generation. A routine PET scan takes normally around 10-20 minutes and the respiratory motion cannot be avoided during this time. This motion can contribute to blurring the image and losing the contrast which may lead to overestimation of the lesion size, as well as miscalculation of the standardized uptake value (SUV) (Yukutake et al. 2014). In addition to the mentioned blurring effect, motion can produce severe image artifacts caused by mismatches between the attenuation map and the emission map (Papathanassiou et al. 2005). When imaging lung cancer, motion affects the detectability of small tumor lesions (especially if they are located close to the diaphragm) and the accuracy of quantitative analysis, impairing diagnosis and therapy monitoring (Liu et al. 2009; Nehmeh et al. 2002).

According to previous studies, patient's diaphragm can move up to 2-3 cm during the acquisition (Kesner et al. 2014) and this leads to an underestimation of the tracer concentration of 30% and overestimation of the lesion size by a factor of 2 or even more (Liu, Alessio and Kinahan 2011).

Different methods have been proposed to detect and subsequently compensate the effect of respiratory motion in the thorax and abdominal area (Nehmeh 2013). The majority of the proposed methods are based on the use of external markers, such as respiratory belts, infrared sensors or measurements of the nasal air temperature. However, external tracking methods have several limitations that hamper their accuracy and applicability in clinical settings. First, most of these methods detect external motion, which does not necessarily correspond to the internal motion of the organs (Giraud and Houle 2013). In addition, respiratory external markers frequently require time-consuming calibrations (Lassen et al. 2017), have the risk of being inadequate throughout the acquisition due to changes in the respiratory baseline (Liu et al. 2009) or malfunctions during the acquisition (Gould 2017). Moreover, their use may be uncomfortable for patients. Therefore, there is an interest of obtaining respiratory gating without the use of external devices and with as little patient instructions as possible. In this context, data-driven methods, which derive the respiratory signal directly from the acquired PET data (self-gating methods) or through the use of MRI navigators in combined PET/MR systems, are promising alternatives to the use of external markers (He et al. 2008; Kesner et al. 2009; Grimm et al. 2015; Kesner and Kuntner 2010).

Objective of the thesis:

The aim of this thesis is to validate a data-driven self-gating method and subsequently apply it to several patient datasets, in order to obtain an optimized respiratory signal extraction. The main objective of the thesis will be achieved by the completion of the following specific objectives:

- To validate the data-driven motion detection method in phantom experiments. The extracted respiratory signal from the data-driven method is compared to the respiratory signal acquired from an external respiratory belt and the correspondence of two signals in time and frequency domain is examined.

- To compare and evaluate the gated images obtained by means of the data-driven method and the external respiratory signal. The respiratory translations of the

diaphragm will be measured in the gated images obtained from the data driven method and the external trigger.

- To apply the method to patient datasets, in order to find the correlation between signal-to-noise ratio (SNR), contrast-to-noise ratio (CNR) and the volume of the Region of Interest (ROI) used to extract the respiratory signal.

- To evaluate the impact of motion-limiting techniques (gating and post-reconstruction motion compensation techniques), both in the phantom experiments and in the patients datasets with significant motion.

Thesis structure:

The structure of this master thesis is as follows:

- Chapter 2 presents an introduction to the basic physics of PET and its devices, as well as an overview to the basic theoretical concepts related to the image formation process, the image reconstruction techniques and the data corrections necessary to obtain accurate and quantitative PET images.

- Chapter 3 present the methodology used in this master thesis. It starts with the specifications of the PET/CT and PET/MR hybrid systems used in this thesis. Then, the data acquisition formats used in PET and then the motion detection method used in this work are described. Next sections introduces the human thorax phantom used in the project and the figures of merit used to evaluate the data-driven respiratory signal and the final part of this chapter introduces the patient data and the figures of merit used to optimize the respiratory signal.

- Chapter 4 shows the main results of this master thesis. It begins with the results related to the phantom data, to show later the results obtained in the evaluated patient datasets.

- An in-deep discussion of the results presented in chapter 4, their implications, the limitations of the study and the future work to be done are presented in chapter 5.

- Finally, the main conclusions of this master thesis are provided in chapter 6.

Chapter 2

Theoretical Background

This chapter starts with a discussion about underlying physics of PET and its constituents. The chapter continues with the image formation in PET and different methods of image reconstruction and hybrid PET systems. The last section contains a short discussion on the motion detection and compensation techniques used in PET.

2.1 Basic Physics of PET

PET system takes advantage of the β^+ decay and the annihilation photons properties to produce images from radioactive distribution in the tissue. The following section discusses some fundamental properties of PET imaging and physics behind it.

2.1.1 Positron (β^+) Decay

In general, there are two ways to produce positron: pair production and radioactive decay. In radioactive process (β^+ decay), a proton transforms into a neutron and subsequently a positron and a neutrino are emitted.

$$\mathrm{p}^+ \longrightarrow \mathrm{n} + \mathrm{e}^+ + \nu + \text{energy} \tag{2.1}$$

The positron is the antiparticle of an electron, with all the physical properties the same than the electron but with positive electric charge. Since positron carries a positive charge, in order for the daughter nucleus to balance the charges, one orbital electron should be ejected from the atom in a process called electron capture. The minimum transition energy required for a β^+ decay to occur is 1.022 MeV.

The excess transition energy above 1.022 MeV will be distributed statistically between the positron and the neutrino and to a smaller amount the nucleus as their kinetic energies. The β^+ energy has a spectrum which is influenced by the nucleus (Figure 2.1). After emission of a positron, it loses it's kinetic energy either in inelastic collision with atomic electrons or in bremsstrahlung process with other atomic nuclei. Each one of these processes plus the elastic collision with the atomic nuclei, will deflect the positron and make it's path to be a very tortuous one until it comes to rest in a few millimeters from the decay process by temporarily forming an atom called positronium with an electron. The lifetime of this atom is about 10^{-10} s and then positron and electron will combine together to form an annihilation process in which their rest masses turn into energy in

the form of two γ rays with 0.511 MeV energy for each and as a result of momentum conservation, these photons will leave the annihilation site at nearly 180° in the opposite directions.
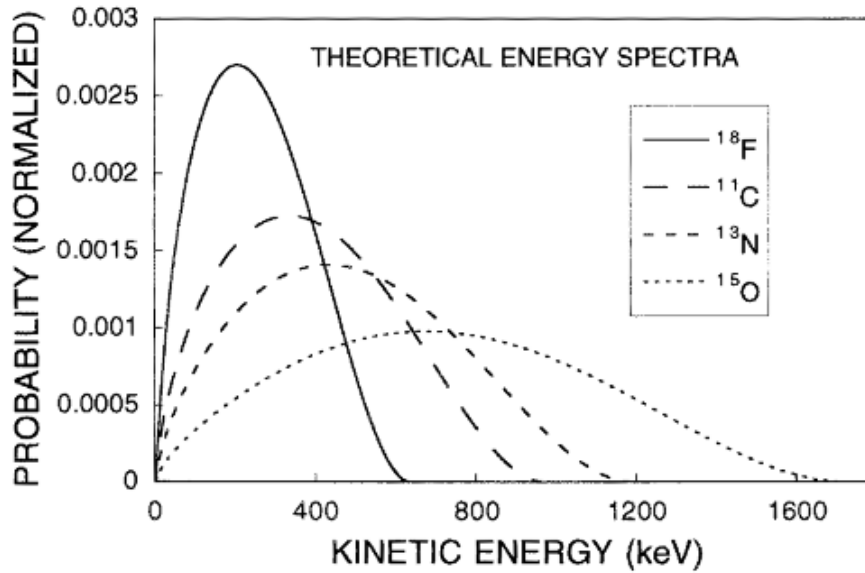
Figure 2.1: β^+ energy spectra of several commonly used radionuclides in PET (curves are normalized to have equal area) (Levin and Hoffman 1999).

The fact that the positron travels a finite distance before annihilation, adds some uncertainty in localizing the positron-emitting nuclei and is called positron range which has a detrimental effect on nuclear imaging resolution. This effect is subtle and becomes more serious with isotopes which emit positrons with higher energies (Figure 2.2) (Cal-González et al. 2013; Muehllehner, Buchin and Dudek 1976; Phelps et al. 1975). Due to the variation in momentum of the positron, the emitted annihilation photons travel not exactly 180 ° opposite of each other which limits the accuracy in localizing the annihilation point and as a result contributes to the degradation of PET imaging resolution. This happens especially when the detectors are further apart from each other (DeBenedetti et al. 1950).
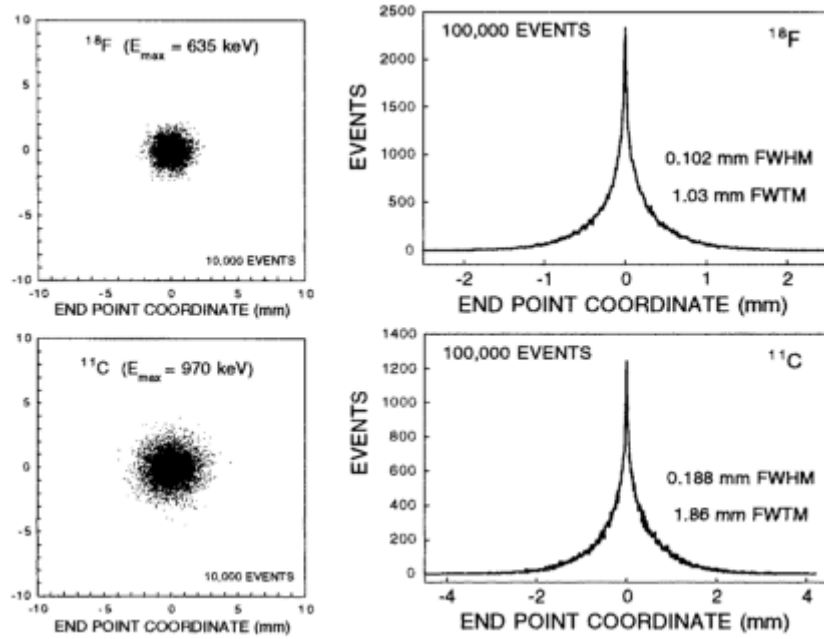
Figure 2.2: Distribution of annihilation points for positron-emitting point sources in water (^{18}F with $E_\beta^{\max} = 0.635$ MeV and ^{11}C with $E_\beta^{\max} = 0.97$ MeV) with broader distribution profile for ^{11}C (Levin and Hoffman 1999).

2.1.2 Radionuclide Production in PET

In general, there are two types of radioactive substances used in radionuclide imaging: gamma and positron emitters. The radionuclides which are used in PET imaging are positron emitters, in which the radioactive element undergoes a β^+ decay.

The main method in production of positron emitter radionuclides, is to use cyclotron to bombard the target material with charged particles. In this sense, the charged particles (proton, α-particle, deuteron, ...) should gain enough energy to overcome the Coulomb barrier of the target nucleus and initiate a nuclear reaction. Cyclotron consists of two hollow semicircular D-shaped electrodes called *dees* with a gap in between them and these electrodes are located in between the poles of a large magnet which provide a constant magnetic field (≈ 1.5 Tesla) in the center (Figure 2.3). With a high frequency AC voltage applied to the electrodes, the particle injected in the gap between the *dees* are going to be accelerated in a curved circular path according to the Lorentz-force:

$$\vec{F} = q(\vec{E} + \vec{V} \times \vec{B}) \tag{2.2}$$

So the centripetal force acting on the charged particle is:

$$\frac{mv^2}{r} = qvB \tag{2.3}$$

Hence the frequency of a revolution becomes:

$$\omega = \frac{qB}{m} = const \tag{2.4}$$

Which is known as the cyclotron frequency. In the high velocities range, the relativistic corrections should be applied, which gives us:

$$\omega = \frac{qB}{\gamma m_0} \tag{2.5}$$
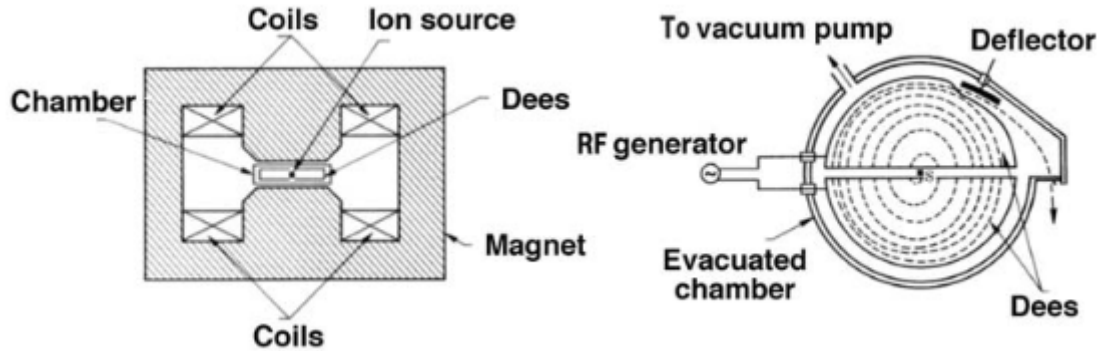
Figure 2.3: Schematic representation of a cyclotron. (Podgorsak 2005).

When the particle reaches the highest allowed orbital, it will be directed to a target material. The typical beam current at the target are in the range of 5-100 μA. The cyclotron works with both positive and negative beam acceleration. The positive beam accelerator uses electrostatic deflection which is very inefficient (around 30% of the beam current is lost during extraction). In a negative beam accelerator, an H^- particle (two electrons and a proton) gets accelerated and when reaches the outermost orbit it passes through a thin carbon foil to strip off the electrons and the positive charge gets deflected by the means of a magnetic field to the target material. ^{18}F is one of the most important cyclotron produced radionuclides using the highly enriched ^{18}O water as the target material in the reaction ^{18}O(p,n)^{18}F (Guillaume et al. 1991).

Besides the isotopes produced from a particle accelerator, there are some generator-produced radionuclides commonly used in PET imaging. These are, among others: (1) The ^{68}Ge radionuclide, which is used for example in receptor cancer imaging (Al-Nahhas et al. 2007), and it is produced in ^{68}Ge/^{68}Ga generators. (2) The ^{82}Rb radionuclide, which is produced in ^{82}Sr/^{82}Rb generators, and has applications for myocardial perfusion studies in PET (Knapp and Mirzadeh 1994). A summary of common positron emitters is provided in Table 2.1.

Positron-emitter	Half-life	Daughter	Maximum positron energy	Mean linear range in tissue
^{11}C	20.4 min	^{11}B	0.96 MeV	0.3 mm
^{13}N	9.9 min	^{13}C	1.19 MeV	0.4 mm
^{15}O	2.9 min	^{15}N	1.72 MeV	1.5 mm
^{18}F	110 min	^{18}O	0.64 MeV	0.2mm
^{68}Ga	68 min	^{68}Zn	1.89 MeV	1.9 mm
^{82}Rb	1.3 min	^{82}Kr	3.35 MeV	2.6 mm

Table 2.1: Some commonly used cyclotron and generator-produced radionuclides (taken from (Oppelt 2011)).

2.1.3   Interaction of Photons in Matter

Regarding the photon energies common to PET imaging there are three major processes that specify the interaction of photons in matter. What follows is a brief presentation of these effects.

Phtoelectric Effect

In this process, a photon transfers all its energy to an atom and vanishes itself as a consequence. The absorbed energy is used to eject an orbital electron (Figure 2.4). The kinetic energy of the ejected electron:

$$E_e = E_p - K_0 \tag{2.6}$$

can be calculated as a difference between the photon energy E_p and the electron binding energy K_0. This effect involves the innershell electrons and when the photon energy exceeds that of the K shell binding energy, around 80% of the interactions involve the K shell electrons (Cunningham and Johns 1983). The vacancy in the innershell of the atom produced by the photoelectron causes the emission of characteristic X-ray or Auger electrons.
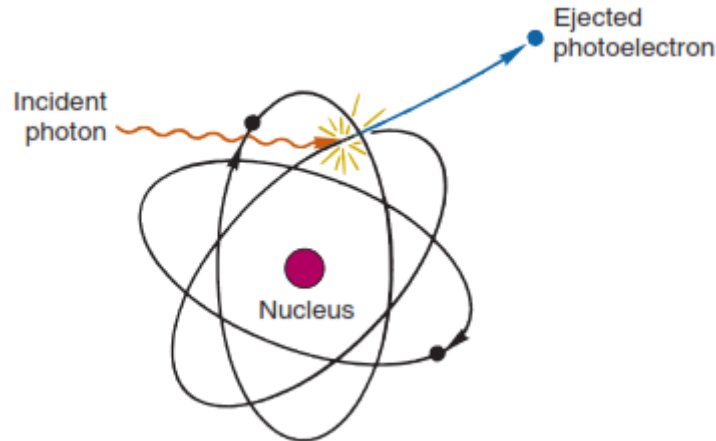
Figure 2.4: Photoelectric process and ejection of an innershell electron (Cherry, Sorenson and Phelps 2012).

Compton Scattering

Compton scattering considers the interaction of a high energy photon with a loosely bound orbital electron at rest (the electron is considered unbound) and in the process the electron is ejected from the atom and the photon is going to be scattered based on the amount of energy that transfers to the electron. The momentum and energy conservation calculations yields the equation below which specifies the final photon energy based on the incident photon energy and scattering angle:

$$E_f = \frac{E_0}{1 + \frac{E_0}{m_e c^2}(1 - \cos\theta)} \tag{2.7}$$

as the angle of scattered photon increases, the scattered photon energy decreases (Figure 2.5) and the recoil electron becomes more and more energetic.
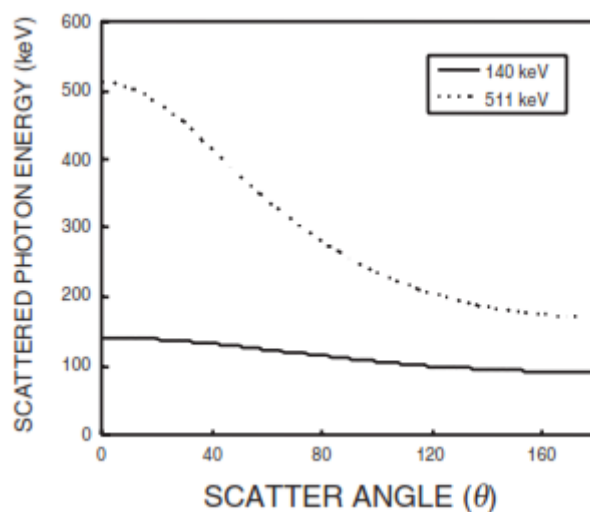
Figure 2.5: Energy of scattered photon as a function of its angle (Wernick and Aarsvold 2004).

It is worth noting that the scattered photon energy never reaches zero and the incoming photon cannot transfer all of its kinetic energy to the electron.

The back-scattering refers to the photon transferring the highest amount of energy possible to the orbital electron and as a consequence, scattering back with 180° to its initial direction. This maximum energy transferred to the electron is referred to as the compton edge in pulse height spectrometry, where the maximum energy deposited to the object during the back-scattering makes a peak in the deposited energy distribution in the detector.

Pair Production

In pair production, an energetic photon interacts with electric field of an atomic nucleus. The photon vanishes during this process and its energy is used to produce an electron-positron pair. The rest mass energy or electron or positron is 0.511 MeV, which means the incident photon energy most have a minimum of 1.022 MeV for this process to happen. The extra energy of the photon will be randomly shared between the electron and positron as their kinetic energies:

$$E_{positron} + E_{electron} = E_0 - 1.022 \text{MeV} \tag{2.8}$$

The electron and positron will lose their kinetic energy in ionization and excitation reactions. When the positron loses its energy and stops, reacts with an electron in an annihilation reaction and two gamma rays are produced that travel 180° opposite of each other.

The probability of a photon interacting with matter depends on its energy and the thickness of matter it travels. The mass attenuation coefficient μ experienced by the photon:

$$\mu = \tau + \sigma + \kappa \tag{2.9}$$

Which is a summation of mass attenuation caused by photoelectric effect, compton and pair production respectively. Figure 2.6 shows the prevalence regions of the interactions discussed above as a function of energy for different atomic numbers.
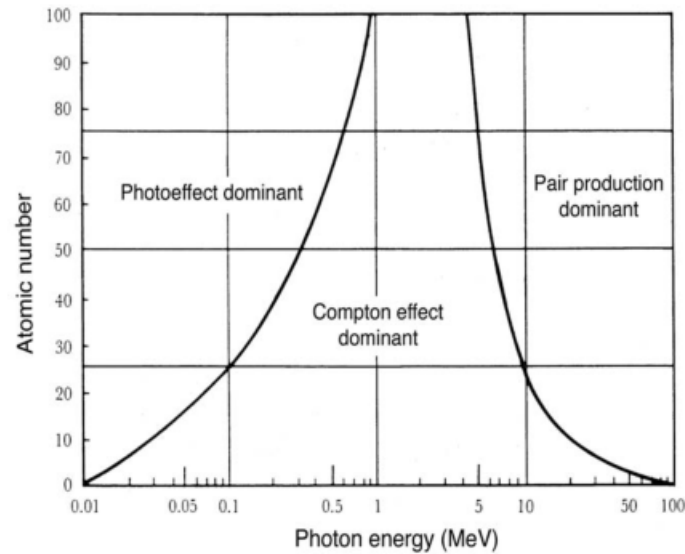
Figure 2.6: Interaction of photons in matter as a function of energy (Podgorsak 2005).

2.1.4   Radiation Detectors in PET

The basic idea of radiation detectors include measuring the deposited energy of radiation by some measurable quantity like electrical current. The most commonly used detectors in PET imaging include a scintillation detector, which interacts with gamma photons and yields visible light proportional to the energy deposited in the detector. In the second step a photo-detector called photomultiplier tube (PMT) will convert the incoming light to electrical pulses. In regards to the configuration of PET tomographs, There are two common detector design approaches in use nowadays. The first one consists of a few (6 to 8) large flat detectors which are coupled to an array of PMTs (Karp et al. 1990) and the second one which is a full ring circular system and is commonly used in modern PET systems, consists of arrays of small detectors, each one in a block coupled to a limited number of PMTs (Casey and Nutt 1986).

There are several important considerations in choosing the scintillators, among them is the stopping power for high-energy photons, which has a strong dependence to the atomic number of the material (higher atomic numbers raises the cross section of the photoelectric effect). The decay time is another important parameters that specifies the timing precision and the number of counts that can be processed in a unit of time. Among other important properties of the scintillators are high light output, index of refraction and transparency to its own scintillation photons. Table 2.2 shows a summary of some important properties of the scintillators.

Property	NaI(TI)	BGO	LSO	YSO	GSO	BaF$_2$
Density(g/cm^3)	3.67	7.13	7.4	4.53	6.71	4.89
Effective Z	50.6	74.2	65.5	34.2	58.6	52.2
Decay constant(ns)	230	300	40	70	60	0.6
Light output (photons/KeV)	38	6	29	46	10	2
Index of refraction	1.85	2.15	1.82	1.8	1.91	1.56
Hygroscopic?	yes	no	no	no	no	no
Peak emission(nm)	410	480	420	420	440	220

Table 2.2: Properties of some commonly used scintillators in PET (taken from (Bailey et al. 2005)).

The PMTs are consisted of a vacuum enclosure with a photocathode that ejects electrons when struck by visible light. The ejected electron are produced by photoelectric interaction and are called photoelectrons. The conversion efficiency of light to electron (also known as quantum efficiency) is 1-3 photoelectrons per 10 visible light photons. The photoelectron is guided through a focusing grid to a metal plate named dynode which is manitained at a positive voltage with respect to the photocathode. The photoelectron striking the dynode ejects several secondary electrons and this process continues over 9-12 dynodes, with each dynode having a higher potential than the last one (Cherry, Sorenson and Phelps 2012). In the end the gathered electrons will be collected in the anode (Figure 2.7).
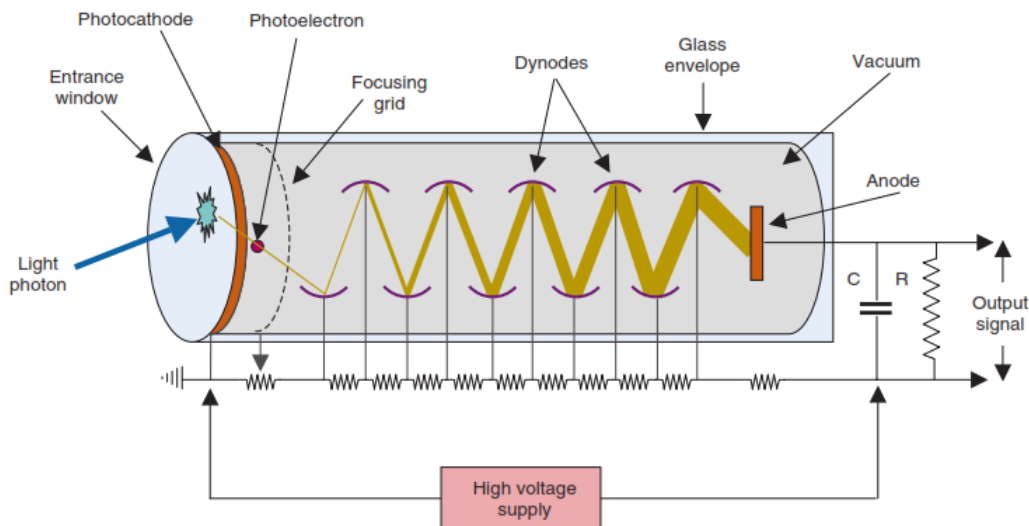
Figure 2.7: schematic representation of a photomultiplier tube (Cherry, Sorenson and Phelps 2012).

One significant drawback of PMTs is their extreme sensitivity to magnetic fields, which makes them not suitable to be used in combination with Magnetic Resonance scanners (MR), which use static and homogeneous magnetic fields higher than 1 T and radio-frequency pulses. As shown by (Peng 2007), significant variations of the gain and energy resolution of PMT-based detectors are observed as soon as the magnetic field is increased above 10 mT, and the ability to decode crystals in a array with PMT-based

detectors is rapidly lost as soon as the magnetic field becomes significant (Vaquero et al. 2013).

Solid-state detectors have several inherent advantages over PMTs, such as: high quantum efficiency, compact and flexible shape that can be adapted to individual crystals, ruggedness, demonstrated insensitivity to magnetic fields up to more than 10 T and potentially inexpensive mass production.

Avalanche photodiodes (APDs) are semiconductor devices with a low-field depleted region where visible or near-UV photons can create hole-electron pairs by photoelectric effect. APDs exist as small discrete devices (Lecomte et al. 1985) or as monolithic arrays (Pichler et al. 2004), which can be used for individual or multiplexed crystal readouts. APDs are insensitive to strong magnetic fields, and therefore can be used in combined PET/MR systems (Pichler, Judenhofer and Wehrl 2008).

Silicon Photomultipliers (SiPMs) consists of a densely packed matrix of small APD cells biased to be operated above avalanche breakdown in the so-called Geiger mode. All cells are connected in parallel via individual quenching resistors, which are needed to recharge a cell after a breakdown discharge. The Geiger-mode operation yields a high gain (10^5 - 10^6), and the multi-cell structure can provide a proportional output for moderate photon flux by summing all cells that have been activated. SiPMs are attractive for detector design in PET, because: high gain similar to PMTs avoiding the need for a low-noise electronic front-end, fast response, lower bias (< 100 V) and standard MOS semiconductor production process with low fabrication costs (Lecomte 2009). SiPM-based PET/CT (Miller et al. 2015) and PET/MR (Grant et al. 2016) systems are available nowadays.

2.2   PET Image Formation

This section begins with an overview of the event classification in PET and then a brief introduction on data acquisition types will be presented.

2.2.1   Event Characterization in PET

The detection of two annihilation photons can be considered as a valid event (Figure 2.8) if they meet the following three conditions: (1) Two annihilation photons be detected within a predefined coincidence time window (2) The line of response (LOR) needs to be a valid acceptance angle of the device (3) The energy of photons detected should be within the defined energy window. If all these conditions are met then the event is called a prompt event.Prompt events are of different origins:

- Single event: If a single photon is detected by the system.

- True events: Two detected photons that truly belong to the same annihilated positron.

- Random events: Two detected photons that are detected within the accepted time window but belong to different annihilation events. The rate of random events between two detectors is defined as:

$$R_{ab} = 2\tau N_a N_b \tag{2.10}$$

with τ being the coincidence time window and N being the activity rate on a detector. Usually $N_a \approx N_b$.

- Scattered events: When one or both of the photons detected within the same coincidence time window had undergone compton scattering.

- Multiple events: More than two photons are registered within a time window.

The prompt rate is defined as:

$$\text{prompt} = \text{trues} + \text{randoms} + \text{scatter} \tag{2.11}$$

As only the true events provide useful information about the 3D distribution of the injected tracer, randoms and scattered events must be corrected in order to obtain good quality PET images. These corrections will be shortly discussed in the following sections.
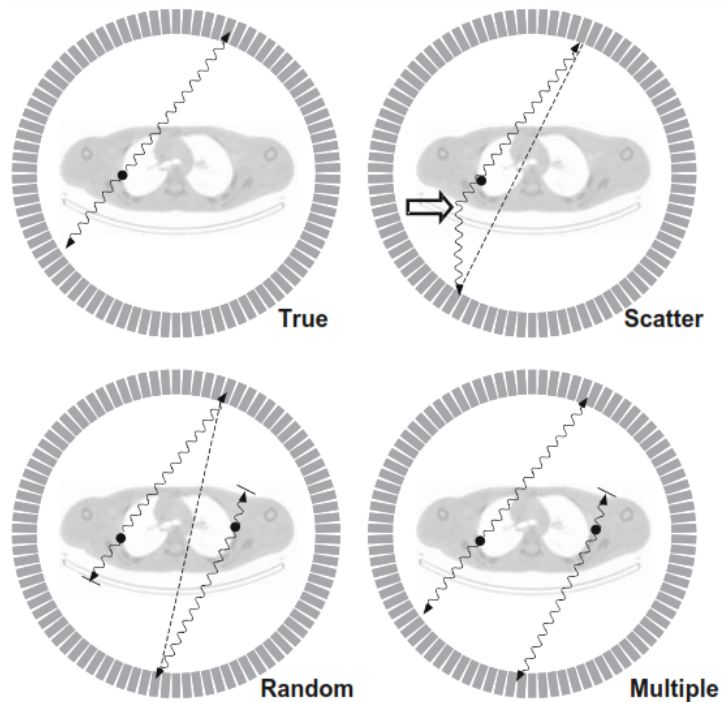
Figure 2.8: Coincidence events of different origins recorded by PET.Dashed lines indicate miscalculated lines of responses (Bailey et al. 2005).

The most common geometry of a PET system consists of either full circular rings of detectors that covers 360°(or partial rings) or multiple flat detectors. The defined coordiante system used for the PET system is shown in figure 2.9. The angle between the transaxial plane (x-y) and the z-axis is called the polar angle and the angle around x-y

plane is referred to as azimuthal angle. In 2D PET, $\theta \approx 0$ while in 3D PET θ can be opened up to allow prompt events between the rings. The selection of the polar angle is a trade-off between the sensitivity gain and the fraction of scatter events (Bailey et al. 2005).
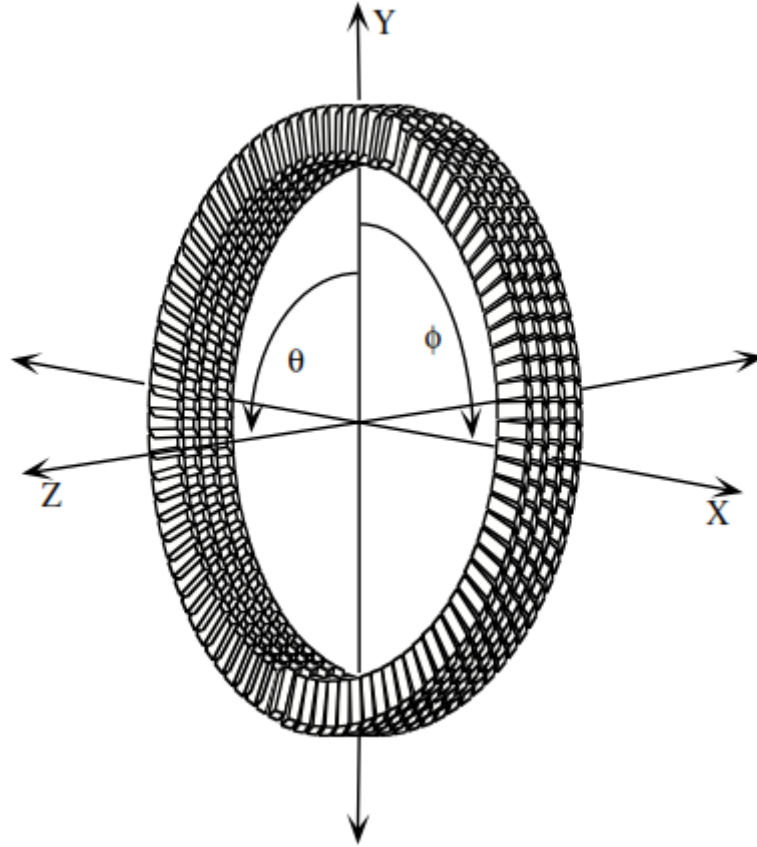
Figure 2.9: A full ring PET system with the azimuthal angle (ϕ) around the ring and the polar angle (θ) between the rings (Bailey et al. 2005).

Since PET systems do not need a physical collimator because the direction of annihilation photons are measured electronically, it gives them an advantage in spatial resolution over the imaging devices that use physical collimation, although there are several factors that limit the intrinsic spatial resolution in PET, such as for example: positron range, non-collinearity and detector size. Modern PET systems have spatial resolution in the range of 4-6mm (Hirtl 2017).

2.2.2   Data Acquisition Types in PET

Pertaining to the data acquisition types in emission tomography there are two prevalent approaches:

- List-mode: One way to store the measured coincidences for further processing is to write the information from prompt events in order of occurrence during the acquisition. An event packet may include: crystal number, photon energy,

positioning, etc. In addition, gantry information (as for example count rate and time information) as well as external data (gating and patient motion information) can be inserted into the list mode file (Byrne 2001).

- Sinogram: In this format, every LOR is characterized by its angle and its distance from the center of the gantry. The sinogram consist of a histogram representing the number of counts in each radial and angular bin. They are the basic ingredient of most image reconstruction algorithms due to their good mathematical properties. The sinogram corresponding to a point source in image space is represented as a sine wave, therefore the name 'sinogram'. (Fahey 2002)
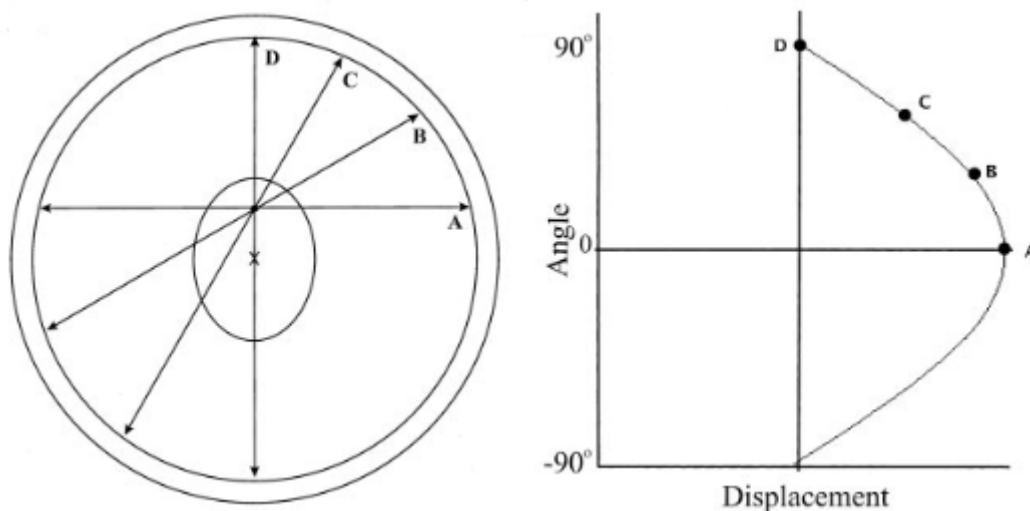
Figure 2.10: (left) four detected events for the same annihilation point.(right) their respective points on the sinogram (Fahey 2002).

The michelogram is a way to visualize how the axial data are combined with each other. On the y-axis we have detector rings on one side and on the x-axis we have the detectors on the opposite side.For each point on the grid we have one sinogram between the two rings. In a full 3D PET we have one point in each grid. In order to reduce the size of the 3D data, there is the possibility to combine several neighboring LORs in the axial direction, which is a usual method to compress the data size in PET and is called mashing.

As can be seen in Figure 2.11, for the image on the left the data acquisition is in 2D PET, which only contains the data for direct transaxial planes, as for the michelogram in the middle, the data contains sinograms for every possible correspondence between the rings and for the michelogram on the right, there are several sinograms connected together with a horizontal line which are combined to give one plane. There are several important parameters pertaining to the michelograms :

- Segments: As we do the mashing and combining several planes together into one transaxial plane, we basically segmenting our michelogram (for example in Figure 2.11 on the right we have 3 segments).
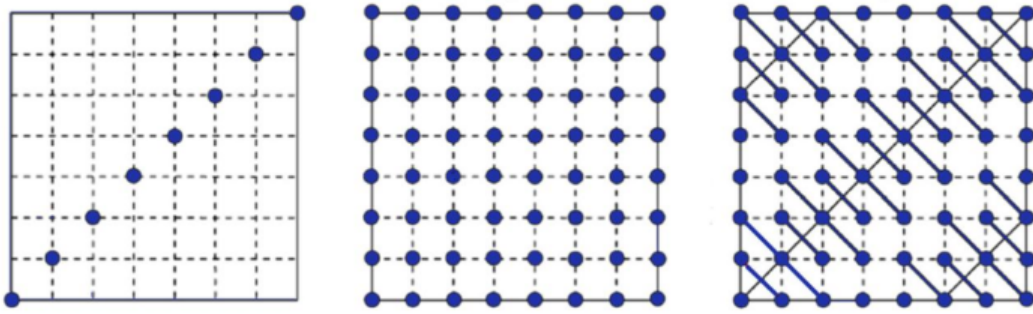
Figure 2.11: michelograms with 8 ring.(left) 2D acquisition (middle) 3D acquisition without mashing (right) 3D acquisition with mashing (Fahey 2002).

- Span: If we add the odd-numbered planes with the even-numbered planes (excluding first and last 2) we get the span number (in our case $3 + 2 = 5$).

- Maximum ring difference (MRD): Maximum allowed difference between the ring numbers.

2.3 PET Image Reconstruction

This section begins with an overview over the 2D and 3D data acquisition mode and continues with different image reconstruction techniques.

2.3.1 2D and 3D PET Imaging

2D PET imaging considers the lines of response (LOR) over a specific imaging plane. The data is collected from several projections for angles $0 \leq \phi \leq 2\pi$ into a sinogram for each transaxial slice through the body. The integration along each LOR for a fixed ϕ is called radon transform. After collecting the sinograms over all the axial slices, stacking all the image planes together will give the 3D image.

Although this 2D imaging leads to a 3D image in the end, it is different from a fully 3D imaging, since in 2D imaging it is just the LORs perpendicular to the patient axis or cross planes that are taken into account for each image plane but in 3D PET imaging the data is collected from all or most of the oblique planes (Figure 2.12). The advantage of 3D imaging mode is that it increases the sensitivity and lowers the statistical noise in image reconstruction which leads to higher signal-to-noise ratio and more scatter fraction that needs to be corrected.
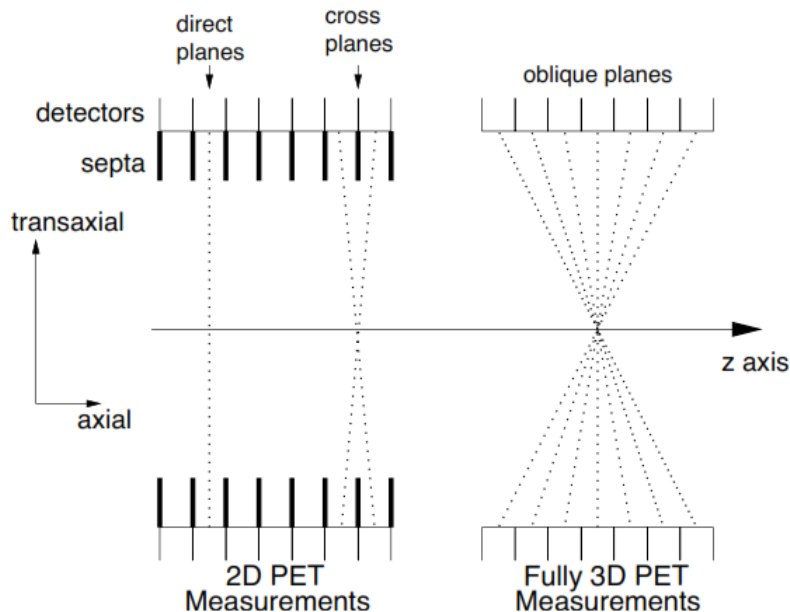
Figure 2.12: Two modes of imaging in PET. 2D imaging considers only direct and cross planes for each image plane. 3D PET on the other hand collects data for all or most of the oblique planes as well (Alessio and Kinahan 2006).

2.3.2   Analytic Image Reconstruction

This reconstruction method assumes that the acquired data is deterministic and free of statistical noise. The analytic reconstruction method is based on the Fourier-slice theorem, which states that the Fourier transform of the projection along any specific angle is equal in value to a section through the Fourier transform of the object at the same angle (Kak and Slaney, n.d.) (Figure 2.13). In this case, having the Fourier transform of all the projections and replacing them in the Fourier space leads to oversampling in the center of the Fourier transform of the object. The solution to this problem is using the Filtered Backprojection (FBP) (Bracewell and Riddle 1967), where as the name suggests, the Fourier transform of the projections are first filtered using a ramp filter and then backprojected to the image space (equation 2.12 (Birkfellner 2015)).

$$f(x,y) = \frac{1}{2\pi} \int\limits_0^\pi \left[\frac{1}{\sqrt{2\pi}} \int\limits_{-\infty}^\infty \widehat{R_f(\varphi,.)}(r)|r|e^{ir(x\cos\varphi + y\sin\varphi)} dr \right] d\varphi \qquad (2.12)$$

where the expression inside the squared brackets, is the inverse Fourier transform of $\widehat{R_f(\varphi,.)}(r)|r|$ calculated at $t = x\cos\varphi + y\sin\varphi$.
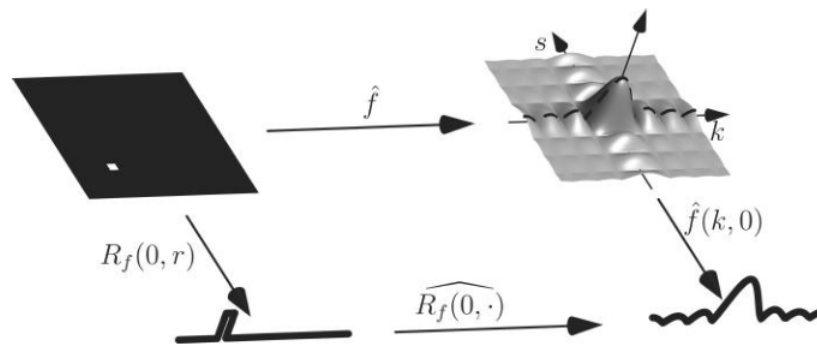
Figure 2.13: Visual illustration of the Fourier-slice theorem (Birkfellner 2015).

2.3.3   Iterative Image Reconstruction

Disregarding the noise in acquired PET data leads to images with reduced resolution and poor noise properties (Alessio and Kinahan 2006). The iterative reconstruction methods account for the noise in the measurements and gives more realistic solutions at cost of increased complexity. The components that need to be specified in every iterative method are the following: (1) a model for the image; (2) a description of the system model that relates the data to the image; (3) a model to relate how the measurements of the projections vary with their expected mean values; (4) a cost function that defines the best image, which usually is a Maximum Likelihood (ML) approach; and (5) an Expectation Maximization (EM) algorithm that optimize the cost function.

The most well-known iterative reconstruction method for tomographic imaging data is the Maximum Likelihood-Expectation Maximization (ML-EM) algorithm (Shepp and Vardi 1982; Dempster, Laird and Rubin 1977). This method uses the iterative equation (Alessio and Kinahan 2006):

$$f_j^{(n+1)} = \frac{\hat{f}_j^{(n)}}{\sum\limits_{i'} H_{i'j}} \sum\limits_{i} H_{ij} \frac{p_i}{\sum\limits_{k} H_{ik}\hat{f}_k^{(n)}} \tag{2.13}$$

where $\hat{f}_j^{(n+1)}$ is the next estimate of voxel j based on the current value $\hat{f}_j^{(n)}$. The algorithm starts with an estimation of the image, which usually is set to a constant value, then this image will be forward projected and the comparison of the estimated values and the measured projection values will result in a set of multiplicative correction factors which will be backprojected into image space and will be used as correction factor for the initial estimated image. This correction factors are later multiplied by the initial image and divided by a weighting term based on the model of the system. This new image will be then given as input to the algorithm and the process continues until a solution is reached (Alessio and Kinahan 2006) (Figure 2.14).

One of the most common iterative methods used in PET image reconstruction is a variation of the ML-EM algorithm explained abvo, and it is called Ordered Subsets Expectation Maximization (OSEM) (Hudson and Larkin 1994) method. This algorithm uses only a subset of entire data to reduce the reconstruction time at the cost of a slightly
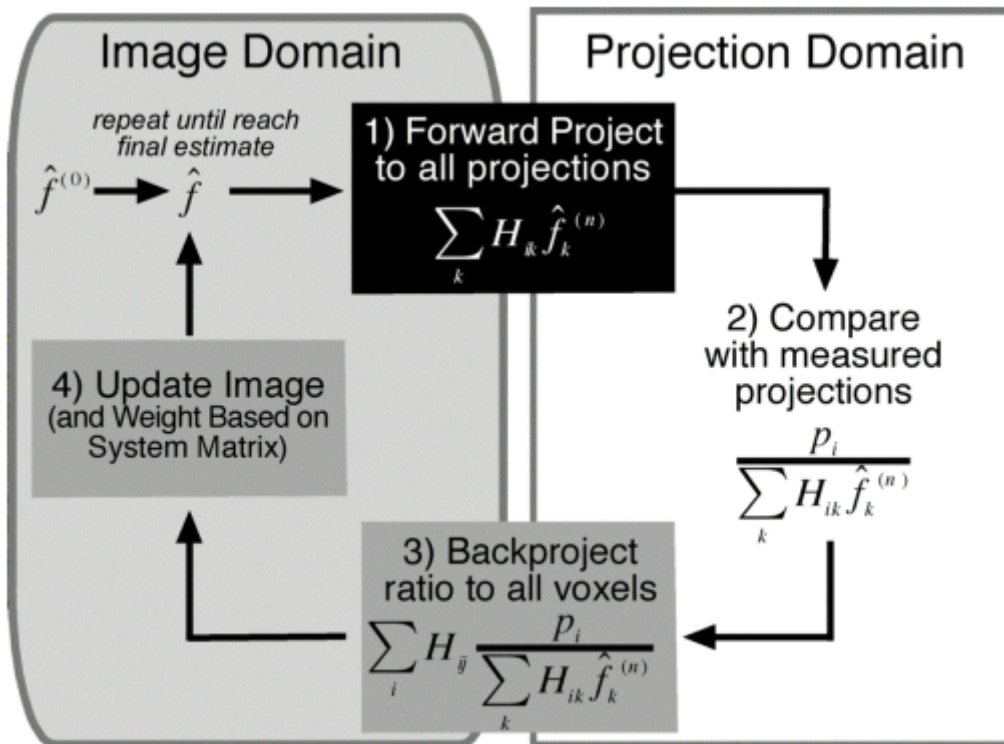
Figure 2.14: Flow diagram of the ML-EM algorithm (Alessio and Kinahan 2006)

more variance but the same bias level as ML-EM (Lalush and Tsui 2000).

$$f_j^{(n+1)} = \frac{\hat{f}_j^{(n)}}{\sum\limits_{i' \in S_b} H_{i'j}} \sum\limits_{i \in S_b} H_{ij} \frac{p_i}{\sum\limits_{k} H_{ik} \hat{f}_k^{(n)}} \tag{2.14}$$

with total B subsets and the backprojections steps summing over only the projections in subset S_b (Alessio and Kinahan 2006).

Due to the statistical nature of the photon detection, the PET images reconstructed by means of analytical or iterative methods are usually very noisy to be used in clinical practice. For this reason, regularization techniques need to be applied in order to give smooth images without high levels of noise. One of the most common forms of regularization is to apply a smoothing filter. The Frequency response of the detection system is finite and the signal power gradually roll off with higher frequencies but the noise power remains constant, so in general a trade-off should be made between the resolution and the noise in the image (Alessio and Kinahan 2006).

2.4   Hybrid Imaging

Most of the modern PET imaging systems are integrated with either a CT scanner or MRI, this way the anatomic structure can be added to the PET images as well as using this information for the attenuation correction of the images.

2.4.1   PET/CT

In order to accurately diagnose and localize the tumor as well as staging the malignancy, having an accurately aligned functional and anatomical image is beneficial. As mentioned earlier, the stand-alone PET imaging systems give the information about the distribution of the radiotracers in the body, yet except rare cases such as cardiac perfusion studies (Cherry, Sorenson and Phelps 2012) which shows some specific anatomical features, the organs structure is unknown or the acquired resolution of the organs are poor compared to other modalities like CT and MRI. Therefore, there is a need for two separate scans and then do the co-registration of the functional and anatomical images. Since the acquisitions are obtained in different sessions and different systems, spatial and temporal correspondence of the two sets of data is lost and image alignment is challenging.

With the advent of first hybrid PET/CT tomograph, which used a spiral CT and a partial ring on a common rotational support in a single gantry (Beyer et al. 2000), there is the possibility to acquire the functional and anatomical structure of the body in the same system and in a single scanning session. This provides accurately aligned images, with a good anatomical localization of the lesion of interest. The CT image is acquired under breath-hold condition with a high-counting-rate CT scan instead of a low-counting-rate radioactive rod,which improves the signal-to-noise ratio of the attenuation correction map. PET imaging takes 5-10 minutes for each bed position.

PET and CT components in a integrated PET/CT are usually both top end performance scanners so as to be able to produce high quality images in each modality. The CT part of a PET /CT can be also used as a diagnostic tool (higher mAs, contrast media). The combination of PET and CT gives much more information compared to the separate use of the two instruments. The main advantage resides in the possibility to fuse the morphological information obtained from the CT with the functional information from PET. Further advantages of the PET/CT combination are: the possibility to use CT information to correct PET data, to define the region of interest for the calculation of Standardized Uptake Values (SUV) or the correction of partial volume effect. On the other hand, the PET image completes the morphological information of a CT acting like a "metabolic" contrast agent, which is very important for example in the definition of the treatment planning in radiotherapy (Townsend, Beyer and Blodgett 2003; Ciernik et al. 2003).

The development of new scintillators such as lutetium oxyorthosilicate (LSO) with fast decay time and high density, together with the improved performance of Photomultipliers (PMTs) and reconstruction algorithms (Karp et al. 2008), paved the way for the appearance of time of flight (TOF) PET/CT systems (Figure 2.15). The concept of ToF assumes that the annihilation point of two photons originating from a single positron annihilation can be calculated from their travel time differences (Conti 2011; Surti and Karp 2016). With this additional information, the Signal-to-noise Ratio (SNR) in the reconstructed PET images can be improved significantly (Lecoq 2017).
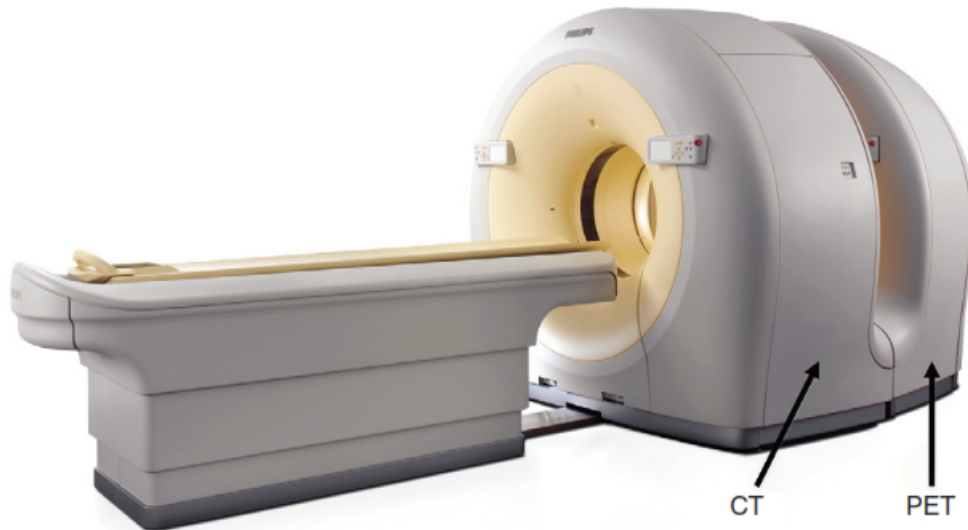
Figure 2.15: Philips Ingenuity TF PET/CT time of flight system (Cherry, Sorenson and Phelps 2012).

2.4.2   PET/MRI

Although the PET/CT system has proven its value in clinical procedure domain in giving useful information on functional and anatomical structures, yet the soft-tissue contrast is very limited and the patient is exposed to significant amount of radiation dose (Brix et al. 2005). Also the specificity and sensitivity of MRI is often higher than CT (Pichler, Judenhofer and Wehrl 2008; Müller-Horvat et al. 2006). One advantage of PET/MRI is the possibility of simultaneous imaging which can be of paramont importance in detection and correction of the motion effect (Buerger et al. 2012).

One of the complications in designing PET/MRI is related to the fact that PMTs are highly sensitive to the magnetic fields used in typical MR devices, affecting the electrons trajectory and therefore the the gain and event positioning of PMTs. Solid stated photo-detectors, such as the avalanche photodiode (APD) or Silicon Photomultipliers (SiPMs), are proven to be not affected by magnetic fields (Pichler et al. 1997) and are good choices to replace PMT as a scintillation light detector in PET/MRI.

Another challenging subject related to PET/MRI is the attenuation correction. Unlike CT images that can be used to determine gamma ray attenuation in matter, MRI images provide proton densities of the matter which is not related to the attenuation value in the tissue. Segmented attenuation correction maps (Beyer et al. 2016) among other approaches are being used as an alternative way of acquiring attenuation correction maps.

2.5   Data corrections in PET

In order to obtain quantitative PET images, several corrections need to be applied to the data. These corrections can be applied to the sinogram before the image reconstruction or they can be added to the system matrix in the iterative reconstruction algorithms,

with the second option being preferable to preserve the Poisson statistical nature of data.

Normalization

A typical PET system consists of thousands of detectors and each detector may vary from others in different aspects, such as: differences in sensitivity for counts emitted at different points of the FOV, differences in the detection efficiency of each detector pair, etc. If this variations are not properly compensated for, then normalization artifacts will appear in the reconstructed images. One usual approach in normalization correction is to expose all the detectors to the same amount of radiation (using a ^{68}Ga/ ^{68}Ge rod) and measure the variation in number of counts detected by each detector (Cherry, Sorenson and Phelps 2012).

Random Correction

Random events corresponds to events that belong to different annihilations but are captured in the same coincidence time window. Randoms coincidences are responsible for introducing an almost uniform background to the image, and as a consequence, they decrease the image contrast. One conventional solution to this problem is to delay the coincidence time window to an amount much bigger than its width and accepting the events that arrive during this time window. By doing this the true and scatter events are automatically discarded, and the distribution of random events will be obtained.

This number will be then subtracted from the coincidence events for each detector pair or added to the system model, with the second option being preferable.

Scatter Correction

Scattered events lead to a decrease in image contrast (hazy background concentrated toward the image center) and errors in the relationship between the activity distribution in the object and the image intensity. The fraction of the scattered events can be as high as 70% in 3D imaging (Figure 2.16). There are several techniques for scatter correction, such as for example: (1) empirical scatter corrections,which is considered as the simplest method is fitting an analytical function to the scatter tails outside the object (2) multiple energy window techniques, which uses the data recorded in energy windows set below or above the photo peak to estimate the contribution of the scattered photons within the photo peak window (3) convolution and deconvolution approaches that model the scatter distribution with the integral transformation of projections in the photo peak window and (4) simulation-based scatter correction, which takes into account the physics of photon interaction in matter and uses the map of attenuation coefficients in the medium to analytically or numerically (Monte Carlo simulation) estimate the scatter (Bailey et al. 2005).
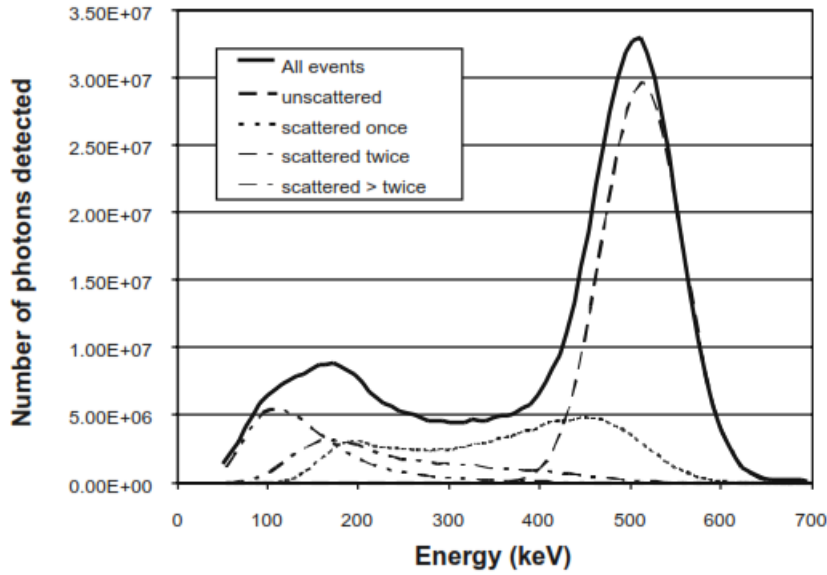
Figure 2.16: Monte Carlo simulation of a 20 cm diameter cylinder filled with positron emitters, shows the energy spectra of 511 KeV gamma rays, based on the number of scattering events that each photon has (taken from (Bailey et al. 2005)).

The Monte-Carlo simulation is the ideal research tool for scatter modelling and for the evaluation of scatter correction techniques. However, the computing requirements for a Monte-Carlo simulation led to the development of analytical simulation tools, which are based on approximations that improve the speed of operation. Of those, the Single Scatter Simulation (SSS) is the most used method for scatter correction nowadays. The SSS algorithm has been introduced in 1996 by Watson and colleages (Watson, Newport and Casey 1996) and modified (improved) versions of it (Watson 2000; Watson et al. 2004) are integrated nowadays in all the Siemens Biograph PET/CT and PET/MR systems.

Attenuation Correction

The photons produced from annihilation events can interact with the surrounding tissue by either depositing a portion of its energy (scattering) or by losing all the energy and getting absorbed. The probability of capturing the photon in the detector, depends on tissue density and the photon energy as well as the distance traveled by the photon. If the attenuation effect remain uncorrected, it leads to lower density tissues like lungs show higher activity and bones and deep lying structures show less amount of activity. Attenuation can be described using the equation:

$$I = I_0 e^{-\mu x} \tag{2.15}$$

where I is the transmitted intensity of photons and I_0 is the incident photon intensity. μ corresponds to the linear attenuation coefficient which is a function of the tissue density and the photon energy. In order to apply the corrections an attenuation correction map (μ map), which shows an absorption pattern for all the voxels in the image, is needed. The attenuation correction factor (ACF) can be obtained either by measuring the electron density (a transmission scan in stand-alone PET systems or a CT scan in PET/CT)

or segmentation of the proton density (using MR).

The transmission based ACFs can be obtained by acquiring a blank scan using a ^{68}Ga/ ^{68}Ge or ^{137}Cs rod sources (Ostertag et al. 1989; Keller, Svarer and Sibomana 2013) as a daily routine and a transmission scan for each patient. The attenuation is defined as:

$$ATN = \frac{blank}{transmission} \tag{2.16}$$

this procedure usually takes around 2-10 minutes (Meikle, Dahlbom and Cherry 1993).

The CT based attenuation maps which is used in hybrid PET/CT systems, employ the reconstructed CT images to acquire the ACFs, although a bilinear scaling of the photon attenuation is required to account for different photon energies between polychromatic X-ray (80-140 KeV) of the CT scan and monochromatic annihilation photons (511 KeV) (Carney et al. 2006).

The current PET/MRI systems use segmented attenuation correction maps (Beyer et al. 2016) as an alternative way of acquiring attenuation correction maps. Among other approaches are atlas-based methods and reconstruction-based attenuation maps (Nuyts et al. 2013).
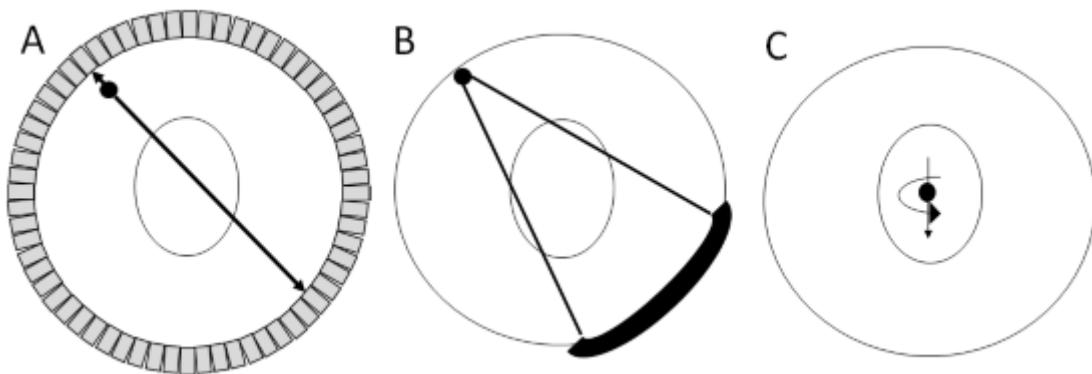
Figure 2.17: Three attenuation correction methods, (A) transmission scans in stand-alone PET systems, (B) CT scanning using PET/CT, (C) proton relaxation measurements which is followed by segmentation in PET/MR systems. (Lassen 2017).

Dead Time Correction

PET detectors will exhibit pile-up and dead time effects at high counting rates. The corrections must be applied in order to account for this effect otherwise the activity concentration will be underestimated. In most cases an empirical model is applied in which the counting rate is measured as a function of radioactivity concentration for different object sizes and at different energy thresholds.

2.6   Motion in PET and Gating

Respiratory and cardiac motion are two sources of image blurring in the thoracic images. This problem is raised in PET imaging because capturing enough photons counts for image generation needs several minutes. The breathing and cardiac movements will affect the quality of the PET images in two ways: introducing image blur and image artifacts due to wrong attenuation correction. Image blur is introduced in the image as the organs tend to move during respiration specially in the thoracic and abdominal region. The amount of blur is proportional to the magnitude of thoracic movement and is responsible for the loss of contrast.

The usual respiratory motion in the diaphragm is in the order of 2-3 cm. This amount of motion causes an overestimation of the lesion size by a factor of 2, and an underestimation of the tracer concentration up to 30% (Kesner et al. 2014; Liu, Alessio and Kinahan 2011).

CT images can be obtained in less than a second, and therefore hardly suffer from the effects of respiratory motion, since the thoracic movements can be avoided by holding the breath during the scanning time. Cardiac motion, on other hand, can be corrected using the cardiac Electrocardiogram (ECG) gating. In the presence of motion, the co-registration of CT and PET images may be not accurate and as a result, the activity in a tissue may be corrected with a wrong tissue density, leading to image artifacts in the PET images. In general, many negative effects can be attributed to the motion during the PET image acquisition such as wrong diagnosis of tumor stage, incorrect localization of the tumor and miscalculation of the dose uptake ratio. Therefore there is a need for address these problems in PET imaging.

2.6.1   Respiratory and cardiac motion detection

The standard method for cardiac gating consists of using the electrocardiogram (ECG) signals in sync with the PET data. Each cardiac cycle contains a very low number of counts in order to make the image but the combination of all the cardiac cycles can produce acceptable images.

For respiratory gating, there are several methods to track the respiratory signal that use external markers and have been developed and can be implemented such as: (1) A sensor to detect the pressure changes during the respiration. (2) A belt around the patient's abdomen to track the thoracic motion. (3) A sensor to detect the temperature change of air flowing in the lungs (Büther et al. 2009). However, external tracking methods have several limitations that hamper their accuracy and applicability in clinical settings. First, most of these methods detect external motion, which does not necessarily correspond to the internal motion of the organs (Giraud and Houle 2013). In addition, respiratory external markers frequently require time-consuming calibrations (Lassen et al. 2017) and may present malfunctions during the acquisition (Gould 2017). In this context, data-driven methods are promising alternatives to the use of external markers (He et al. 2008).

There are two known types of methods to use in data-driven gating. (1) Methods that derive the respiratory or cardiac signal directly from the acquired PET rawdata (self-gating methods) (Büther et al. 2009) and (2) methods that make use of MRI navigators simultaneously acquired in combined PET/MR systems.

In relation to the self-gating methods that use the acquired PET raw data, two implementations are the most common: (1) Sensitivity method, which uses the fact that the sensitivity profile of the scanner changes as the activity source moves in the axial direction of the device. (2) The center of mass method (CoM). In this approach a histogram is made from number of counts against axial coordinate of the scanner and it is done in small periods of time. This way as the object moves in the axial direction, the histograms can be used to determine the center of mass for each period.

MR-based motion estimation techniques aim to find motion models that shows the relationship between the motion of interest (motion of the internal organ) and a surrogate data (movements of skin) and use this model to estimate the actual motion based on the subsequent acquisition of surrogate data (McClelland et al. 2013). Most of the approaches fall into two categories: (1) precalibrated motion model, in which the dynamic MR data is used to build a patient-specific motion model before or during the first minutes of PET data acquisition and then use the surrogate data during the PET acquisition. (2) simultaneous motion models that use the MR data during the whole PET acquisition to estimate the motion (Munoz et al. 2016).

2.6.2   Motion compensation techniques

The easier and most used technique for reducing the negative effects of respiratory and/or cardiac motion is known as gating. This technique consists in dividing the cardiac contraction and/or respiration into several phases, and therefore limiting the respiratory and/or cardiac motion effects.

Gating-based methods correspond to dividing the acquired raw PET data into several bins and each of these bins are representative of the information acquired in some specific respiratory/cardiac phase (see Figure 2.18). This way there will be less motion in the images reconstructed using each phase, but also lower statistics and as a result, reduced contrast because only a portion of counts has been used to reconstruct the images for each phase (Gigengack et al. 2015).
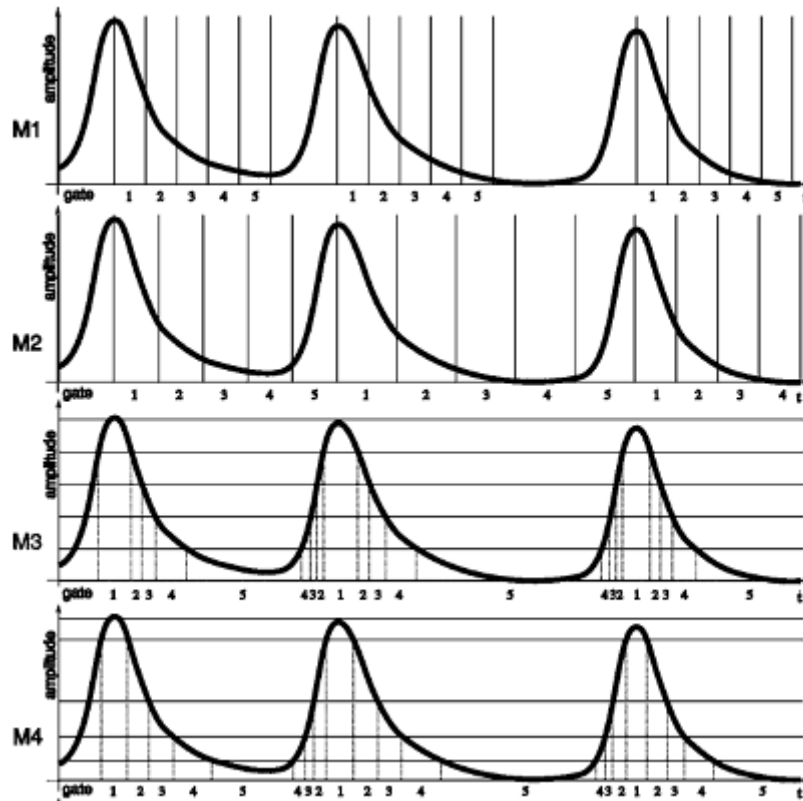
Figure 2.18: Different respiratory gating approaches.From top to bottom, M1:time-based equal gates, M2:time-based variable gates, M3: amplitude-based equal gates, M4: amplitude-based variable gates. (Dawood et al. 2007).

As mentioned before, gating approaches have the disadvantage of using only fractions of the acquired data, thus, resulting in increased noise levels in the resulting images. For this reason, motion compensation (MoCo) approaches have generated substantial interest. Among the motion-compensation techniques, there are two that become the standard correction approaches: reconstruct-transform-average (RTA) which reconstruct the images for each gate and then transform them to a reference image and does the averaging (Figure 2.19). The second method is called motion-corrected image reconstruction (MCIR) (Figure 2.20) which includes the information of the respiratory motion in the system matrix during the image reconstruction (Munoz et al. 2016).
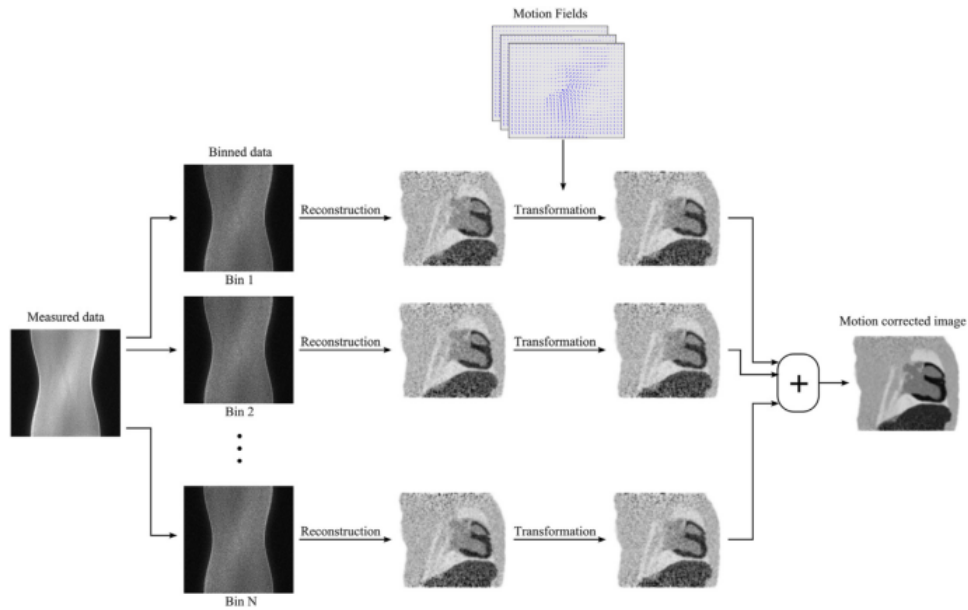
Figure 2.19: RTA method, a postreconstruction registration approach. The data is going to be binned between several gates with less motion. Each gate is reconstructed separately and are transformed to a reference gate. In the last step all the images are summed together and averaged to obtain the motion-free image (Munoz et al. 2016).
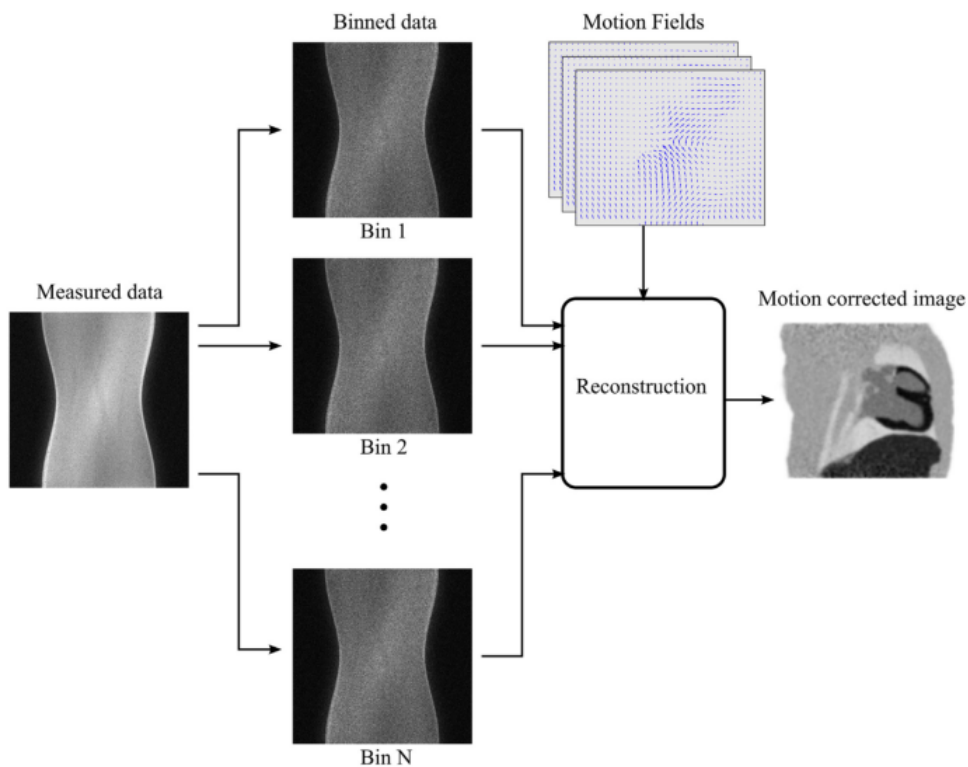
Figure 2.20: MCIR technique. The motion information is included in the reconstruction algorithm which modifies the emission and attenuation maps (Munoz et al. 2016).

Chapter 3

Materials and Methods

In this chapter we will describe the tools employed to carry out the goals proposed in this master thesis. *Sections 3.1* and *3.2* shows the description of the imaging devices used to acquire the data for the phantom and patient experiments. The storage format used for the PET data acquired in this work is described in *section 3.3*, while the data-driven motion detection technique used in this thesis is described in *section 3.4*. Furthermore, the motion-limiting techniques evaluated in this thesis are described in *section 3.5*. Finally, the phantom experiments performed in this thesis and their evaluation is described in *section 3.6*, while the patient datasets included in the study are described in *section 3.7*.

3.1   mCT time of flight PET/CT scanner

The Biograph mCT (Siemens Medical Solutions USA, Inc) is a PET/CT system with the time of flight (TOF) capability which helps to improve the quality of PET images. Using lutetium-oxyorthosilicate (LSO) with reasonable stopping power and decay constant ($\approx$ 40 ns) gives this system the power to further localize the positron annihilation point along the LOR and as a consequence gives a better signal to noise ratio (SNR).

The CT scanner of mCT device consists of a 128-slice scanner (SOMATOM Definition AS+, Siemens Medical Solutions USA, Inc.) which has an aperture of 78 cm with the ability of acquiring images with 0.5-20 mm. The tube current can be adjusted between 20 and 800 mA and the tube voltage of 80, 100, 120, 140 kV (Jakoby et al. 2011). The PET component of the Biograph mCT consists of 4 rings with each ring having 48 blocks with 13×13 crystals (4 mm $\times$ 4 mm $\times$ 20 mm) each. The axial field of view (FOV) is 21.8 cm which gives 109 image planes, each one having 2 mm spacing. The maximum fan angle of acceptance of 13.2° for each detector results in a high sensitivity and count rate. The energy resolution is 11.5 $\pm0.2\%$ with lower energy limit of 435 keV and the time resolution of 4.1 ns which is effective to reduce the number of scattered events (Table 3.1).

Parameter	mCT
Detector material	LSO
Detector element dimension	$4 \times 4 \times 20$ mm
Detector element per block	169
Total # of detector elements	32448
patient bore	78 cm
Tunnel length (PET and CT)	100 cm
Axial FOV	218 mm
Image planes	109
Plane spacing	2 mm
Max. detector ring difference	49
Angle of acceptance	13.2°
Coincidence time window	4.1 ns
Energy window	435-650 keV

Table 3.1: Biograph mCT specifications (Jakoby et al. 2011).

The performance of the mCT system, evaluated using the NEMA NU-2 2007 method, is as follows (see (Jakoby et al. 2011)): The sensitivity at the center of the FOV is 9.7±0.2 (kcps/MBq) and the axial and transversal spatial resolutions are the same (4.4 ±0.1 mm) for a point source with 1 cm radial distance from center of FOV. The scatter fraction is 33.2 ±0.7% for low activity concentrations. The spatial, time and energy resolution as a function of single count rate (up to 55 Mcps) is 4.1 ±0.0 (FWHM mm), 527.5 ±4.9 (FWHM ps) and 11.5 ±0.2 (FWHM %) respectively. The Noise Equivalent Count Rate (NECR) peak is 180.3 ± 7.8 kcounts/s at 28.3 ± 0.6 kBq/mL.

3.2 Biograph mMR Whole-body PET/MR scanner

The Biograph mMR system used in this study is a whole-body integrated PET/MR with the ability of simultaneous data acquisition, which allows for the acquisition of several MR sequences without extending the examination time. The MR component of this system comprises a 3 Tesla niobium-titanium superconductor magnet, a whole body gradient coil which is actively shielded (amplitude of 45 mT/m and slew rate of 200 T/m/s) and a radiofrequency body coil (transmitter bandwidth of 800 kHz and peak power of 35 kW) (Delso et al. 2011).

A PET detector assembly is installed between radiofrequency coil and the gradient coil, with 8 rings of 56 detector blocks, 8×8 lutetium oxyorthosilicate crystals of $4 \times 4 \times 20$ mm per block, coupled to an array of 3×3 APDs. With energy resolution of 14.5% and energy window of 430-610 KeV. The time resolution and coincidence window of 2.93 ns and 5.86 ns respectively. The transaxial field of view of the PET system is 59.4 cm and the axial field of view is 25.8 cm. Specifications of the PET component of the biograph mMR is summarized in table 3.2.

The performance of the mMR system evaluated using the NEMA NU-2-2007 protocol

for the PET part of the system and the quality control manual of the American College of Radiology (ACR) for the MR part (values are taken from (Delso et al. 2011)). The spatial resolution for both transverse and axial, is measured 4.3 mm full width at half maximum (FWHM) at 10 mm radial distance from the center of FOV. The peak Noise Equivalent Count Rate (NECR) had a value of 184 kcps for activity concentration of 23.1 kBq/mL. The scatter fraction at peak NECR was 37.9% and the system sensitivity along the center of the scanner was measured 15.0 kcps/MBq.

Parameter	mMR
Detector material	LSO
Detector element dimension	$4 \times 4 \times 20$mm
Detector element per block	8×8
Detector rings	8
APDs per block	3×3
Axial FOV	25.8 cm
Radial FOV	58.8 cm
Image planes	127
Coincidence time window	5.86 ns
Energy window	430-610 KeV

Table 3.2: The specifications of the PET component of the biograph mMR (values from (Delso et al. 2011)).

3.3 List-mode and sinogram format

The raw-data acquisition is in list-mode format, in which the file is read in 32-Bit packets (Jones 1999) with every packet being either an event packet or a tag packet.

TXXX XXXX XXXX XXXX XXXX XXXX XXXX XXXX

With T=1 corresponding to a informative tag (time marker, dead-time tracking, gantry motions, ...), and T=0 indicative of a event packet. The available tags are:

10XX XXXX XXXX XXXX XXXX XXXX XXXX XXXX
Gantry Motions and Positions

1100 XXXX XXXX XXXX XXXX XXXX XXXX XXXX
Time Marker/ Dead-Time Tracking

1110 XXXX XXXX XXXX XXXX XXXX XXXX XXXX
Patient Monitoring: (Gating/Physiological /Head Tracking)

1111 XXXX XXXX XXXX XXXX XXXX XXXX XXXX
Control / Acquisition Parameters

0PBB BBBB BBBB BBBB BBBB BBBB BBBB BBBB

Here, P=1 means a prompt and P=0 is a delayed event. The other 29 Bits (B) specify the Bin address.

The sinogram format of the Biograph mCT (Table3.3) comprises of 400 radial bins, 168 angular bins, and 621 slices in total, from which 109 are direct planes and 512 oblique planes, and also 13 TOF bins (312ps wide). The maximum ring difference (MRD) is ±49. A summary of the Biograph mCT sinogram parameters are gathered in Table 3.3.

Parameter	Value
Total number of rings	55
Maximum ring difference(MRD)	49
Axial compression(SPAN)	11
Number of segments	9
Sinogram projections(radial bins)	400
Sinogram views(angular bins)	168
Number of sinograms	621
Sinograms per segment	{109,97,97,75,75,53,53}

Table 3.3: Sinogram format for the Biograph mCT system.

For the biograph mMR, the sinogram formats consists of 344 radial bins and 252 angular bins, with original list mode data comprising of 4084 and 837 for no axial compression and axial compression respectively. Table 3.4 summarizes the sinogram parameters for biograph mMR system.

Parameter	With axial compression	No axial compression
Total number of rings	64	64
Maximum ring difference (MRD)	60	60
Axial compression (SPAN)	11	1
Number of segments	11 (0,-1,+1,...,-5,+5)	121 (0,-1,+1,...,-60,+60)
Sinogram projections (radial bins)	344	344
Sinogram views (angular bins)	252	252
Number of sinograms	837	4084
Sinogram per segment	{127,115,115,93,93,71,71, 49,49,27,27}	{64,63,63,62,62,61,61, 60,60,59,59,58,58,57,57,56,56, 55,55,54,54,53,53,52,52,51,51, 50,50,49,49,48,48,47,47,46,46, 45,45,44,44,43,43,42,42,41,41, 40,40,39,39,38,38,37,37,36,36, 35,35,34,34,33,33,32,32,31,31, 30,30,29,29,28,28,27,27,26,26, 25,25,24,24,23,23,22,22,21,21, 20,20,19,19,18,18,17,17,16,16, 15,15,14,14,13,13,12,12,11,11, 10,10,9,9,8,8,7,7,6,6,5,5,4,4}

Table 3.4: Sinogram parameters of biograph mMR system.

3.4 Data-driven Motion Detection

The analysis of the count rates is done every 200 ms in the listmode file (equation 3.1) (Büther et al. 2009):

$$T(t) = (P(t) - D(t)).exp(\lambda t) \qquad (3.1)$$

where P(t) corresponds to the number of prompts and D(t) is the number of delays. This difference gives an estimation of the true events. The $exp(\lambda t)$ is to account for the decay factor over time with λ being the decay constant of the radionuclide.

The method for extraction of the respiratory motion uses a VOI surrounding the selected organ or lesion using the reconstructed static image. This selected region is then segmented and forward projected (Figure 3.1) to give a histogram of the true events as a function of the axial slices for every time frame. This way as the organ moves along the axial direction, every histogram contains information about the respiratory motion which is extracted using the center of mass method (equation 3.2) (Büther et al. 2009):

$$Center\ of\ mass(t) = \frac{\sum_{i} i.T(i,t)}{\sum_{i} T(i,t)} \tag{3.2}$$

where i and t are the number of the axial slice and t is the time frame respectively and T refers to the histogram.
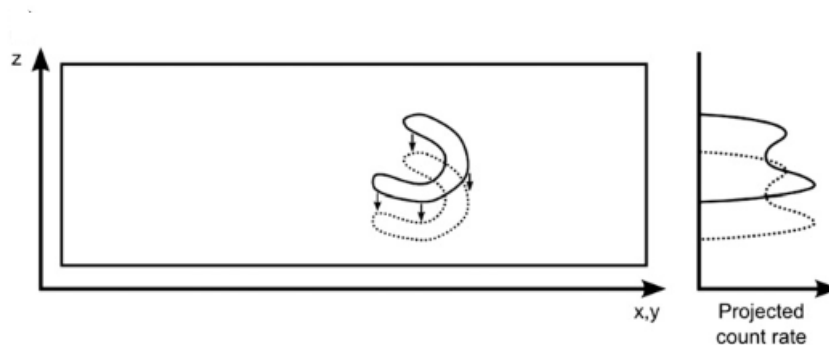
Figure 3.1: Center of mass method. The segmented VOI is forward projected for different time frames, giving two histograms with different center of mass. (Büther et al. 2009).

Due to the statistical nature of PET imaging (positron decay process, random and scattered events, ...), the raw respiratory signal is noisy. In general there will be two peaks for the respiratory and cardiac movement in the frequency spectrum, with $f_{resp} \leq 0.4$ Hz and $f_{card} \approx 1.2$ Hz. The approach used in this project to obtain the respiratory signal includes: 1) A frequency filtering of the respiration by putting all the other frequencies to zero and 2) using a moving average filter (0.3s) to exclude the frequencies above 1Hz (Lassen 2017).

3.5   Gating and Motion Compensation

The gating approach used in this study is the amplitude based binning rather than the time based method since it shows a better performance in capturing the respiratory motion (Dawood et al. 2007). An amplitude-based equal gates binning is applied to the respiratory signal with moving average filtering using 10-95 percentile of the amplitude (in order to deal with irregular amplitude variability in the amplitude in patient data). For the frequency filtered signal the approach includes the amplitude based variable gates binning in a way that every gate contains the same number of events. Images for each gate are reconstructed using the vendor reconstruction software (e7-tools, Siemens). Figure 3.2 shows a comparison between the data driven gating and a standard clinical approach without motion compensation.
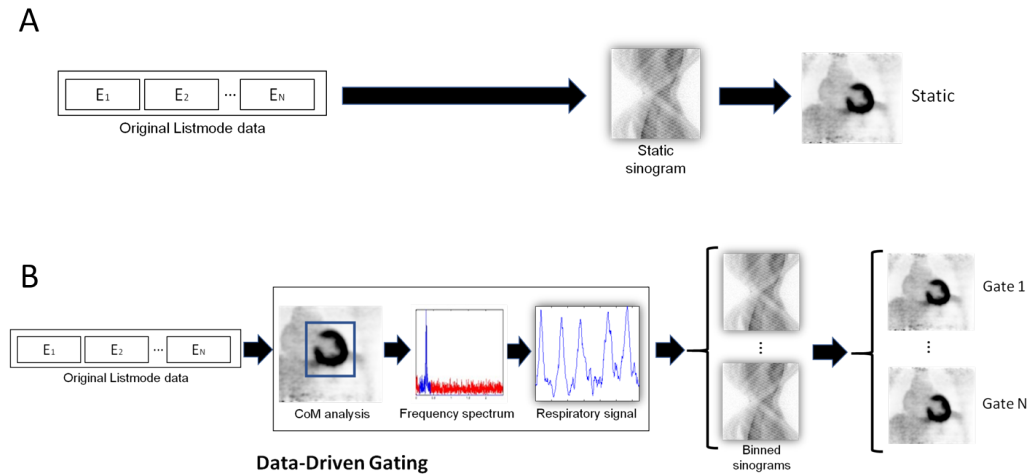
Figure 3.2: Data-driven motion detection. A: Standard clinical reconstruction set-up, employs the acquired listmode file with all stored events (E1, E2,..., EN) during the acquisition. The resulting reconstruction has respiratory motion embedded in images, thus, degrading the image quality. B: The proposed data-driven gating extracts the respiratory signal from the listmode file, followed by a respiratory gating of the acquired data (Lassen 2017).

For motion compensation of the gated images we used the Reconstruct-Transform-Average (RTA) approach, which incorporates the motion information after the gated image reconstruction process. In this approach, the different gates are reconstructed independently, and then transformed to a reference gate and averaged (Picard and Thompson 1997). The RTA-MoCo algorithm implemented in the Software for Tomographic Image Reconstruction (STIR) (Thielemans et al. 2012; Tsoumpas et al. 2013) was used in this work. The motion vector fields which are used for the RTA-MoCo approach were estimated from the co-registration of previously reconstructed gated PET images to a chosen reference gate. This co-registration process was done in Matlab, using the Medical Imaging Registration Toolbox software (Myronenko and Song 2010).

3.6 Phantom-data

3.6.1 Phantom Specifications

Two phantom studies were evaluated in this study, both acquired in a PET/CT system (Siemens Biograph mCT) at a collaborating site in Münster (Germany) (Figure 3.3). The specifications of this phantom are listed below (Fieseler et al. 2013; Bolwin et al. 2018):

- Elastic lungs

- Liver compartment

- Four coronary holders for plaque simulations

- One holder for tumor simulations

- Double-layer myocardium

This phantom is equipped with a pneumatic system for simulations of respiratory and cardiac motion with the maximum axial motion of 3 cm. The background activity was set to 4 kBq/mL, while the small plaque-type lesions were filled with a lesion-to-background ratio of 70:1. The respiratory motion range was set to 2 cm, while the cardiac motion was set to a maximum change of 60 mL blood volume.

The following acquisitions were performed and analyzed:

1. **Experiment 6001:** Respiratory + Cardiac motion. 16 min Listmode acquisition. No heart uptake. Respiratory cycle 4.6 s (1.6 s inspiration, 3.0 s expiration) Cardiac cycle 1.2 s (0.6 s systole, 0.6 s diastole).

2. **Experiment 7001:** Respiratory + Cardiac motion. 30 min Listmode acquisition. Heart-to-background ratio 5:1. Respiratory cycle 4.6 s (1.6 s inspiration, 3.0 s expiration) Cardiac cycle 1.9 s (0.9 s systole, 1.0 s diastole).
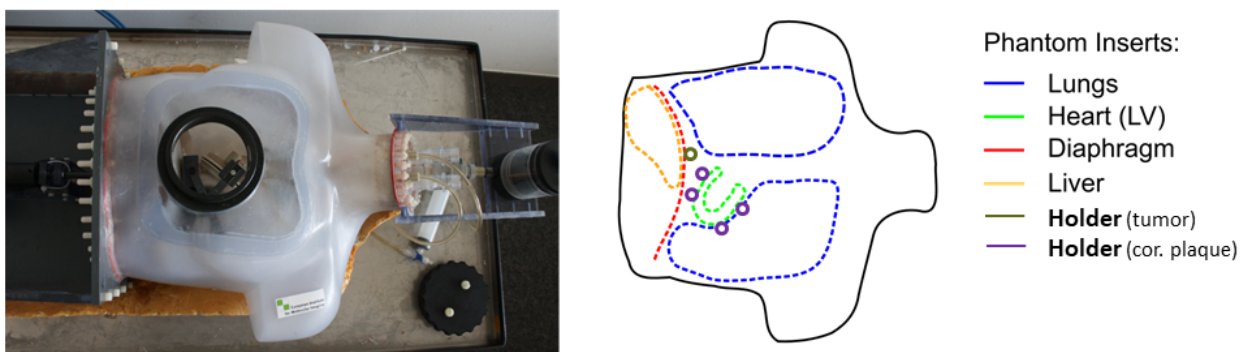
Figure 3.3: Picture and scheme of the human thorax phantom with several phantom inserts (Fieseler et al. 2013).

The number of stored prompts, randoms and effective true coincidences in these two acquisitions is reported in Table 3.5.

Patient	Duration (sec)	Prompts	Randoms	Trues
Experiment 6001	960	14.0×10^7	2.40×10^7	11.6×10^7
Experiment 7001	1800	21.2×10^7	3.20×10^7	18.0×10^7

Table 3.5: Acquisition duration and number of stored coincidences for the phantom acquisitions evaluated in this work.

3.6.2   Evaluations and figures of merit

The performance of the data-driven motion detection method will be dependent on the choice of the Region of Interest (ROI) used to extract the respiratory signal. The optimal ROI will be the one with most vivid respiratory motion within the ROI and with the

higher contrast in the non attenuation-corrected (NAC) PET image. ROIs centered in the diaphragm and myocardium, and with different sizes, are considered in this work (see Figure 3.4).

<div align="center">(a)   (b)</div>
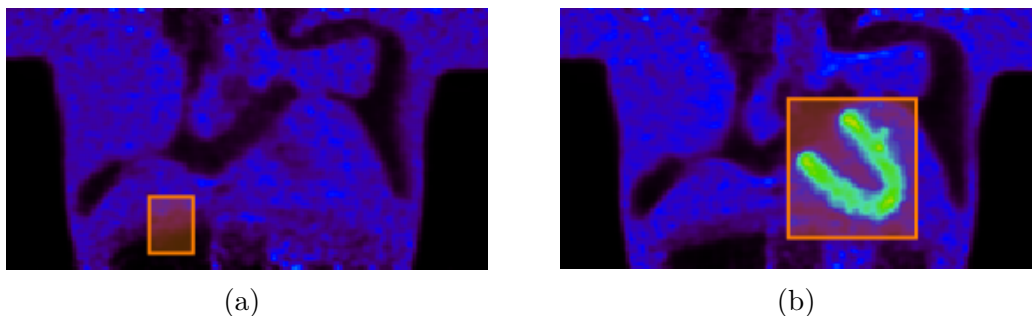
Figure 3.4: ROI selected for (a) Diaphragm and (b) Myocardium

Upon extracting the respiratory signal for each of these different regions, we compare the result using different figures of merit, which are defined as follows.

The correlation between the data-driven extracted signals and the external signal is evaluated using the spearman's rank correlation coefficient.

$$r_s = \frac{\text{cov}(\text{rg}_x, \text{rg}_y)}{\sigma_{\text{rg}_x} \sigma_{\text{rg}_y}}$$

with x and y being two respiratory signals and rg_x and rg_y are their ranks.

The signal to noise (SNR) ratio is defined as the ratio of signal power to the noise power, in the frequency spectrum. In this work, it is defined by the expression:

$$\text{SNR} = \frac{\max(0.1 < f < 0.5)}{\text{mean}(2 < f < 3)} \tag{3.3}$$

with f being the frequency calculated from the frequency spectra of the respiratory signal.

On the other hand, we also evaluated the contrast to noise ratio (CNR) in the defined ROI, measured in the NAC PET images. Here, the definition of CNR is similar to the definition given above for the SNR, with the difference that here the CNR is evaluated directly in the reconstructed images, while the SNR above was defined for the frequency spectrum. We evaluated 3 different criteria for CNR evaluation, defined as follows:

$$\text{CNR}_{\text{means}} = \frac{\text{mean(segmented ROI)}}{\text{mean(background noise)}} \tag{3.4}$$

$$\text{CNR}_{\text{max\_noise}} = \frac{\text{max(segmented ROI)}}{\sigma(\text{background noise})} \tag{3.5}$$

$$\text{CNR}_{90\_10} = \frac{10\_\text{highest\_ROI}}{10\_\text{lowest\_ROI}} \tag{3.6}$$

Here, the segmented ROI obtained using a binary mask with values below 41 % of the maximum gray value set to zero.Background noise consists of all the pixels in the ROI

which do not belong to the segmented area. The symbol σ corresponds to the standard deviation of the specific pixels gray values. $\text{CNR}_{\text{means}}$ is the ratio of mean value of segmented area and mean value of background noise. $\text{CNR}_{\text{max\_noise}}$ measures the ratio of maximum value in the segmented pixels over the standard deviation (σ) of the background noise and $\text{CNR}_{\text{90\_10}}$ is indicative of ratio of mean value of 10 % of the pixels with highest gray values and 10 % of the pixels with lowest gray values. The figures of merit presented above will be employed to show the correlation of SNR vs CNR and SNR vs volume.

The performance of the motion-limiting techniques (gating and RTA-MoCo) will be evaluated by direct comparison of the static images with the reference gate image and the RTA-MoCo image. Three different figures of merit will be evaluated for each of the above mentioned images:

$$\text{LBR}_{\text{max}} = \frac{\text{max(lesion)}}{\text{mean(background)}} \tag{3.7}$$

$$\text{LBR}_{50} = \frac{\text{mean(lesion)}}{\text{mean(background)}} \tag{3.8}$$

$$\text{Noise} = \frac{\sigma(\text{background})}{\text{mean(background)}} \times 100\% \tag{3.9}$$

Where LBR_{max} corresponds to the ratio of the maximum value of the lesion and mean of the selected background (uniform gray value and no drastic changes of contrast). LBR_{50} is the ratio of the mean value of the lesion which is selected using the threshold segmentation of 50 %, meaning that every gray value inside the ROI which is below 50 % of the maximum value will be set to zero. The noise value is specified using the ratio of the standard deviation of the selected background and mean of the background.

3.7   Patient-data

Evaluations of the detected respiratory signal and figures of merit were performed on 12 patients with lung cancer. The specifications of the patients and the data acquisitions are summarized in Table 3.6, while the number of acquired counts for each patient are summarized in Table 3.7.

The radiotracer injected for the patients was ^{18}F-FDG and the image reconstructions are performed using OSEM iterative algorithm with PSF resolution modeling with 24 subsets and 3 iterations. All reconstructed images were corrected for normalization, deadtime, attenuation, scatter, frame-length and randoms. Subsequently a post reconstruction gaussian filter (5 mm full with at half maximum (FWHM)) is applied to the images. The obtained images consist of $344 \times 344 \times 127$ voxels.

The respiratory signal was extracted using the center of mass (CoM) method with the sample time of 100 ms and the raw respiratory signals are filtered using only the moving average filtering method.

Patient	Dose (MBq)	Injection time	Acquisition time	Sex	Age	Weight (kg)	size (cm)
PT 54	239	12:09:00	14:06:49	F	82	60	158
PT 95	209	10:38:00	12:37:32	F	63	51	155
PT 96	250	11:27:00	13:14:14	M	71	63	179
PT 105	292	11:28:00	13:17:52	M	75	75	176
PT 109	258	11:44:00	13:31:41	M	70	65	176
PT 112	250	12:54:00	14:37:53	F	75	63	155
PT 115	343	11:33:00	13:29:07	M	64	86	185
PT 117	234	10:38:00	12:32:43	F	60	58	171
PT 121	328	09:43:00	11:54:49	M	57	85	183
PT 123	241	11:58:00	13:50:58	M	81	60	171
PT 124	283	12:43:24	14:46:53	F	72	71	165
PT 125	276	10:56:24	12:42:04	M	76	70	186

Table 3.6: Specifications of the patient data used in this work.

Patient	Duration (sec)	Prompts	Randoms	Trues
PT 54	600	19.6×10^7	9.40×10^7	10.2×10^7
PT 95	600	15.6×10^7	6.20×10^7	9.40×10^7
PT 96	80.0	2.60×10^7	1.10×10^7	1.50×10^7
PT 105	114	5.00×10^7	2.60×10^7	2.40×10^7
PT 109	600	23.0×10^7	10.5×10^7	12.5×10^7
PT 112	110	4.00×10^7	1.90×10^7	2.10×10^7
PT 115	600	24.3×10^7	11.7×10^7	12.6×10^7
PT 117	600	17.7×10^7	7.40×10^7	10.3×10^7
PT 121	600	18.0×10^7	7.9×10^7	10.1×10^7
PT 123	138	4.60×10^7	2.04×10^7	2.55×10^7
PT 124	600	19.3×10^7	8.3×10^7	11.0×10^7
PT 125	178	7.80×10^7	3.70×10^7	4.10×10^7

Table 3.7: Data acquisition length and number of acquired counts in the patients analyzed in this work.

3.7.1   Evaluations and Figures of Merit

As with the phantom experiment, the performance of the data-driven method depends on the choice of the ROI used to extract the signal. The ROIs used in this study are selected based on the higher contrast they have with the background and the amount of respiratory movement they have. On this basis the suitable candidates used are the ROIs of different volumes centered in myocardium, lesion and the diaphragm. After extracting the respiratory signal for each case, the SNR ratio and the CNR values are calculated for each case and the correlation between the SNR vs CNR, SNR vs volume and SNR vs detected motion is evaluated. These figures-of-merit are calculated as described in *section 3.6.2*. The calculations of the CNR is done on the NAC images. Figure 3.5 shows the ROIs chosen for the patient data.

The performance of the motion-limiting techniques is also evaluated by following the figures-of-merit described in *section 3.6.2*.

(a)   (b)
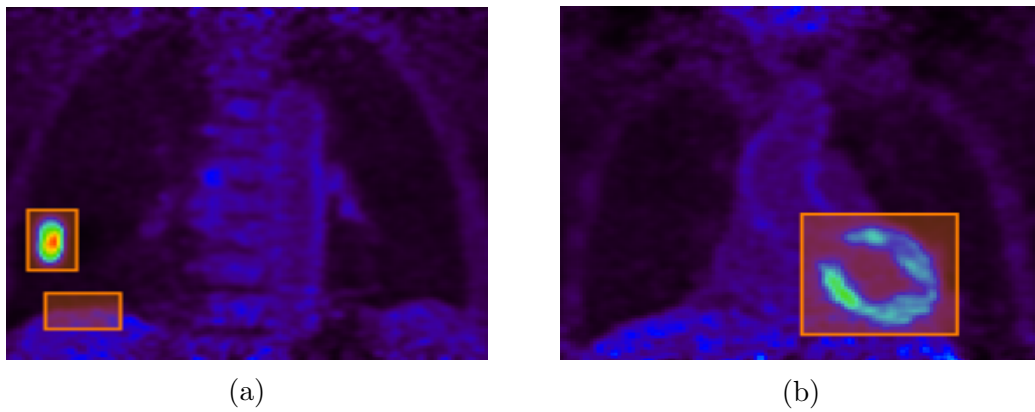
Figure 3.5: ROIs used for study of the patient data. (a) instances of ROIs selected for lung lesion and diaphragm. (b) ROI selected for the myocardium

Chapter 4

Results

4.1 Experimental Phantom Results

In this section, the results of the phantom experiments are presented, which corresponds to two different acquired datasets. **Experiment 6001** represents the phantom acquisition without heart uptake, while **experiment 7001** represents the phantom acquisition with heart uptake.

4.1.1 Validation of Respiratory Motion Detection

The frequency spectra for the phantom experiments are obtained using the Fast Fourier Transform (FFT) on the data-driven signal and external respiratory signal obtained with the Anzai system. Figure 4.1 depicts these two frequency spectra for both cases. For each experiment, both spectra present a very strong peak at frequency $f_{resp} \approx 0.21$ Hz, which corresponds to the periodic respiratory signal of 4.6 s used during the phantom experiments. The external signals and data-driven signal for experiment 7001 present several harmonic peaks at frequencies of $f \approx 0.42$ Hz, $f \approx 0.63$ Hz, etc; which are not observed in the data-driven signals for experiment 6001.

The signal-to-noise ratio (SNR) in the frequency spectra is 33.2 for the data-driven signal and 2069 for the external Anzai signal for experiment 6001 and for experiment 7001 the values are 47.8 and 3549 for data-driven and external Anzai signal respectively.
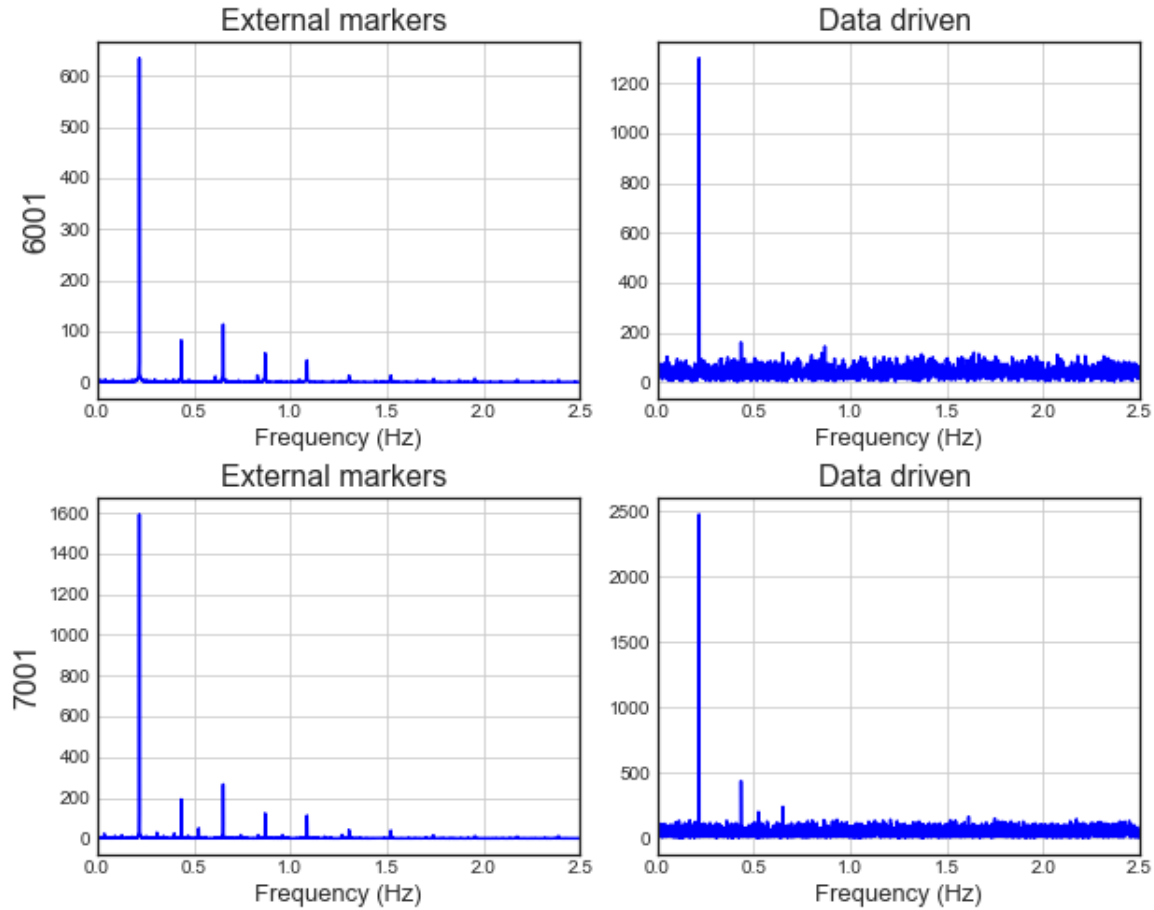
Figure 4.1: Frequency spectra for data-driven and external signals. **Top:** experiment 6001. **Bottom:** experiment 7001.

The entire data-driven and external respiratory signals, for the 16 min acquisition time of experiment 6001, are presented in Figure 4.2 (a). Furthermore, the comparison of the two signals in 100 seconds time periods are shown in Figure 4.2 (b) to (e). The Data-driven respiratory signal is acquired from the frequency filtering of the raw respiratory signal in order to keep the respiratory frequency using an ideal narrow band pass filter and put other frequencies to zero and then applying Inverse Fast Fourier Transform (IFFT) on the frequency spectrum. The data driven and external signals for 30 min acquisition time of experiment 7001 are depicted in Figure 4.3, with the same procedure and filtering as the experiment 6001 and with similar results.

The filtered respiratory signal using the moving average filter is depicted in Figure 4.4, together with the frequency filtered and the external respiratory signals for both experiments. Moving average filtered signal is usually employed in patient datasets, because it is more convenient to model irregularities in the respiratory cycle of the patient, such as breath holds or differences in the respiratory frequency during the acquisition.

The spearman's rank correlation coefficient r_s was 0.9 and 0.93 between the external and the frequency filtered signals and 0.76 and 0.79 between the external and the moving average filtered signals for experiment 6001 and 7001 respectively.
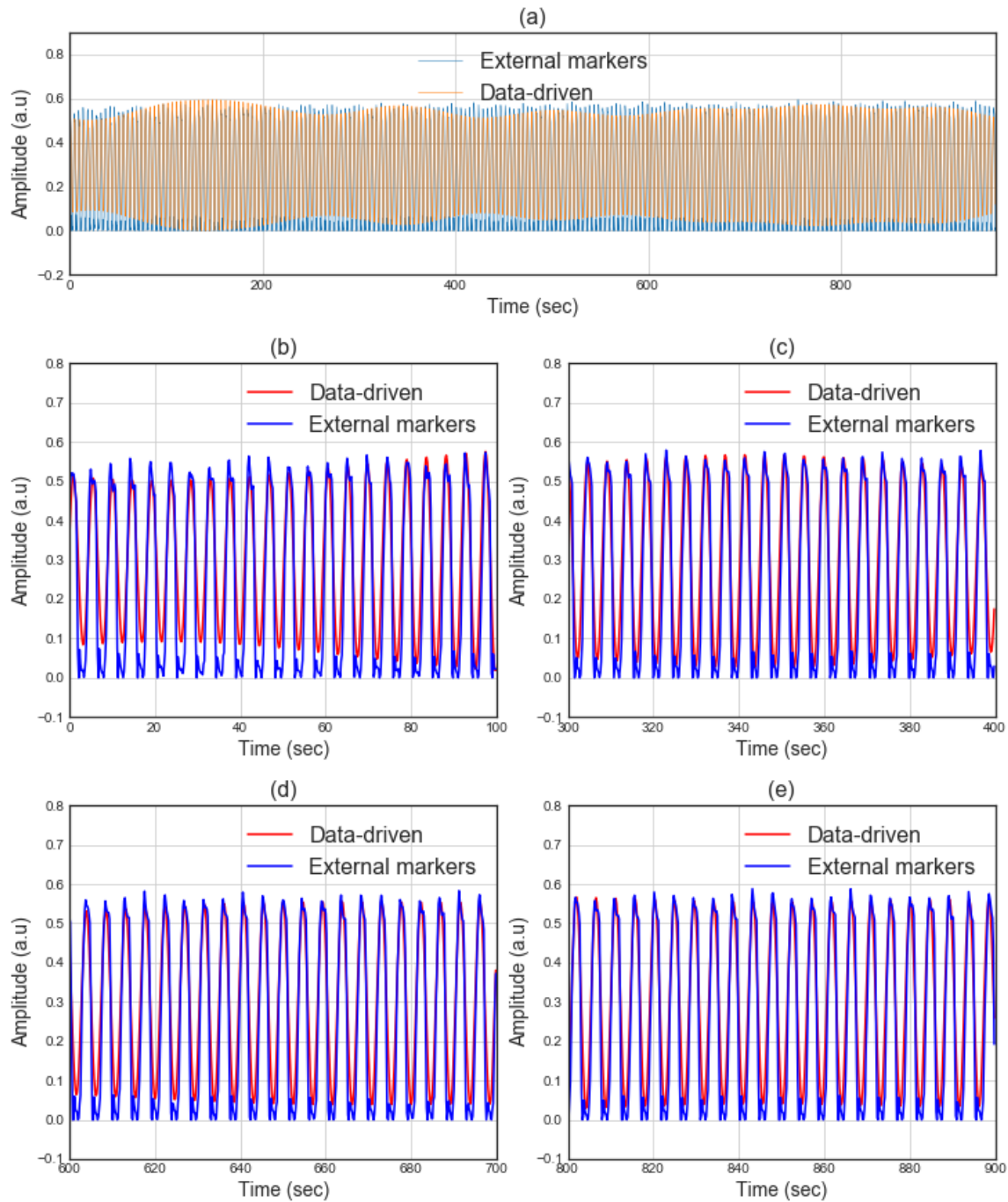
Figure 4.2: Data-driven respiratory signal overlaid with external respiratory signal for experiment 6001, for different time intervals. (a) Whole acquisition time (b) between 0 to 100 seconds (c) between 300 to 400 seconds (d) between 600 to 700 seconds (e) between 800 to 900 seconds.
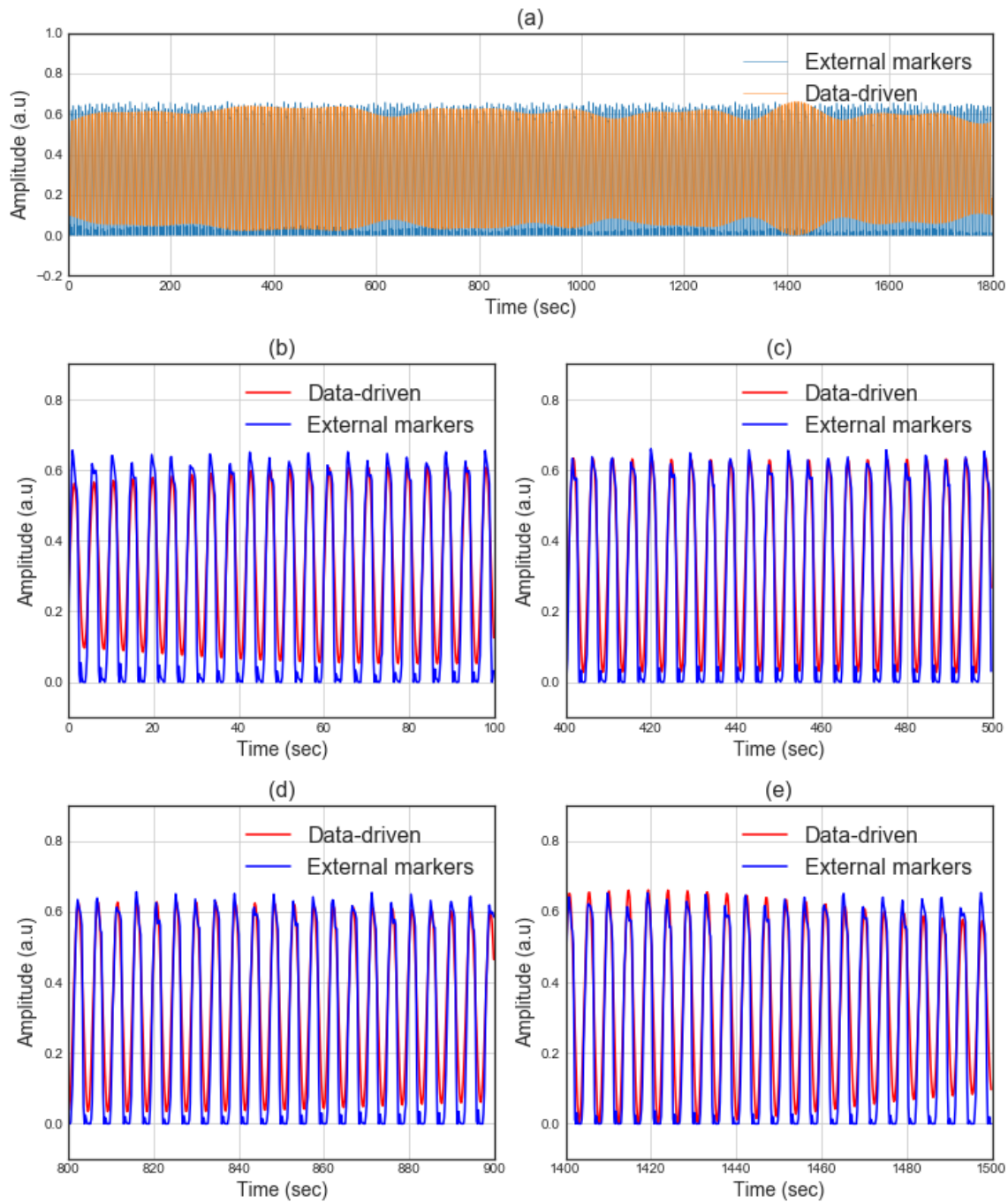
Figure 4.3: Data-driven respiratory signal overlaid with external respiratory signal for experiment 7001, for different time intervals. (a) Whole acquisition time (b) between 0 to 100 seconds (c) between 400 to 500 seconds (d) between 800 to 900 seconds (e) between 1400 to 1500 seconds.
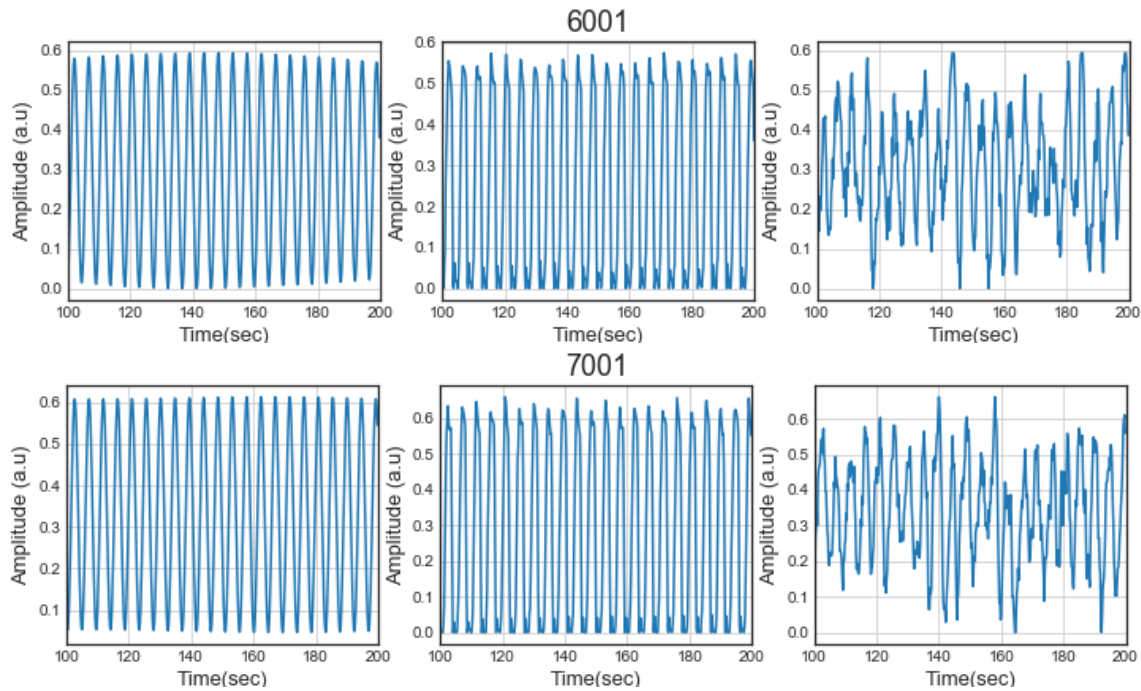
Figure 4.4: Respiratory signals used for gating in experiment 6001 (**top**) and 7001 (**bottom**). From left to right: Frequency filtered data-driven signal, External respiratory signal, Moving average filtered data-driven signal.

4.1.2 Optimization of Respiratory Motion Detection

In order to optimize the respiratory signal extraction, ROIs with different size and different locations were chosen. The SNR vs CNR and SNR vs volume of ROIs located at the diaphragm are shown in Figure 4.5. The same plots, but in this case for ROIs located at the heart, are shown in Figure 4.6.

The examination of the figures-of-merit obtained from the diaphragm, as shown in Figure 4.5, reveals an increase in SNR when increasing the volume of the selected ROI for experiment 7001. However in experiment 6001, we do not see this behavior. The regression lines drawn for SNR vs CNR shows a direct or inverse correlation for experiment 7001, yet the experiment 6001 doesn't shows a linear dependence between the SNR vs CNR.

For the ROIs located at the heart (Figure 4.6), the SNR increases with volume for both experiments. Further, the SNR vs CNR plots show clear correlations for experiment 7001, while these figures-of-merit show weakly dependencies in experiment 6001.
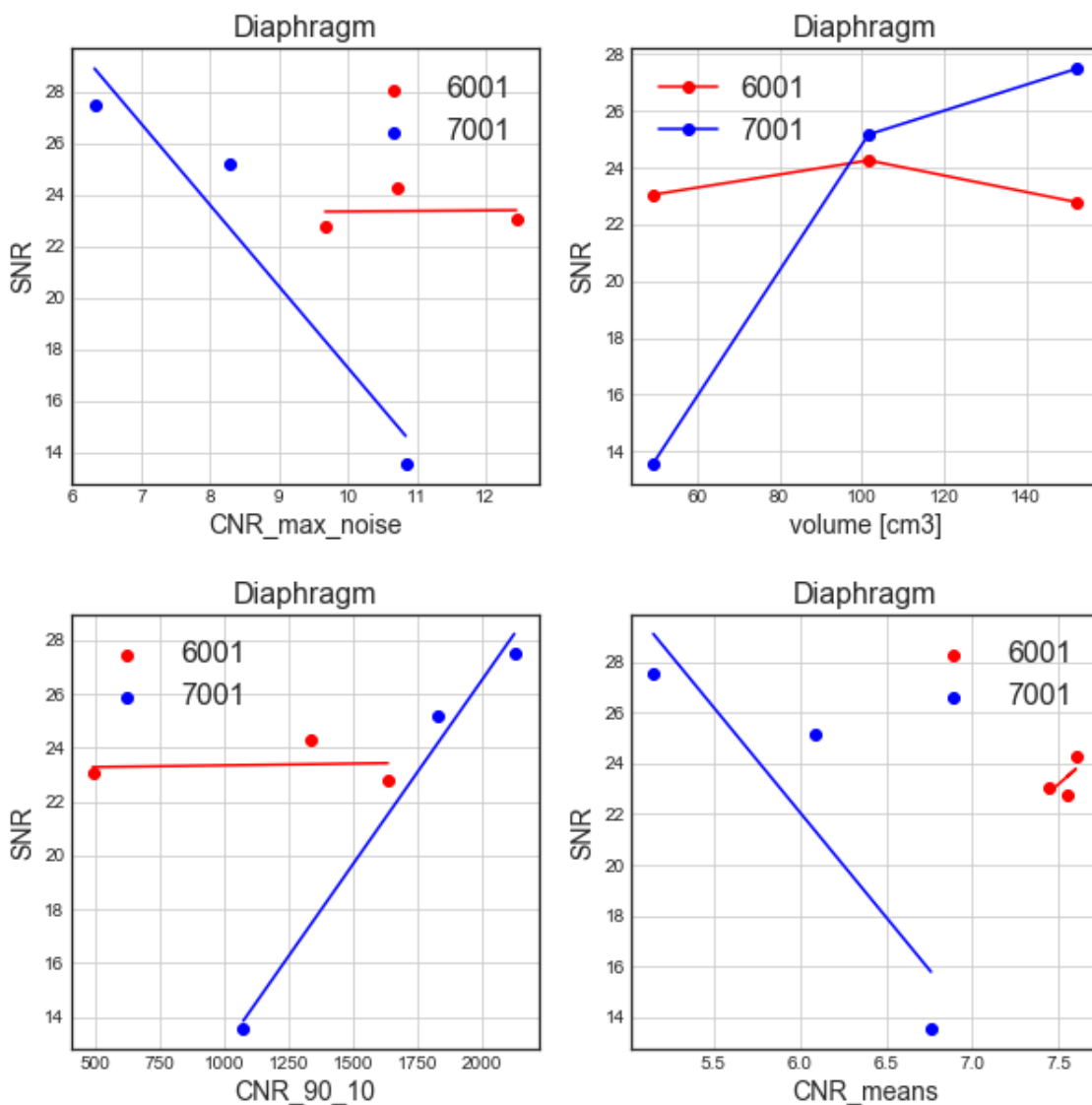
Figure 4.5: The correlation between SNR vs volume and SNR vs CNR using three different criteria shown for diaphragm regions for both phantom experiments.
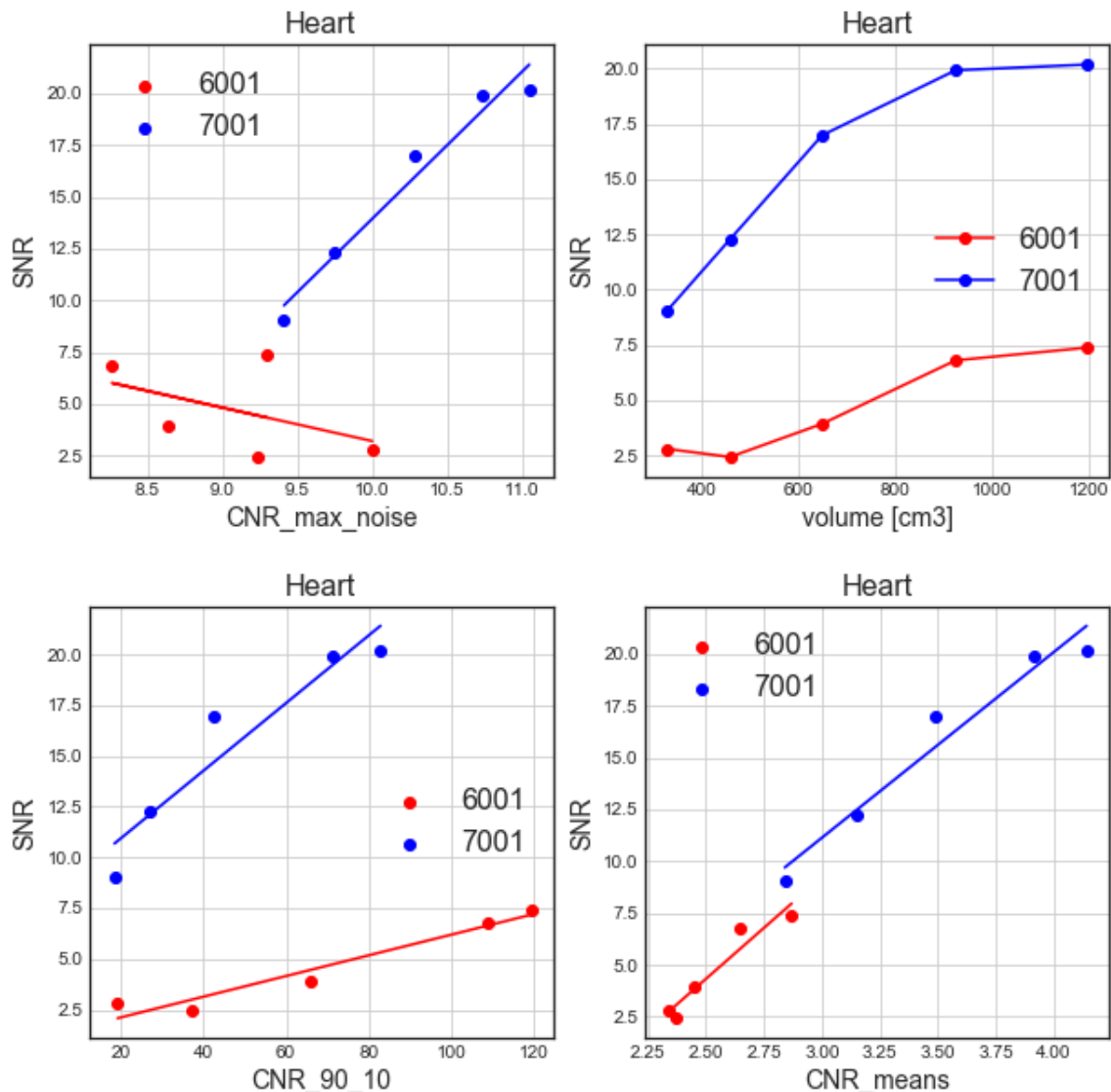
Figure 4.6: The correlation between SNR and CNR for 3 different criteria are presented here, also the SNR vs volume is added to the plot.

4.1.3 Data-driven Gating

Respiratory gating is performed for each experiment, using the external markers as well as the data-driven respiratory signals (frequency and moving average filters were used in the data-driven method). The data is divided into four gates from end-exhalation to end-inhalation. The amount of displacement of the lesion between different gates is taken as a measure of the tracking of the respiratory motion.

The gating images, obtained by using the external signal and the data-driven signals, are shown in Figures 4.7 and 4.8 for experiment 6001 and 7001, respectively. Clear respiratory motion effects can be seen in the gated images for both experiments.

For experiment 6001, the amount of respiratory motion between gate 1 and gate 4 is 10 mm, 10 mm and 9 mm for External method, data-driven with moving average filter (DD-MA) and data-driven with frequency filter (DD-Freq), respectively (Table 4.1 (top)).

The table shows a similar behavior between three signals to track the respiratory motion.

In regards to experiment 7001, gating of the data using three different respiratory signals provides a displacement of 10 mm between gate 1 and gate 4 for three methods (Table 4.1 (bottom)), showing a similar outcome regarding the myocardium displacement.
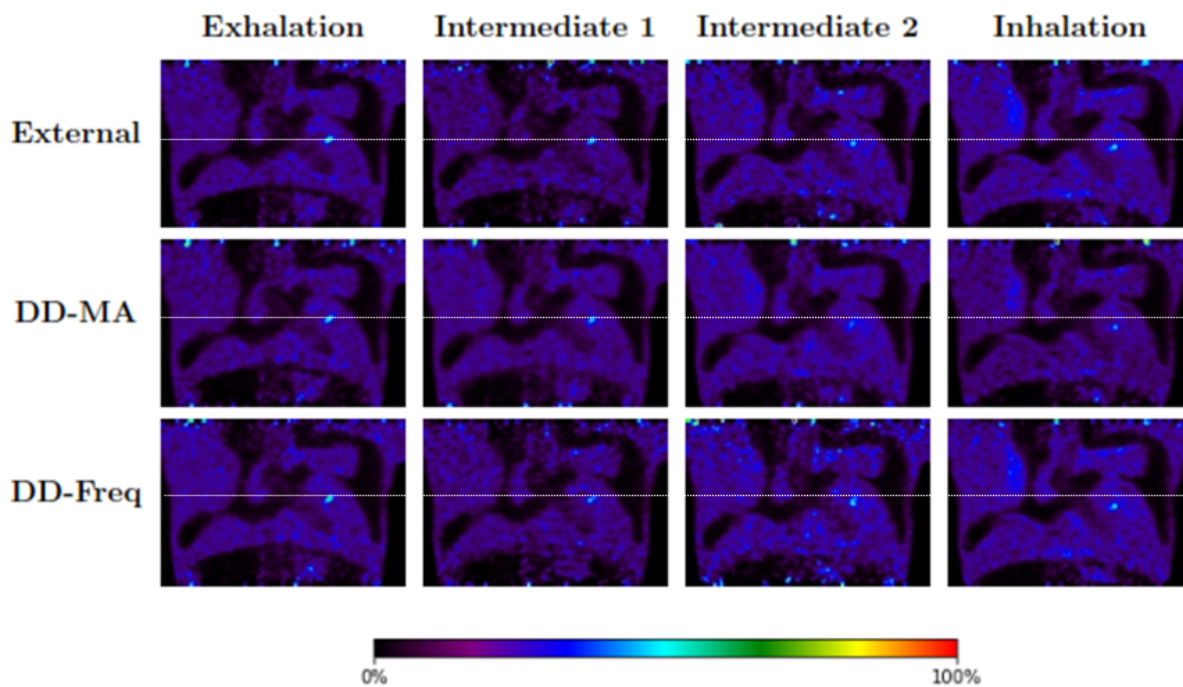
Figure 4.7: Reconstructed gates for external respiratory signal and Data-driven methods using moving average filtering (DD-MA) and frequency filtering (DD-Freq) for experiment 6001.
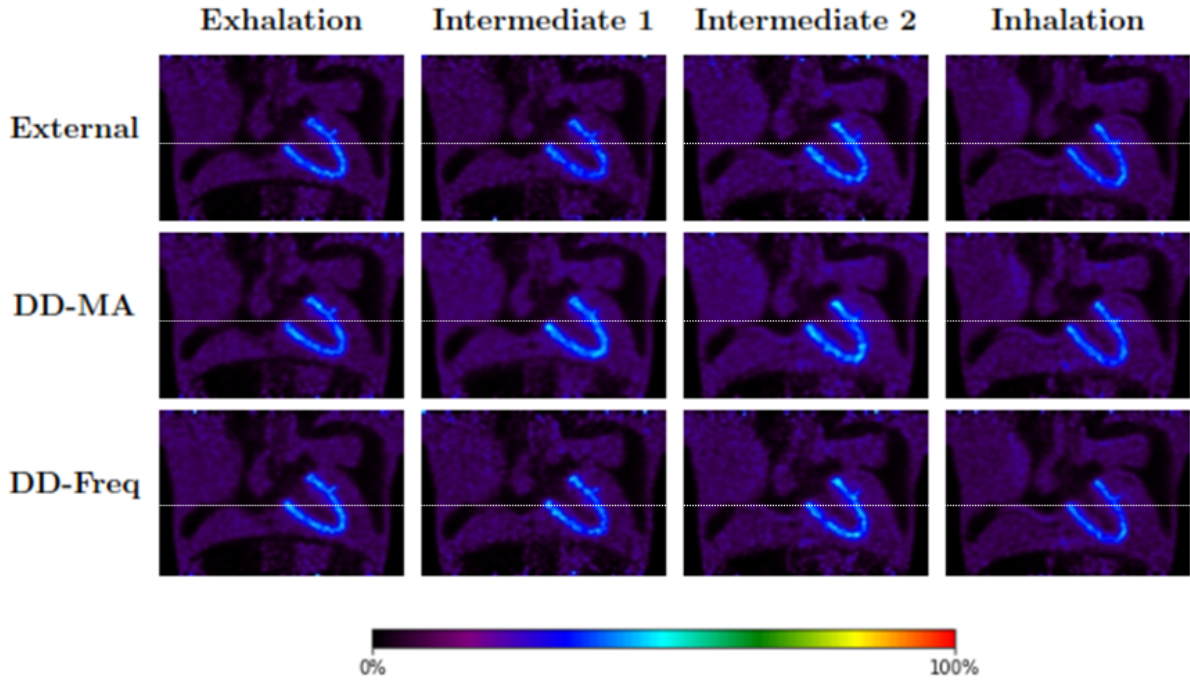
Figure 4.8: Reconstructed gated images for the external and the Data-driven respiratory signals for experiment 7001.

6001	External	DD-MA	DD-Freq
Exhalation (mm)	0.00	0.00	0.00
Intermediate 1 (mm)	1.01	1.01	1.01
Intermediate 2 (mm)	5.06	6.08	7.09
Inhalation (mm)	10.1	10.1	9.1
Maximum displacement (mm)	16.0	16.0	16.0

7001	External	DD-MA	DD-Freq
Exhalation (mm)	0.00	0.00	0.00
Intermediate 1 (mm)	2.03	2.03	2.03
Intermediate 2 (mm)	5.06	6.08	6.08
Inhalation (mm)	10.1	10.1	10.1
Maximum displacement (mm)	18.2	17.2	17.2

Table 4.1: Respiratory axial motion (mm) of the lesion between the different gates with reference to exhalation phase for experiments 6001 (top) and 7001 (bottom). The maximum displacement is captured in diaphragm region (bottom row).

The line profiles, through one of the spherical lesions (experiment 6001) and through the myocardium (experiment 7001), are shown in Figures 4.9 and 4.10. Gate 1 and gate 4 of each of the three methods are shown in the bottom subplots as a comparison. The activities are normalized for a better visualization of the motion effect in between first and last gates.
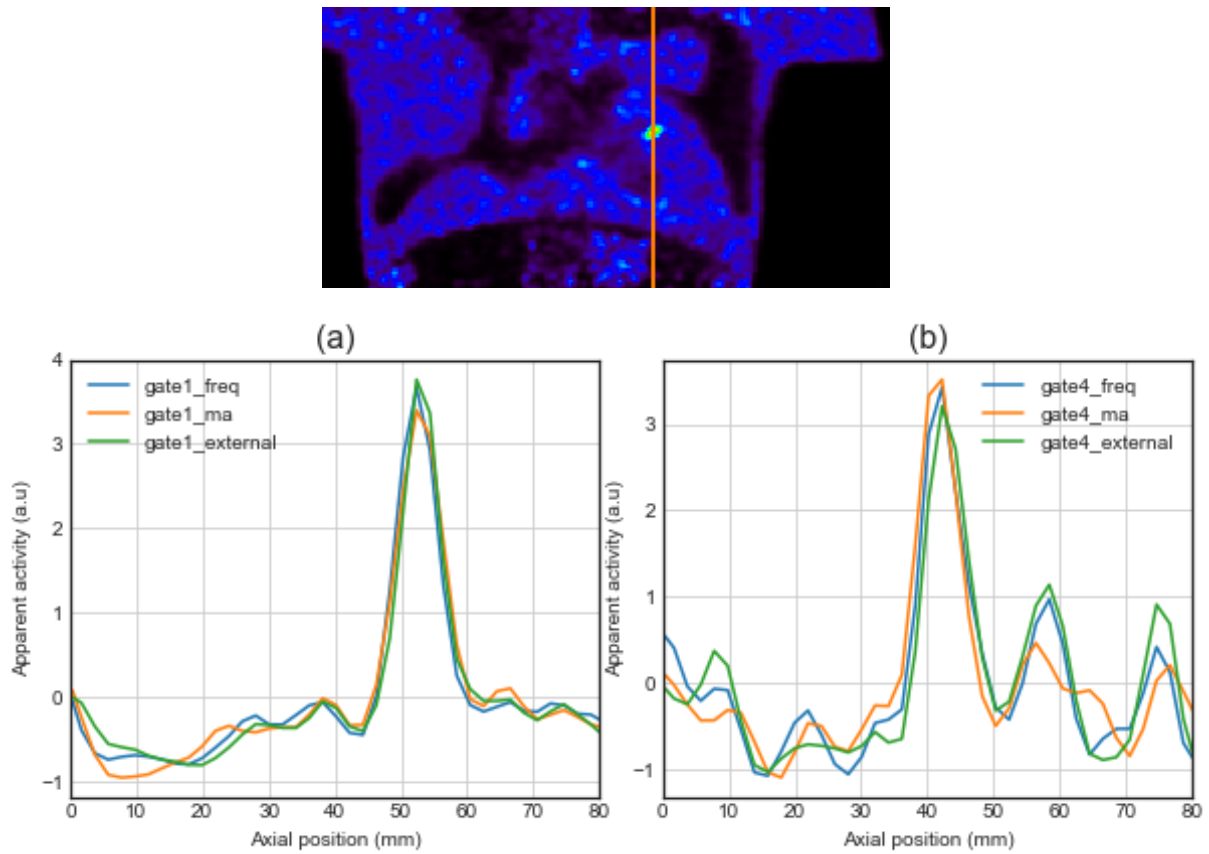
Figure 4.9: Vertical line profiles through the lesion (top), for experiment 6001. A visual comparison of the gate 1 and gate 4 for each of the three respiratory signals (bottom).
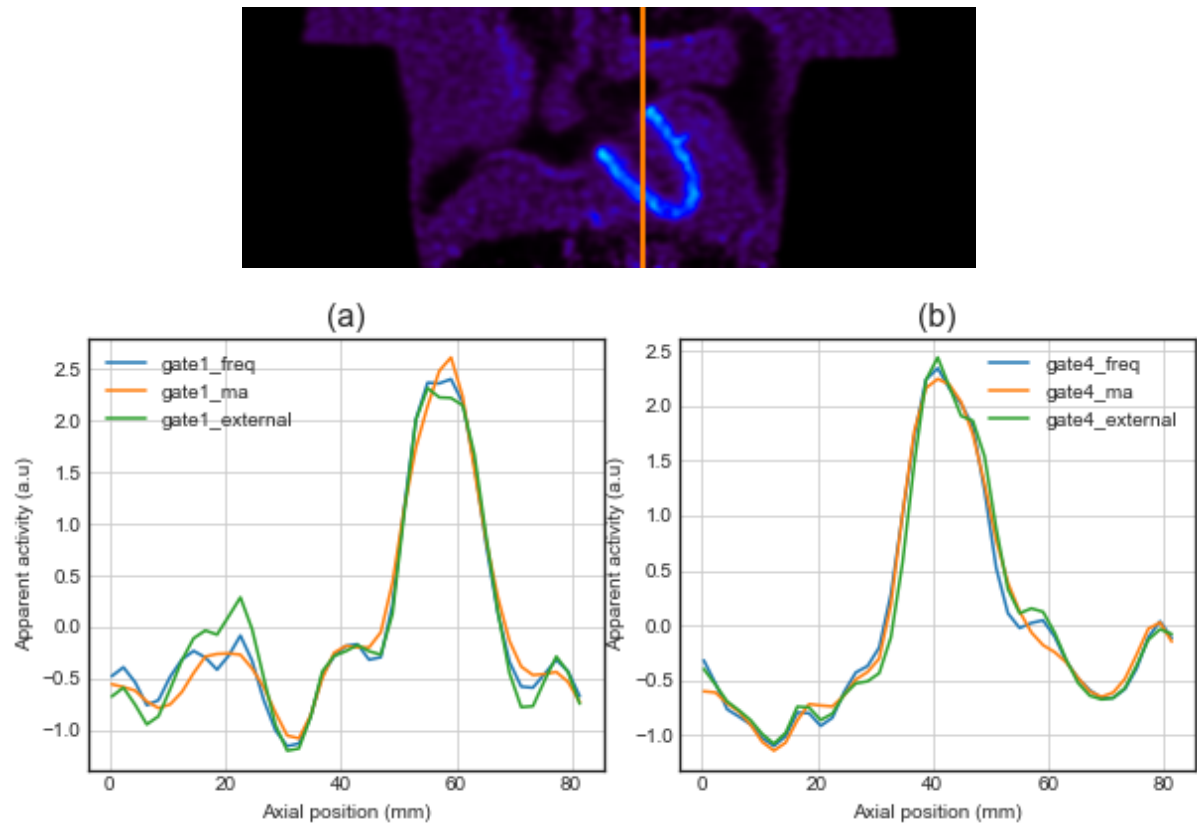
Figure 4.10: A vertical line through the myocardium, used as the line profile (top), for experiment 7001. Visual comparison of gate 1 and gate 4 to capture the displacement (bottom).

4.1.4   Respiratory Motion Compensation

The RTA-MoCo, Static and the reference-gate for both experiments are presented in Figure 4.11. Table 4.2 shows the LBR_{max}, the LBR_{50} and the noise values for all the reconstructed images. As shown in the table, LBR_{max} and LBR_{50} are improved when using motion-limiting techniques (Gated and RTA-MoCo images). However, noise increases significantly in the Gated images, while the noise measured in the RTA-MoCo and Static images is very similar.
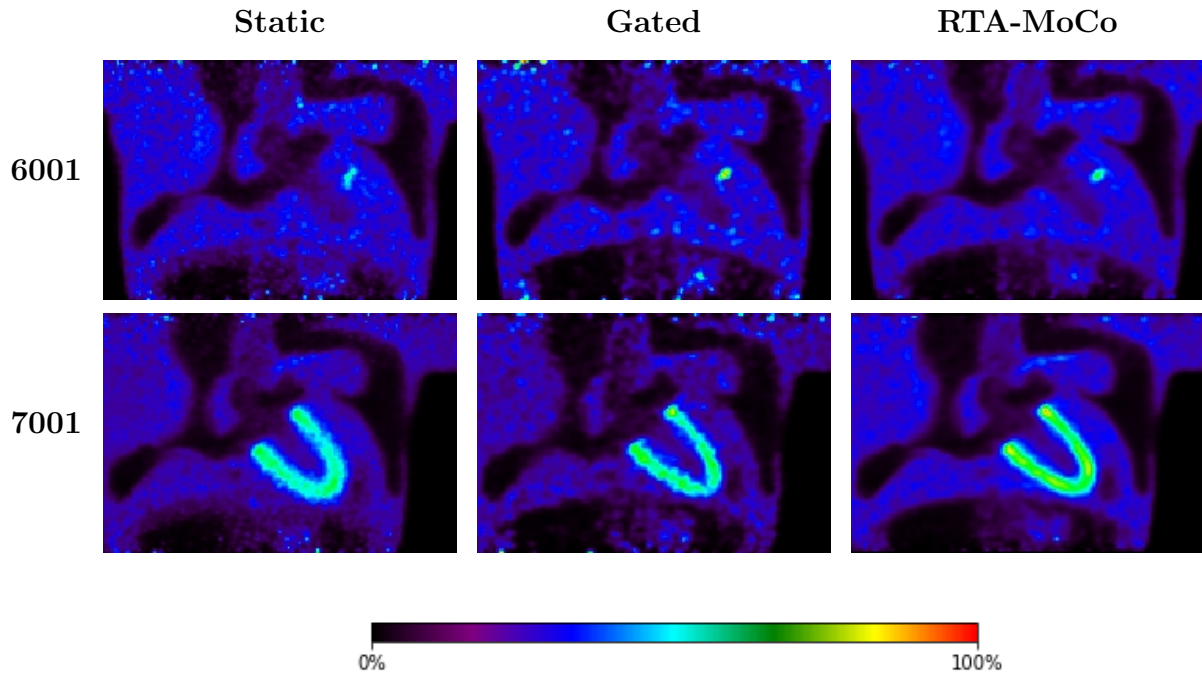
Figure 4.11: Coronal views of the reconstructed phantom experiments 6001 (top) and 7001 (bottom). From left to right: Static image without any motion-limiting technique, Gated image (end-expiratory gate) and RTA-MoCo image.

6001	LBR_{max}	LBR_{50}	Noise (%)
RTA-MoCo	3.72	2.35	9.00
Gated	5.32	3.41	16.0
Static	2.80	1.57	13.0

7001	LBR_{max}	LBR_{50}	Noise (%)
RTA-MoCo	5.89	3.90	8.00
Gated	7.87	4.54	15.0
Static	5.61	3.55	11.0

Table 4.2: Evaluation of LBRs and the noise percentage for both phantom experiments, done for RTA-MoCo image, static image and the reference gate.

Looking at the RTA-MoCo images compared to the static images and also examining the line profiles for MoCo, static and reference gates in Figure 4.12, makes it clear that the MoCo images show more localized lesions compared to the static images and less noise compared to the gated images.
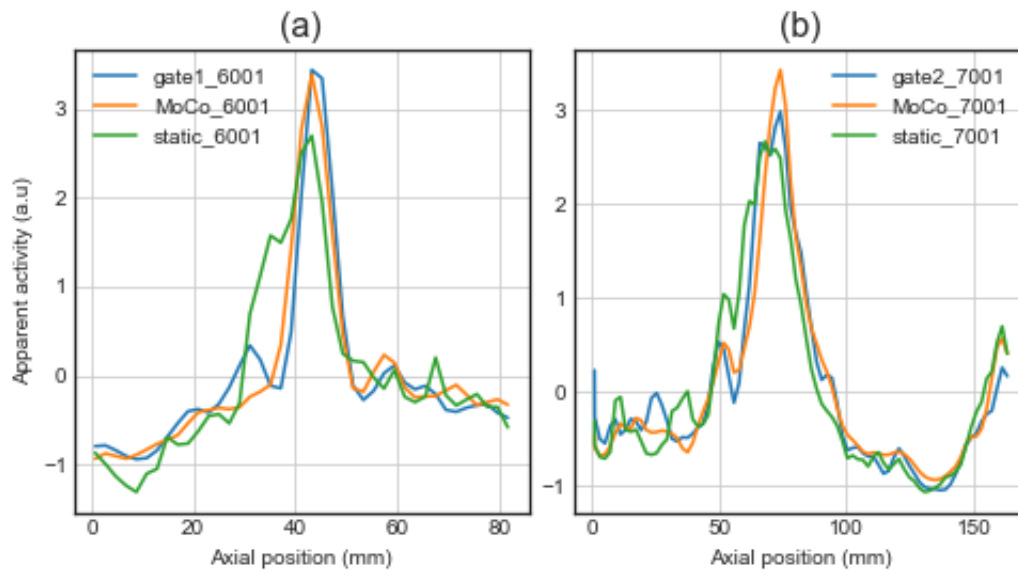
Figure 4.12: Line profiles through the myocardium for experiment 7001 and through the lesion in experiment 6001, for static, RTA-MoCo and the reference gate image. The static line profiles are broader around the peak.

4.2 Patient Data Results

This section contains the results obtained for the evaluated patient data. Several ROIs, located at different places, were specified for each patient to find an optimized respiratory signal extraction. In the patient cases where an acceptable respiratory signal was achieved (SNR higher than 4.0), an amplitude-based gating was also performed and evaluated. The respiratory motion of the patient for these cases was obtained by measuring the displacement between gates. Finally, the evaluation of the impact of a RTA-MoCo technique in the quantitative accuracy of the reconstructed images was performed for three representative cases.

4.2.1 Optimization of Respiratory Motion Detection

Figure 4.13 shows the correlation between the SNR and the ROI-volume correlation for ROIs located at the diaphragm, at the heart and centered at the lung lesion. The correlation between the SNR and three different CNR criteria is shown in Figure 4.14. The linear regression lines depicted in the figure show a very weak dependence between SNR and $CNR_{max-noise}$. Better correlations are seen for the $CNR_{90_{10}}$ and CNR_{means}, especially for the ROIs located at the diaphragm and at the heart.

In 5 of the cases, the data-driven was able to detect the motion with SNR $\geq$ 4 in the heart region and this predefined limit of SNR was achieved in 4 patient-data for the lesion and in 3 of them in diaphragm. In total, in 8 of 12 analyzed patients we were able to extract a respiratory signal with SNR higher than 4. Figure 4.15 shows several representative cases where respiratory motion was successfully extracted with the data-driven method and other representative cases where no clear motion was seen in the

specified ROI. The left image in the bottom row shows a myocardium with low uptake, which may hinder the motion detection. The middle image in the bottom row shows the lesion attached to the non-moving tissue, like mediastinum in this case. Finally, the image on the right-bottom shows a large high-grade tumor, which is most likely not moving.
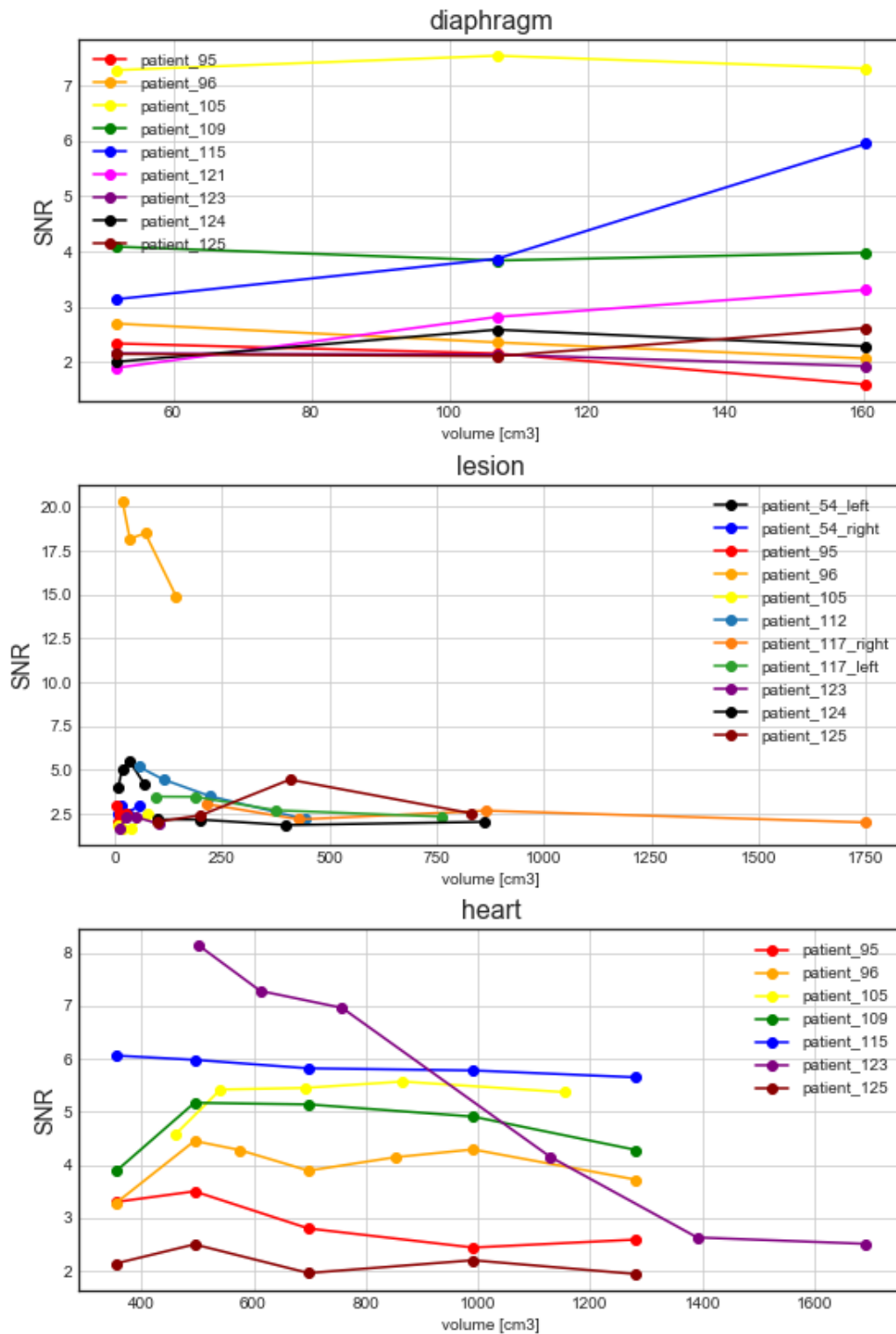
Figure 4.13: The correlation between SNR and different volumes used in each case.
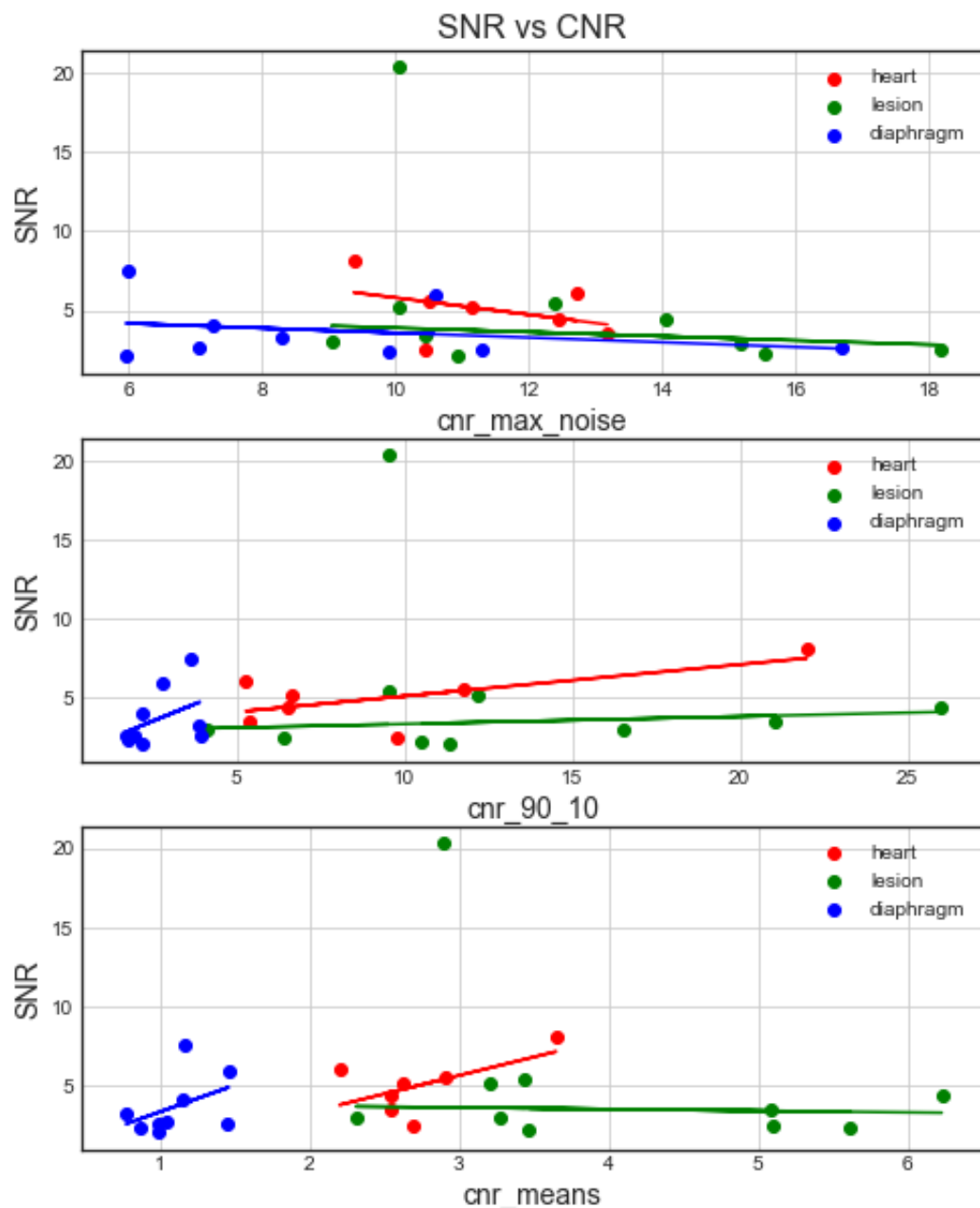
Figure 4.14: SNR vs CNR, using 3 different criteria. The linear regressions are added for ease of detecting the correlations between the SNR and CNR.

PT 96 **PT 115** **PT 123**

PT 95 **PT 117** **PT 117**
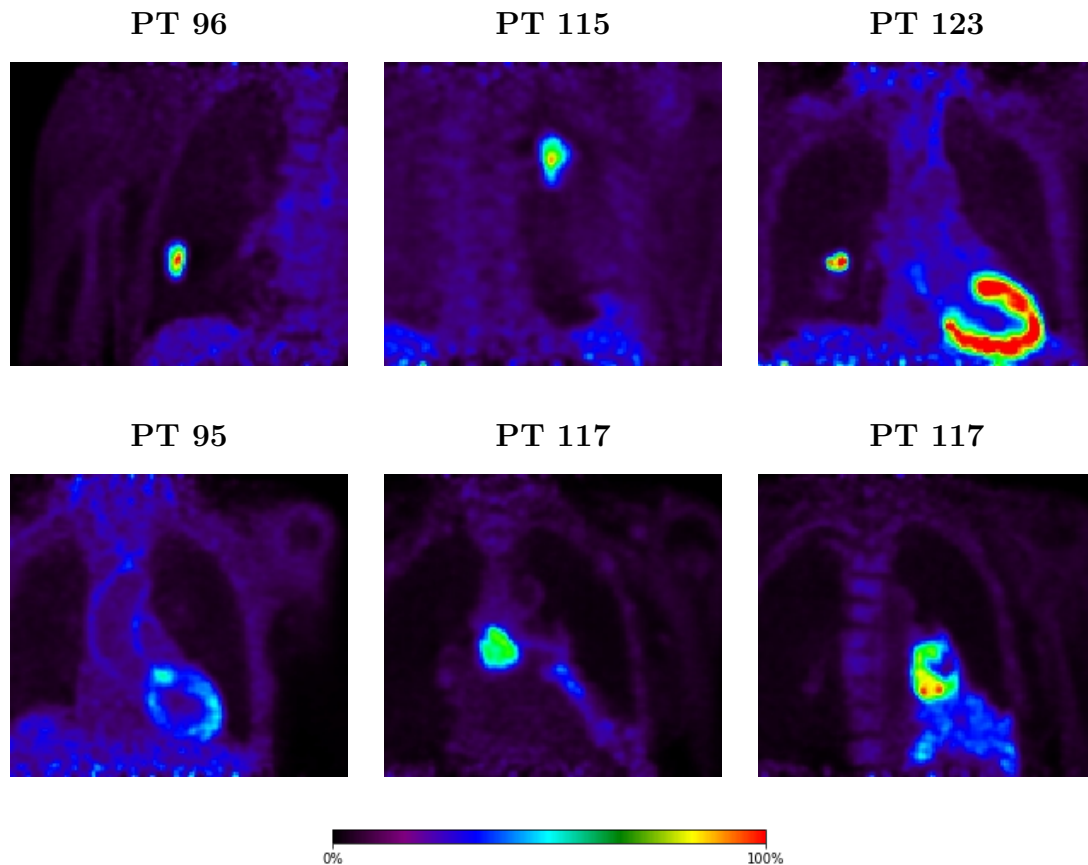
Figure 4.15: **Top**: Cases in which an acceptable respiratory signal was achieved. From left to right: small concentrated lesion with a considerable amount of observed motion, lesion in the moving part of the thorax, myocardium with suitable amount of uptake. **Bottom**: Cases in which the extraction of the respiratory signal was not possible. From left to right: lack of heart uptake, lesion attached to mediastinum, big tumor lesion of a patient with high-grade advanced cancer, which is most likely not breathing properly.

4.2.2   Data-driven Gating

Figure 4.16 shows the gated images corresponding to patient #96, in which the respiratory translation of the tumor lesion is clear. Alternatively, figure 4.17 shows the gate 1 and gate 4 (exhalation and inhalation) for the same patient. The gates are reconstructed using the respiratory signal obtained from the heart and from the lesion lesion. The SNR of the respiratory signal obtained from the heart (SNR $\approx$ 4), results in an inadequate resolution of the motion, while the SNR of the signal obtained from the lesion (SNR $\approx$ 20) resulted in a considerable improvement in the motion tracking of the lesion.
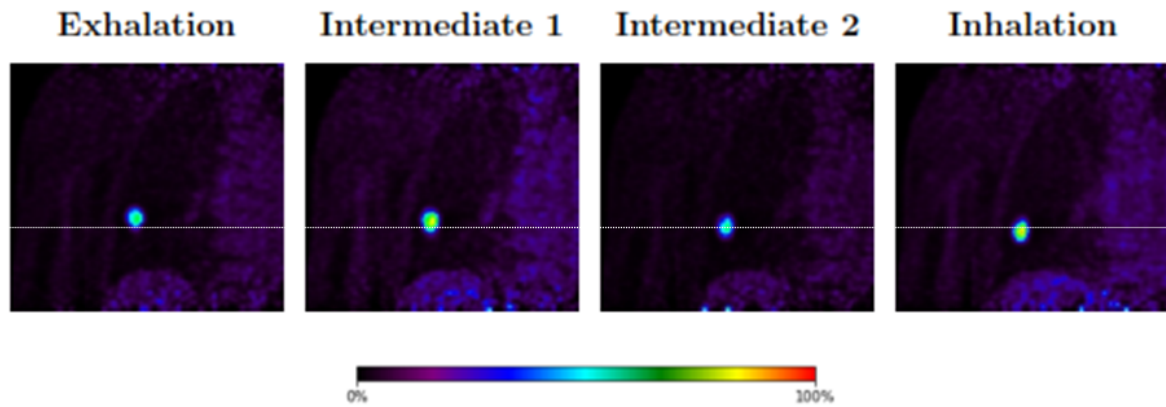
Figure 4.16: A sequence of 4 gates, showing the respiratory movement of the lesion for patient # 96.
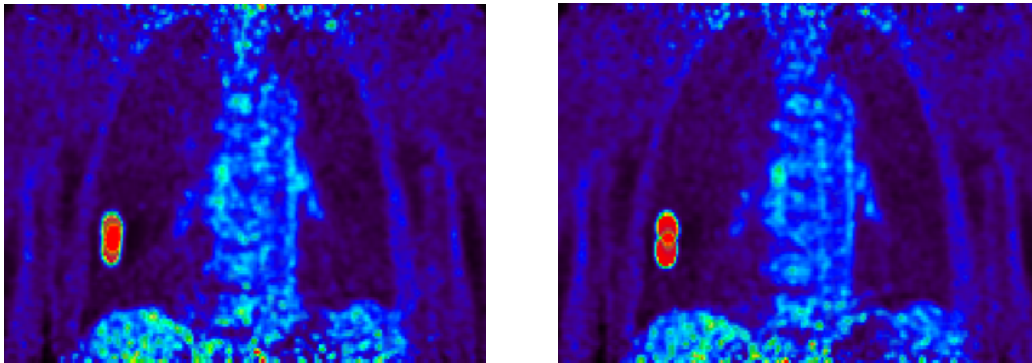
Figure 4.17: Figure shows gate 1 and gate 4 overlaid on each other for patient # 96. Left: gate 1 and gate 4 reconstructed using the respiratory signal captured for the heart region. Right: respiratory signal captured in the lesion for the same patient-data, which shows a superior performance in capturing the motion.

The estimated motion extracted by the data-driven method is measured between gate 1 and gate 4 in all the cases with SNR $\geq$ 4. The correlation between SNR and estimated motion is depicted in Figure 4.18, as a linear regression with coefficient of correlation $r^2 = 0.704$.
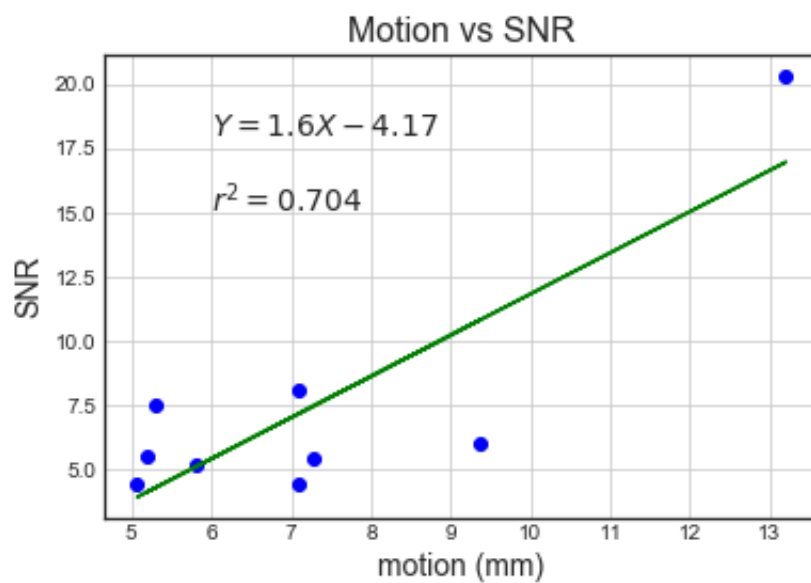
Figure 4.18: The relationship between the captured motion in data-driven gating and corresponding SNR. The regression equation and the coefficient of determination are also added to the figure.

4.2.3   Respiratory Motion Compensation

The impact of motion-limiting techniques (gating and RTA-MoCo) was evaluated in three representative cases that showed a good extraction of the respiratory signal. Figure 4.19 shows the reconstructed RTA-MoCo image, together with the standard Static image without any motion-limiting approach and the gated image at the end-expiratory phase. The motion blurring effect is reduced in the gated images, at an expense of increased noise levels. In the RTA-MoCo images, the blurring effect due to motion is also reduced, while preserving the noise properties of the static images.
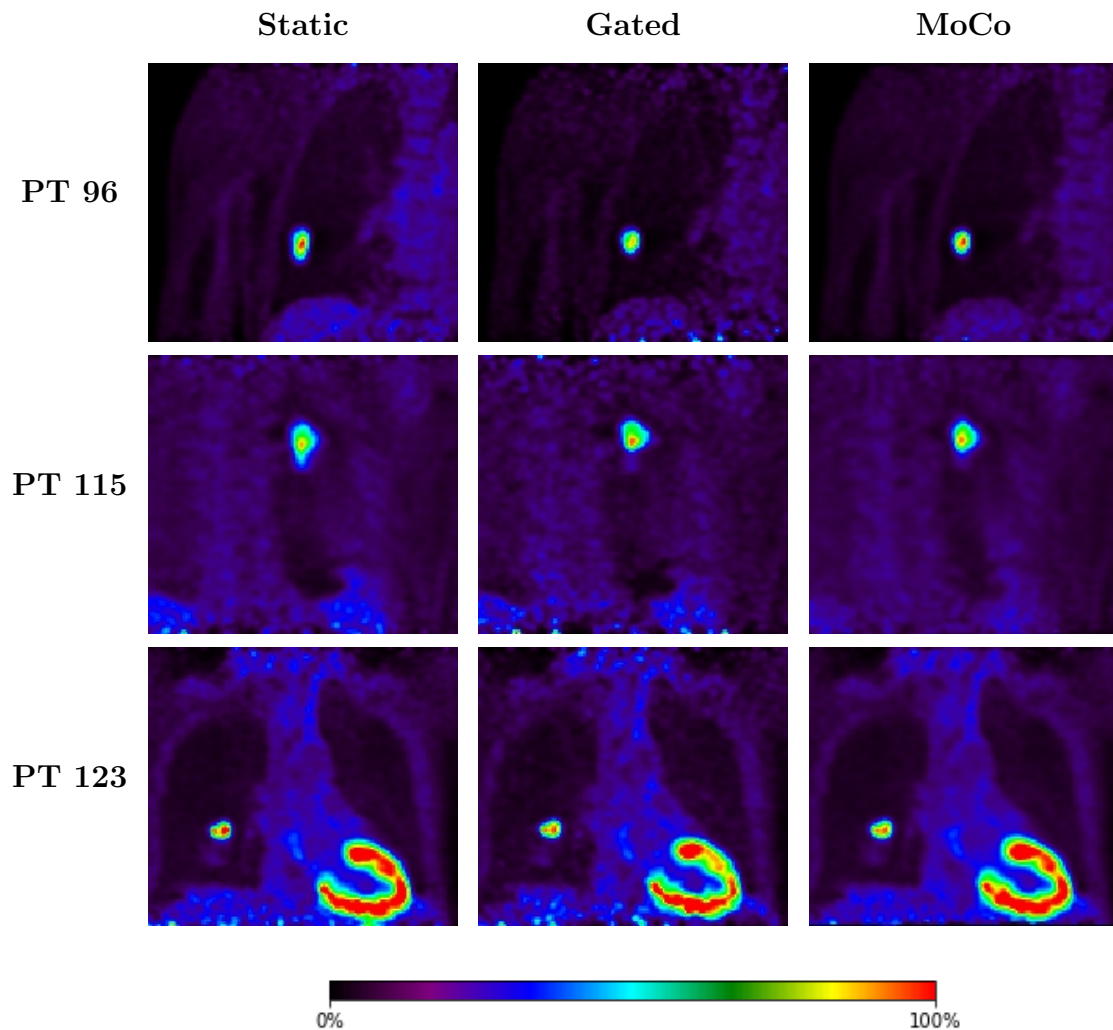
Figure 4.19: Visual comparison of the static image, reference gate used for motion compensation and the MoCo image. The elongation of the static image compared to MoCo image is quite visible in 2 of the cases.

The measured lesion-to-background ratios (LBR_{50} and LBR_{max}) and noise values given in Table 4.3 confirm that the RTA-MoCo images have higher LBR and lower noise than the static images.

PT 96	LBR_{max}	LBR_{50}	Noise (%)
RTA-MoCo	12.6	8.69	17.0
Gated	12.2	8.45	23.0
Static	10.2	6.91	18.0

PT 115	LBR_{max}	LBR_{50}	Noise (%)
RTA-MoCo	9.60	6.39	11.0
Gated	10.0	6.62	19.0
Static	9.11	5.95	13.0

PT 123	LBR_{max}	LBR_{50}	Noise (%)
RTA-MoCo	9.29	6.38	18.0
Gated	9.38	6.54	23.0
Static	10.9	7.30	20.0

Table 4.3: Evaluations of lesion to background (LBR) ratio and the noise percentage for 3 patient data.

The line profiles of the same three cases are depicted in Figure 4.20, which shows broader width around the peak for case 96 and 115, and the same width around the line profile of case 123 for MoCo, static and reference gate can be indicative of the lack of movement in the lesion, looking at the Figure 4.13 confirms this idea, since the data-driven method extracts a very weak signal corresponding to the respiratory movement.
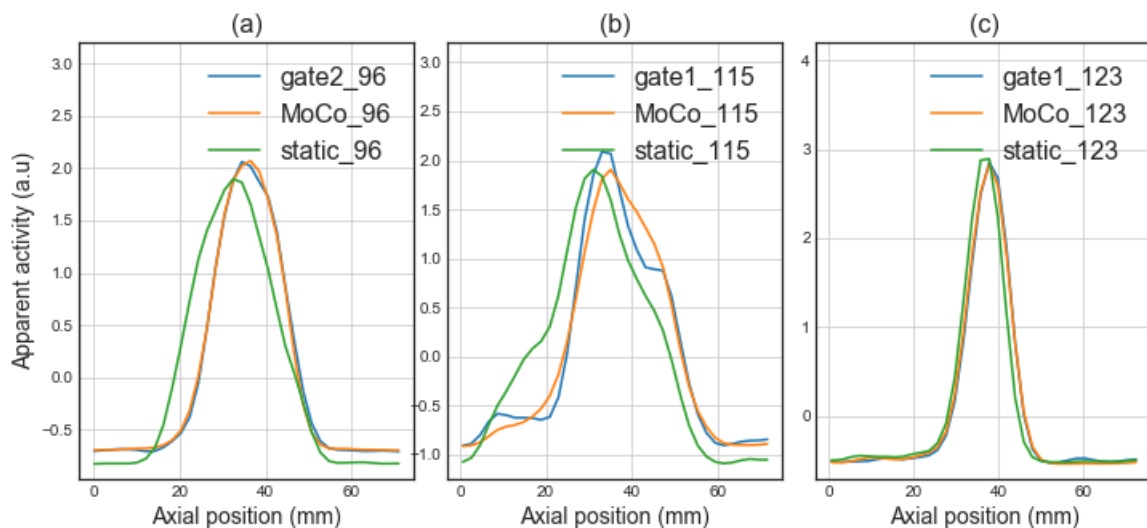
Figure 4.20: Line profiles of the static, reference gate and the motion compensated images for 3 patient data.

Chapter 5

Discussion

5.1 Phantom Data Discussion

The aim of using the phantom data was to validate the method of list-mode driven respiratory gating in PET imaging by comparing the respiratory signals extracted from the external markers with the data-driven signals and in the next step evaluation of the gating images for each case.

In both phantom experiments, the frequency spectrum of the data-driven signal shows an exact correspondence to the external signal obtained from the respiratory belt, with a strong frequency peak at $f_{resp} = 0.21$ Hz. The higher amount of noise of the data-driven signal, which is due to the Poisson nature of PET data (Figure 4.1), provide lower SNR ratio values in the data-driven signals (33.18 and 47.8 in experiments 6001 and 7001 respectively, while the external signal provide SNR values of 2069 and 3549 for experiments 6001 and 7001, respectively).

The highest amount of axial displacement of the thorax is taken as a performance criteria of the gating approaches. A rough estimate of the axial positions using the mean lesion (experiment 6001) and myocardial (experiment 7001) displacements between the gates are shown in Table 4.1. The highest axial motions of the heart in experiment 6001 are 10 mm, 10 mm and 9 mm for external, moving average filtered and frequency filtered methods respectively. While similar maximum displacements of 10 mm are observed in the myocardium in experiment 7001. As mentioned before, the thorax phantom respiratory displacement was set at 20 mm in the diaphragm. The highest amount of motion for experiment 6001 for data-driven and external methods are captured in diaphragm area and amounts to 16 mm both which indicates a successful motion detection for this case. On other hand, the maximum displacement measured in the diaphragm for experiment 7001 was 18 mm and 17 mm, for external and data-driven signals, respectively. The measured displacements are close to the real diaphragm displacement (20 mm). The small motion underestimations of about 20%, measured from the gated images, are due to the relatively low number of gates used in the gating approaches (only 4). We expect that if larger number of gates is used, we will be able to recover the 20 mm axial displacement in the gated images, but at the expense of increasing the noise levels.

Of note, the fact that the two data-driven respiratory signals (frequency filtered and MA filtered) provide very similar gated images, even when their visual aspect is quite

different (see Figures 4.9 and 4.10), suggest that the implemented amplitude-based respiratory binning is quite robust. However, further studies with higher number of gates and in patients or phantom with irregular motion patterns should be performed in order to proof this assumption.

5.2   Patient Data Discussion

The validated data-driven method is applied to the real patient-data in order to optimize the extracted respiratory signals. In this sense 12 patient-data were evaluated to search an optimized extraction of the respiratory signal. The method showed no meaningful correlation between SNR and CNR or SNR and volume of the selected ROI, but the choice of the ROIs and different volume sizes showed to have great impact on the motion and in some cases the change of the volume size could increase or decrease the SNR by 4 times and the same applies to the choice of the ROI from myocardium to lesion to diaphragm. For all the 12 cases studied, the motion was successfully extracted in 8 of them. In 5 cases the myocardium provided acceptable SNR ≥ 4 in the extracted respiratory signal, while the ROI centered at the lesion worked well in 4 cases and the ROI located at the diaphragm worked well in 3 cases.

Several reasons can be attributed to the cases in which no extraction of respiratory motion was achieved, as shown in Figure 4.15 in section 4.2.1. These can be: (1) The lack of a proper contrast in the chosen ROI to extract the respiratory signal. (2) The attachment of the lesion of interest to a non-moving tissue such as mediastinum. In this case, even if the motion is properly extracted from another ROI (heart or diaphragm), the practical impact of the motion-limiting approach will not be relevant as the lesion is not moving. (3) In other cases, patients with high-grade and advanced lung cancer, with large and heterogeneous tumor lesions, are usually be indicative of lack of respiratory motion, due to the patient condition and higher inability to breath properly.

The cases in which a relatively good extraction of the respiratory motion was achieved were selected for further analysis of the gated image reconstruction. In these cases, we observed a linear correlation between the SNR of the respiratory signal and the maximum axial displacement observed in the gated images (correlation coefficient $r^2 = 0.704$). This indicates, as expected, that the ability to extract and track respiratory motion in PET thoracic imaging is directly related with the SNR of the extracted respiratory signal. This is of special importance when aiming to track the tumor lesion motion for radiotherapy planning applications, where an optimal extraction of the respiratory signal is desired.

As shown in Table 4.3, the RTA-MoCo images present lower level of noise than the static and the gated images. In addition, the LBR values show an overall improvement in the motion-limited images (gated and RTA-MoCo) over the static images. This is further demonstrated by the line profiles shown in Figure 4.20, where two of the patients show a more localized lesion in the motion-limited images. In the other case (patient # 123), the similar width of the line profile in all the reconstructed images can be indicative of the lack of movement of the lesion (the captured lesion SNR in this case (≈ 2) also suggests the tumor to be non-moving).

5.3   Limitations of the study and future work

The main limitation of the phantom experiments performed in this work is the lack of a validation of the data-driven gating using experiments with irregular motion patterns. In the two experiments performed in this work, the mechanical motion of the phantom was very regular, showing always a very similar amplitude and the same frequency. This is not representative of how a real patient breath, and therefore, further studies with more complex breathing patterns are needed to properly validate the data-driven motion detection technique.

Furthermore, and related to the patient studies evaluated in this thesis, the absence of a reference external signal to be compared with the data-driven gating, is recognized as another important limitation of the study. Further validations of the data-driven approach in patient datasets with external respiratory triggers available are needed. In that sense, new acquisitions of patients with lung cancer and external gating devices are being acquired and will be analyzed in future work. Furthermore, PET/MR studies that involve the use of MR navigators are also being acquired and will be processed in future work.

The performance of the data-driven method in the patient cases where the extraction of the respiratory signal was not possible is difficult to judge. This is due to the fact that, as we do not have any additional measurement of motion to serve as ground truth, we cannot know if there is really no motion to be detected or if the data-driven approach is not working properly. Furthermore, external gating devices may also fail in real patient acquisitions, due to irregularities in the patient breathing such as breath holds, changes in the respiratory frequency or nonlinear respiratory behavior (respiratory hysteresis). The proper comparison of the data-driven and external tracking approaches for respiratory motion detection is also future work.

Other limitations of this work are the small size of the analyzed patient cohort and the use of only four bins in the amplitude-based respiratory gating, which is known to possess a significant amount of intra-frame motion. Regarding the size of the patient cohort, as it was previously mentioned, several follow-up studies were already initiated. Regarding the number of gates used for the respiratory binning, we expect to see an improvement in the motion-limiting techniques when increasing the number of respiratory bins. However, the increase of noise in the gated reconstructions may also reduce the accuracy of the resulting MoCo images. Further studies are required to find the optimal settings of this technique.

Chapter 6

Conclusion

In this work we demonstrated that a data-driven respiratory signal extraction is feasible in phantom data, obtaining similar results to the ones obtained with external markers. In patient data, the data-driven respiratory extraction was successful in 8 of 12 analyzed cases.

The performance of the data-driven method was extremely dependent on the location of the ROI chosen for the extraction of the respiratory signal and on its size. Unfortunately, an automatic approach to find the optimal ROI location and size was not possible in this work.

Future work includes the evaluation of further patient datasets, with an external trigger or other motion surrogates available, to compare the data-driven motion detection approach with other methodologies.

Bibliography

Al-Nahhas, A, Z Win, T Szyszko, A Singh, C Nanni, S Fanti and D Rubello. 2007. 'Gallium-68 PET: a new frontier in receptor cancer imaging'. *Anticancer research* 27 (6B): 4087–4094.

Alessio, Adam, and Paul Kinahan. 2006. 'PET image reconstruction'. *Nuclear medicine* 1:1–22.

Bailey, Dale L, David W Townsend, Peter E Valk and Michael N Maisey. 2005. *Positron emission tomography.* Springer.

Beyer, Thomas, David W Townsend, Tony Brun, Paul E Kinahan et al. 2000. 'A combined PET/CT scanner for clinical oncology'. *The Journal of nuclear medicine* 41 (8): 1369.

Beyer, Thomas, Martin L Lassen, Ronald Boellaard, Gaspar Delso, Maqsood Yaqub, Bernhard Sattler and Harald H Quick. 2016. 'Investigating the state-of-the-art in whole-body MR-based attenuation correction: an intra-individual, inter-system, inventory study on three clinical PET/MR systems'. *Magnetic Resonance Materials in Physics, Biology and Medicine* 29 (1): 75–87.

Birkfellner, Wolfgang. 2015. *Applied medical image processing: a basic course.* CRC Press.

Bolwin, Konstantin, Björn Czekalla, Lynn J Frohwein, Florian Büther and Klaus P Schäfers. 2018. 'Anthropomorphic thorax phantom for cardio-respiratory motion simulation in tomographic imaging'. *Physics in Medicine & Biology* 63 (3): 035009.

Bracewell, Ronald Newbold, and ACf Riddle. 1967. 'Inversion of fan-beam scans in radio astronomy'. *The Astrophysical Journal* 150:427.

Brix, Gunnar, Ursula Lechel, Gerhard Glatting, Sibylle I Ziegler, Wolfgang Münzing, Stefan P Müller and Thomas Beyer. 2005. 'Radiation exposure of patients undergoing whole-body dual-modality 18F-FDG PET/CT examinations'. *Journal of Nuclear Medicine* 46 (4): 608–613.

Buerger, Christian, Charalampos Tsoumpas, Andrew Aitken, Andrew Peter King, Paul Schleyer, Volkmar Schulz, Paul K Marsden and Tobias Schaeffter. 2012. 'Investigation of MR-based attenuation correction and motion compensation for hybrid PET/MR'. *IEEE Transactions on Nuclear Science* 59 (5): 1967–1976.

Büther, Florian, Mohammad Dawood, Lars Stegger, Frank Wübbeling, Michael Schäfers, Otmar Schober and Klaus P Schäfers. 2009. 'List mode–driven cardiac and respiratory gating in pet'. *Journal of Nuclear Medicine* 50 (5): 674–681.

Byrne, Charles. 2001. 'Likelihood maximization for list-mode emission tomographic image reconstruction'. *IEEE Transactions on Medical Imaging* 20 (10): 1084–1092.

Cal-González, Jacobo, JL Herraiz, Samuel España, PMG Corzo, Juan José Vaquero, Manuel Desco and Jose Manuel Udias. 2013. 'Positron range estimations with PeneloPET'. *Physics in Medicine & Biology* 58 (15): 5127.

Carney, Jonathan PJ, David W Townsend, Vitaliy Rappoport and Bernard Bendriem. 2006. 'Method for transforming CT images for attenuation correction in PET/CT imaging'. *Medical physics* 33 (4): 976–983.

Casey, ME, and R Nutt. 1986. 'A multicrystal two dimensional BGO detector system for positron emission tomography'. *Ieee transactions on nuclear science* 33 (1): 460–463.

Cherry, Simon R, James A Sorenson and Michael E Phelps. 2012. *Physics in nuclear medicine e-Book.* Elsevier Health Sciences.

Ciernik, I Frank, Elena Dizendorf, Brigitta G Baumert, Beatrice Reiner, Cyrill Burger, J Bernard Davis, Urs M Lütolf, Hans C Steinert and Gustav K Von Schulthess. 2003. 'Radiation treatment planning with an integrated positron emission and computer tomography (PET/CT): a feasibility study'. *International Journal of Radiation Oncology Biology Physics* 57 (3): 853–863.

Conti, Maurizio. 2011. 'Focus on time-of-flight PET: the benefits of improved time resolution'. *European journal of nuclear medicine and molecular imaging* 38 (6): 1147–1157.

Cunningham, John Robert, and Harold E Johns. 1983. 'The physics of radiology'. *Springfield: Charles C. Thosmas.*

Dawood, Mohammad, Florian Büther, Norbert Lang, Otmar Schober and Klaus P Schäfers. 2007. 'Respiratory gating in positron emission tomography: a quantitative comparison of different gating schemes'. *Medical Physics* 34 (7): 3067–3076.

DeBenedetti, Sergio, CE Cowan, Wilfred R Konneker and Henry Primakoff. 1950. 'On the angular distribution of two-photon annihilation radiation'. *Physical Review* 77 (2): 205.

Delso, Gaspar, Sebastian Fürst, Björn Jakoby, Ralf Ladebeck, Carl Ganter, Stephan G Nekolla, Markus Schwaiger and Sibylle I Ziegler. 2011. 'Performance measurements of the Siemens mMR integrated whole-body PET/MR scanner'. *Journal of nuclear medicine* 52 (12): 1914–1922.

Dempster, Arthur P, Nan M Laird and Donald B Rubin. 1977. 'Maximum likelihood from incomplete data via the EM algorithm'. *Journal of the royal statistical society. Series B (methodological):* 1–38.

Fahey, Frederic H. 2002. 'Data acquisition in PET imaging'. *Journal of nuclear medicine technology* 30 (2): 39–49.

Fieseler, Michael, Harald Kugel, Fabian Gigengack, Thomas Kösters, Florian Büther, Harald H Quick, Cornelius Faber, Xiaoyi Jiang and Klaus P Schäfers. 2013. 'A dynamic thorax phantom for the assessment of cardiac and respiratory motion correction in PET/MRI: A preliminary evaluation'. *Nuclear Instruments and Methods in Physics Research Section A: Accelerators, Spectrometers, Detectors and Associated Equipment* 702:59–63.

Gigengack, Fabian, Xiaoyi Jiang, Mohammad Dawood and Klaus P Schäfers. 2015. *Motion Correction in Thoracic Positron Emission Tomography.* Springer.

Giraud, Philippe, and Annie Houle. 2013. 'Respiratory gating for radiotherapy: main technical aspects and clinical benefits'. *ISRN Pulmonology* 2013.

Gould, K Lance. 2017. *Optimizing quantitative myocardial perfusion by positron emission tomography for guiding CAD management.*

Grant, Alexander M, Timothy W Deller, Mohammad Mehdi Khalighi, Sri Harsha Maramraju, Gaspar Delso and Craig S Levin. 2016. 'NEMA NU 2-2012 performance studies for the SiPM-based ToF-PET component of the GE SIGNA PET/MR system'. *Medical physics* 43 (5): 2334–2343.

Grimm, Robert, Sebastian Fürst, Michael Souvatzoglou, Christoph Forman, Jana Hutter, Isabel Dregely, Sibylle I Ziegler, Berthold Kiefer, Joachim Hornegger, Kai Tobias Block et al. 2015. 'Self-gated MRI motion modeling for respiratory motion compensation in integrated PET/MRI'. *Medical image analysis* 19 (1): 110–120.

Guillaume, Marcel, Andre Luxen, Bruno Nebeling, Mario Argentini, John C Clark and Victor W Pike. 1991. 'Recommendations for fluorine-18 production'. *International Journal of Radiation Applications and Instrumentation. Part A. Applied Radiation and Isotopes* 42 (8): 749–762.

He, Jianfeng, Graeme J O'Keefe, Sylvia Jie Gong, Gareth Jones, Tim Saunder, Andrew M Scott and Moshi Geso. 2008. 'A novel method for respiratory motion gated with geometric sensitivity of the scanner in 3D PET'. *IEEE Transactions on Nuclear Science* 55 (5): 2557–2565.

Hirtl, A. 2017. 'Functional imaging technology and devices physical principles.'

Hudson, H Malcolm, and Richard S Larkin. 1994. 'Accelerated image reconstruction using ordered subsets of projection data'. *IEEE transactions on medical imaging* 13 (4): 601–609.

Jakoby, BW, Y Bercier, M Conti, ME Casey, B Bendriem and DW Townsend. 2011. 'Physical and clinical performance of the mCT time-of-flight PET/CT scanner'. *Physics in Medicine & Biology* 56 (8): 2375.

Johnson, Keith A, Satoshi Minoshima, Nicolaas I Bohnen, Kevin J Donohoe, Norman L Foster, Peter Herscovitch, Jason H Karlawish, Christopher C Rowe, Saima Hedrick, Virginia Pappas et al. 2013. 'Update on appropriate use criteria for amyloid PET imaging: dementia experts, mild cognitive impairment, and education'. *Journal of Nuclear Medicine* 54 (7): 1011–1013.

Jones, W. 1999. 'PETLINK Guideline'. *various web documents, CPS Innovations, 2002 & frequently updated.*

Kak, AC, and Malcolm Slaney. n.d. 'Principles of Computerized Tomographic Imaging (IEEE, New York, 1988)'. *Google Scholar:* 49.

Karp, Joel S, Suleman Surti, Margaret E Daube-Witherspoon and Gerd Muehllehner. 2008. 'Benefit of time-of-flight in PET: experimental and clinical results'. *Journal of Nuclear Medicine* 49 (3): 462–470.

Karp, Joel S, Gerd Muehllehner, David A Mankoff, Caesar E Ordonez, John M Ollinger, Margaret E Daube-Witherspoon, Arthur T Haigh and Daniel J Beerbohm. 1990. 'Continuous-slice PENN-PET: a positron tomograph with volume imaging capability'. *J Nucl Med* 31 (5): 617–627.

Keller, Sune H, Claus Svarer and Merence Sibomana. 2013. 'Attenuation correction for the HRRT PET-scanner using transmission scatter correction and total variation regularization'. *IEEE transactions on medical imaging* 32 (9): 1611–1621.

Kesner, Adam L, Paul J Schleyer, Florian Büther, Martin A Walter, Klaus P Schäfers and Phillip J Koo. 2014. 'On transcending the impasse of respiratory motion correction applications in routine clinical imaging-a consideration of a fully automated data driven motion control framework'. *EJNMMI physics* 1 (1): 8.

Kesner, Adam Leon, and Claudia Kuntner. 2010. 'A new fast and fully automated software based algorithm for extracting respiratory signal from raw PET data and its comparison to other methods'. *Medical physics* 37 (10): 5550–5559.

Kesner, Adam Leon, Ralph Alexander Bundschuh, Nicole Christine Detorie, Magnus Dahlbom, Sibylle Ilsa Ziegler, Johannes Czernin and Daniel Hillel Silverman. 2009. 'Respiratory gated PET derived in a fully automated manner from raw PET data'. *IEEE Transactions on Nuclear Science* 56 (3): 677–686.

Knapp, FF Russ, and S Mirzadeh. 1994. 'The continuing important role of radionuclide generator systems for nuclear medicine'. *European journal of nuclear medicine* 21 (10): 1151–1165.

La Fougère, C, A Rominger, S Förster, J Geisler and P Bartenstein. 2009. 'PET and SPECT in epilepsy: a critical review'. *Epilepsy & Behavior* 15 (1): 50–55.

Lalush, David S, and Benjamin MW Tsui. 2000. 'Performance of ordered-subset reconstruction algorithms under conditions of extreme attenuation and truncation in myocardial SPECT'. *The Journal of Nuclear Medicine* 41 (4): 737.

Lassen, Martin Lyngby. 2017. 'PET Quantification in PET/CT and PET/MR'.

Lassen, Martin Lyngby, Thomas Rasmussen, Thomas E Christensen, Andreas Kjær and Philip Hasbak. 2017. 'Respiratory gating in cardiac PET: Effects of adenosine and dipyridamole'. *Journal of Nuclear Cardiology* 24 (6): 1941–1949.

Lecomte, R, D Schmitt, AW Lightstone and RJ McIntyre. 1985. 'Performance characteristics of BGO-silicon avalanche photodiode detectors for PET'. *IEEE Transactions on Nuclear Science* 32 (1): 482–486.

Lecomte, Roger. 2009. 'Novel detector technology for clinical PET'. *European journal of nuclear medicine and molecular imaging* 36 (1): 69–85.

Lecoq, P. 2017. 'Pushing the limits in Time-Of-Flight PET imaging'. *IEEE Transactions on Radiation and Plasma Medical Sciences* 1 (6): 473–485.

Levin, Craig S, and Edward J Hoffman. 1999. 'Calculation of positron range and its effect on the fundamental limit of positron emission tomography system spatial resolution'. *Physics in Medicine & Biology* 44 (3): 781.

Liu, Chi, Adam M Alessio and Paul E Kinahan. 2011. 'Respiratory motion correction for quantitative PET/CT using all detected events with internalexternal motion correlation'. *Medical physics* 38 (5): 2715–2723.

Liu, Chi, Larry A Pierce II, Adam M Alessio and Paul E Kinahan. 2009. 'The impact of respiratory motion on tumor quantification and delineation in static PET/CT imaging'. *Physics in Medicine & Biology* 54 (24): 7345.

MacManus, Michael, Ursula Nestle, Kenneth E Rosenzweig, Ignasi Carrio, Cristina Messa, Otakar Belohlavek, Massimo Danna, Tomio Inoue, Elizabeth Deniaud-Alexandre, Stefano Schipani et al. 2009. 'Use of PET and PET/CT for radiation therapy planning: IAEA expert report 2006–2007'. *Radiotherapy and oncology* 91 (1): 85–94.

McClelland, Jamie R, David J Hawkes, Tobias Schaeffter and Andrew P King. 2013. 'Respiratory motion models: A review'. *Medical image analysis* 17 (1): 19–42.

Meikle, Steven R, Magnus Dahlbom and Simon R Cherry. 1993. 'Attenuation Correction Using Count-Limited Transmission Data in Positron Emmission Tomography'. *Journal of nuclear medicine* 34:143–143.

Miller, Michael, Jun Zhang, Katherine Binzel, Jerome Griesmer, Thomas Laurence, Manoj Narayanan, Deepa Natarajamani, Sharon Wang and Michael Knopp. 2015. 'Characterization of the vereos digital photon counting PET system'. *Journal of Nuclear Medicine* 56 (supplement 3): 434–434.

Muehllehner, G, MP Buchin and JH Dudek. 1976. 'Performance parameters of a positron imaging camera'. *IEEE Transactions on Nuclear Science* 23 (1): 528–537.

Müller-Horvat, Christian, Peter Radny, Thomas K Eigentler, Jürgen Schäfer, Christina Pfannenberg, Marius Horger, Sascha Khorchidi, Thomas Nägele, Claus Garbe, Claus D Claussen et al. 2006. 'Prospective comparison of the impact on treatment decisions of whole-body magnetic resonance imaging and computed tomography in patients with metastatic malignant melanoma'. *European Journal of Cancer* 42 (3): 342–350.

Munoz, Camila, Christoph Kolbitsch, Andrew J Reader, Paul Marsden, Tobias Schaeffter and Claudia Prieto. 2016. 'MR-based cardiac and respiratory motion-compensation techniques for PET-MR imaging'. *PET clinics* 11 (2): 179–191.

Myronenko, Andriy, and Xubo Song. 2010. 'Intensity-based image registration by minimizing residual complexity'. *IEEE transactions on medical imaging* 29 (11): 1882–1891.

Nehmeh, Sadek A. 2013. 'Respiratory motion correction strategies in thoracic PET-CT imaging'. *PET clinics* 8 (1): 29–36.

Nehmeh, Sadek A, Yusuf E Erdi, Clifton C Ling, Kenneth E Rosenzweig, Heiko Schoder, Steve M Larson, Homer A Macapinlac, Olivia D Squire and John L Humm. 2002. 'Effect of respiratory gating on quantifying PET images of lung cancer'. *Journal of nuclear medicine* 43 (7): 876–881.

Nuyts, Johan, Girish Bal, Frank Kehren, Matthias Fenchel, Christian Michel and Charles Watson. 2013. 'Completion of a truncated attenuation image from the attenuated PET emission data'. *IEEE transactions on medical imaging* 32 (2): 237–246.

Oppelt, Arnulf. 2011. *Imaging systems for medical diagnostics: fundamentals, technical solutions and applications for systems applying ionizing radiation, nuclear magnetic resonance and ultrasound.* John Wiley & Sons.

Ostertag, Hermann, Wolfgang K Kübler, Josef Doll and Walter J Lorenz. 1989. 'Measured attenuation correction methods'. *European journal of nuclear medicine* 15 (11): 722–726.

Papathanassiou, Dimitri, Stéphanie Becker, Roland Amir, Benoît Menéroux and Jean-Claude Liehn. 2005. 'Respiratory motion artefact in the liver dome on FDG PET/CT: comparison of attenuation correction with CT and a caesium external source'. *European journal of nuclear medicine and molecular imaging* 32 (12): 1422–1428.

Peng, Hao. 2007. *Investigation of new approaches to combined positron emission tomography and magnetic resonance imaging systems.* Vol. 68. 09.

Phelps, Michael E, Edward J Hoffman, Sung-Cheng Huang and Michel M Ter-Pogossian. 1975. 'Effect of positron range on spatial resolution.' *Journal of nuclear medicine: official publication, Society of Nuclear Medicine* 16 (7): 649–652.

Picard, Yani, and Christopher J Thompson. 1997. 'Motion correction of PET images using multiple acquisition frames'. *IEEE transactions on medical imaging* 16 (2): 137–144.

Pichler, B, E Lorenz, R Mirzoyan, W Pimpl, F Roder, M Schwaiger and SI Ziegler. 1997. 'Performance test of a LSO-APD PET module in a 9.4 Tesla magnet'. In *Nuclear Science Symposium, 1997. IEEE,* 2:1237–1239. IEEE.

Pichler, Bernd J, Martin S Judenhofer and Hans F Wehrl. 2008. 'PET/MRI hybrid imaging: devices and initial results'. *European radiology* 18 (6): 1077–1086.

Pichler, BJ, BK Swann, J Rochelle, RE Nutt, Simon R Cherry and SB Siegel. 2004. 'Lutetium oxyorthosilicate block detector readout by avalanche photodiode arrays for high resolution animal PET'. *Physics in Medicine & Biology* 49 (18): 4305.

Podgorsak, Ervin B, et al. 2005. 'Radiation oncology physics'. *Vienna: International Atomic Energy Agency:* 123–271.

Politis, Marios, and Paola Piccini. 2012. 'Positron emission tomography imaging in neurological disorders'. *Journal of neurology* 259 (9): 1769–1780.

Schindler, Thomas H, Heinrich R Schelbert, Alessandra Quercioli and Vasken Dilsizian. 2010. 'Cardiac PET imaging for the detection and monitoring of coronary artery disease and microvascular health'. *JACC: Cardiovascular Imaging* 3 (6): 623–640.

Sharma, Punit, Harmandeep Singh, Sandip Basu and Rakesh Kumar. 2013. 'Positron emission tomography-computed tomography in the management of lung cancer: An update'. *South Asian journal of cancer* 2 (3): 171.

Shepp, Lawrence A, and Yehuda Vardi. 1982. 'Maximum likelihood reconstruction for emission tomography'. *IEEE transactions on medical imaging* 1 (2): 113–122.

Steinert, Hans C. 2011. 'PET and PET-CT of lung cancer'. In *Positron Emission Tomography,* 33–51. Springer.

Surti, Suleman, and Joel S Karp. 2016. 'Advances in time-of-flight PET'. *Physica Medica: European Journal of Medical Physics* 32 (1): 12–22.

Thielemans, Kris, Charalampos Tsoumpas, Sanida Mustafovic, Tobias Beisel, Pablo Aguiar, Nikolaos Dikaios and Matthew W Jacobson. 2012. 'STIR: software for tomographic image reconstruction release 2'. *Physics in Medicine & Biology* 57 (4): 867.

Townsend, David W, Thomas Beyer and Todd M Blodgett. 2003. 'PET/CT scanners: a hardware approach to image fusion'. In *Seminars in nuclear medicine,* 33:193–204. 3. Elsevier.

Tsoumpas, Charalampos, Irene Polycarpou, Kris Thielemans, Christian Buerger, AP King, Tobias Schaeffter and PK Marsden. 2013. 'The effect of regularization in motion compensated PET image reconstruction: a realistic numerical 4D simulation study'. *Physics in Medicine & Biology* 58 (6): 1759.

Vaquero, Juan José, JJ Sánchez, José Manuel Udías, Jacobo Cal-González and Manuel Desco. 2013. 'MRI compatibility of position-sensitive photomultiplier depth-of-interaction PET detectors modules for in-line multimodality preclinical studies'. *Nuclear Instruments and Methods in Physics Research Section A: Accelerators, Spectrometers, Detectors and Associated Equipment* 702:83–87.

Watson, Charles C. 2000. 'New, faster, image-based scatter correction for 3D PET'. *IEEE Transactions on Nuclear Science* 47 (4): 1587–1594.

Watson, Charles C, DMEC Newport and Mike E Casey. 1996. 'A single scatter simulation technique for scatter correction in 3D PET'. In *Three-dimensional image reconstruction in radiology and nuclear medicine,* 255–268. Springer.

Watson, Charles C, ME Casey, C Michel and B Bendriem. 2004. 'Advances in scatter correction for 3D PET/CT'. In *Nuclear Science Symposium Conference Record, 2004 IEEE,* 5:3008–3012. IEEE.

Wernick, Miles N, and John N Aarsvold. 2004. *Emission tomography: the fundamentals of PET and SPECT.* Elsevier.

Yukutake, Masanobu, Tamito Sasaki, Masahiro Serikawa, Tomoyuki Minami, Akihito Okazaki, Takashi Ishigaki, Yoshifumi Fujimoto, Yuuki Hatta, Shigemi Kitamura and Kazuaki Chayama. 2014. 'The effect of respiratory-gated positron emission tomography/computed tomography in patients with pancreatic cancer.' *Hellenic journal of nuclear medicine* 17 (1): 31–36.